UNIVERSITÀ DI PARMA
DIPARTIMENTO DI INGEGNERIA E ARCHITETTURA

Dottorato di Ricerca in Tecnologie dell'Informazione
XXXVI Ciclo

Aizhan Issatayeva

Integrated liquid biopsy for cancer diagnostics via genomic biomarkers detection

DISSERTAZIONE PRESENTATA PER IL CONSEGUIMENTO
DEL TITOLO DI DOTTORE DI RICERCA

JANUARY 2024

UNIVERSITÀ DI PARMA

Dottorato di Ricerca in Tecnologie dell'Informazione

XXXVI Ciclo

Integrated liquid biopsy for cancer diagnostics via genomic biomarkers detection

Coordinatore:

Chiar.mo Prof. Marco Locatelli

Tutor:

Chiar.ma Prof. Annamaria Cucinotta

Dottoranda: *Aizhan Issatayeva*

January 2024

I dedicate my thesis to my Master thesis supervisors who motivated me to start a scientific path and to my beloved family and friends who supported me throughout the PhD journey.

Contents

List of Figures

List of Tables

Introduction

Cancer is one of the leading causes of death worldwide, causing more than 10 million deaths annually [1]. Detecting cancer in its early stages significantly enhances the survival chances of patients, but is challenging given the weak manifestation or absence of symptoms [2]. Regular population screening emerges as a promising approach for early-stage diagnosis [3]. However, current diagnostic methods have limitations: invasiveness of tissue biopsy, exposure of patients to ionizing radiation by imaging-based techniques, limited accuracy and sensitivity of stool- and blood-based tests [2–4]. One of the promising non-invasive and sensitive screening tools that recently gained research attention is liquid biopsy. The method is based on the detection of circulating tumor cells, exosomes, circulating tumor nucleic acids, and other tumor-related substances that may serve as cancer biomarkers in body fluids [2]. Circulating tumor DNAs and RNAs, continuously released into body fluids with a half-life of about 2.5 hours, are good candidates for real-time monitoring of tumor dynamics and therapy response [5]. Alterations in nucleic acids contribute significantly to genetic changes in cancer etiology and may be used for diagnosing cancer in early stages [6].

Examples of genomic biomarkers are an abnormal expression of some microRNAs (miRNAs), a point mutation in DNA sequences, and an altered level of DNA methylation [2, 7]. MiRNAs are 17-25 nucleotides (nt) long non-coding RNAs that regulate gene expression [8, 9]. Altered levels of some miRNAs can lead to the suppression of tumor suppressor genes or modulation of oncogenes, thus promoting cancer formation [8]. For instance, the concentration of miRNA-21, miRNA-126, miRNA-155, or miRNA-191 is $10^{-14} - 10^{-13}$ M in healthy people's serum, but they

are about 100 times more overexpressed in breast cancer patients' serum [10]. Circulating tumor DNAs are long fragments (about 150 nt) of DNA present in body fluids at a concentration of about 10^{-10} M [2, 11]. They contain information about tumor-specific changes, including single-nucleotide point mutations and DNA methylation levels [12]. Single-point mutations in some genes, like KRAS, BRCA2, BRAF, and TP53, are positively correlated with cancer development [13, 14]. DNA methylation is defined as an addition of a methyl group $(-CH_3)$ to cytosines. Hypermethylation at a particular gene (regional) can be found in 12% of cancer cases and hypomethylation through a whole genome (global) is associated with 70% of cancer patients [15]. A gold standard technique for the miRNA and DNA measurements is the fluorescence-based detection of the targets pre-amplified by the polymerase chain reaction (PCR) [16]. The fluorescence-based technique requires a multi-step assay and labeling with a fluorescent dye due to weak auto-fluorescence from biological samples [17]. Hence, there is room for developing more straightforward, faster, and more accurate techniques for detecting DNAs and miRNAs in body fluids.

This thesis aims to explore alternative methods for detecting DNAs and miRNAs, with potential applications in liquid biopsy for cancer screening. Thus, one of the attractive techniques that can provide molecular-specific and trace-sensitive information of a biological sample is surface-enhanced Raman spectroscopy (SERS). The working principle is based on inelastic scattering, that is the scattering of light with a frequency different from the frequency of the incident light [18, 19]. This difference, called Raman shift, being a result of the molecular vibrations, is specific to each molecule. Thus, the Raman spectrum, which represents the intensity profile of the scattered light as a function of the Raman shift, provides information about the qualitative and quantitative composition of an analyzed sample [20]. SERS uses metal nanoparticles (NPs) to enhance Raman scattering through a localized surface plasmon resonance effect [18, 21]. There are three main types of NP arrangements on SERS substrates: NPs in a colloidal solution, NPs immobilized on a solid substrate, and nanostructures fabricated on a substrate [22]. The motivation to study SERS for liquid biopsy application is its potential to outperform the fluorescence-based gold standard. Thus, label-free SERS measurement of DNAs and miRNAs can be achieved

with more straightforward assays [23]. Labeled SERS can result in a better multiplexing ability because Raman reporters have narrow bands allowing multiple of them to be used simultaneously for the detection of several biomarkers [19, 23].

The work conducted during this Ph.D. is a part of the European project "Photonics for healthcare: multiscale cancer diagnosis and therapy" (PHAST-ETN). This project involves 14 beneficiaries and 8 partner organizations around Europe. As a part of the project, I had secondments in different organizations: 2 months in Politecnico di Torino, Turin, Italy under the supervision of Professor Davide Janner, 4.5 months in Leibniz Institute of Photonic Technology (Leibniz-IPHT), Jena, Germany under the guidance of Professor Michael Schmitt, 1.5 months in Tyndall National Institute, Cork, Ireland under the direction of Professor Stefan Andersson-Engels, and 1 month in Horiba SAS company, Lille, France under the supervision of Doctor Sébastien Legendre.

The thesis is organized as follows:

- Chapter 1 reviews biological protocols used for target-specific SERS measurement of DNAs and miRNAs. The protocols are categorized into groups based on their working principles. The review evaluates the future potential of SERS-based sensing to reach a clinical level, either by replacing or complementing existing gold standards. Evaluation criteria include the detection capabilities of SERS-based protocols and their suitability for liquid biopsy applications. This comprehensive review is based on an analysis of over 150 papers, and the findings are reflected in the paper [24].

- Chapter 2 presents the results of direct SERS measurement of miRNAs and their bases with NPs immobilized on a glass substrate and NPs in a colloidal solution. Three different types of NPs, such as AuNPs, AgNPs produced by the Lee-Meisel method, and AgNPs fabricated by the Leopold-Lendl approach, will be evaluated for SERS sensing of miRNAs. The work presented in this chapter was conducted during the secondments at Politecnico di Torino and Leibniz-IPHT.

- Chapter 3 discusses the application of a capture-based biological protocol for

the target-specific detection of miRNAs on a solid substrate. The experiments were performed during the secondment at Tyndall National Institute.

- Chapter 4 proposes the application of photonic crystal fibers (PCFs) as a microfluidic device for the measurement of DNAs and miRNAs. The hollow regions of PCFs can be used for incorporating analytes so that a light-analyte interaction can be used for different sensing methods. This chapter presents two approaches for the nucleic acids measurement in PCFs. The first is the SERS measurement of miRNAs attached to the inner surface of the solid core PCFs by a capture-based protocol. SERS measurement in PCFs can be advantageous compared to a single-point measurement in a solution or on a substrate due to a longer interaction area between an analyte, NPs, and light [25]. The experiments were conducted during the secondment at Tyndall National Institute. The second sensing method used for DNA detection is based on a shift of a transmission spectrum. This shift is caused by an increased thickness of PCF's cladding achieved due to the bio-layer formed by the step-by-step functionalization protocol. This chapter will discuss the optimization of the optical setup used for this measurement.

- Chapter 5 presents the measurement of miRNA and its bases conducted with a novel method, called Tip-Enhanced Raman Spectroscopy (TERS). TERS is the technique that combines scanning probe microscopy (SPM) with Raman spectroscopy to provide topographic and spatially resolved chemical information. In this method, a sharp metallic tip with a nm-size apex is brought in contact with a sample and illuminated to produce enhanced Raman scattering. The position of the tip relative to the sample is controlled by the feedback from SPM. As a result, a TERS signal can be measured at a particular point on the sample, or a TERS map over a region can be recorded. TERS measurements were performed during the secondment in Horiba SAS.

- Conclusion summarizes the results achieved in different types of measurement of nucleic acids and evaluates the potential of each studied technique to be used for liquid biopsy application.

Chapter 1

SERS and its application for the genomic biomarkers detection

1.1 Gemonic biomarkers of cancer

Genomic biomarkers are defined as alterations in DNA and RNA characteristics that can be used to distinguish between normal biological and pathogenic processes, predict the response to therapy, and assess disease progression [7]. Different types of changes in nucleic acids can serve as genomic biomarkers, but in this thesis three of them will be covered: deregulation of miRNA expression, DNA point mutation, and DNA methylation. Those alterations have gained research attention as promising biomarkers that can be detected by SERS-based protocols.

The main function of miRNAs, non-coding RNAs consisting of 17-25 nt, is the regulation of gene expression [8, 9]. While the majority of miRNAs are intracellular, some migrate outside and can be found in various body fluids, including blood, urine, saliva, breast milk, and others [9]. Circulating miRNAs may contribute to cancer development by reducing the levels of tumor suppressor genes or by increasing the levels of oncogenes. The first case occurs when specific miRNAs, like miRNA-21, are overexpressed, while the latter scenario happens when other miRNAs, such as miRNA-34, are downregulated [9]. The potential of miRNAs to serve as cancer

biomarkers was initially explored by Lawrie *et al.* in 2008, who observed elevated levels of miRNA-21, miRNA-155, and miRNA-210 in serum of patients with diffuse large C-cell lymphoma [26]. Since then many studies have been conducted in this field. Galvao-Lima *et al.* compiled a list of miRNAs associated with breast, cervical, and prostate cancers and organized them into a Venn diagram grouping according to their relevance to one or two of the specified cancers [27]. A review conducted by Sundarbose *et al.* has presented the deregulated miRNAs detected in cancer cells, blood, plasma, serum, and tissue of patients with different types of cancer, including breast, glioblastoma, gastric, lung, oral, ovarian, prostate, pancreatic, hepatocellular, and others [28].

DNA point mutation is a substitution of one nucleotide by another one in DNA sequence [29]. Point mutations depending on their location in genes can cause a variety of abnormal genetic processes that may lead to cancer formation or spread [30]. Their potential as diagnostic and prognosis biomarkers has been analyzed by many studies. For example, the genome-wide association has revealed 77 point mutations that separately or in combination account for 30% of familial prostate cancer risks [31]. Macinnis *et al.* have developed algorithms to predict a familial prostate cancer risk based on family history and 26 point mutations [32]. Penney *et al.* have studied the application of point mutations for the discrimination of two types of colorectal cancer, mucinous and non-mucinous [33]. Garrigos *et al.* have analyzed 64 point mutations and found out that an absence or presence of some mutations can forecast a progression of metastatic renal cell carcinoma [34].

DNA methylation is the process of the methyl group (CH_3) addition to the cytosine-phosphate-guanine (CpG) dinucleotide of the DNA molecule [35]. The CpG dinucleotide is present in the human genome either as short sequences distributed throughout the genome or as long sequences (hundreds to thousands nt), clustered in the promoter regions of genes and called CpG islands. Under normal conditions, the CpG inside the islands is unmethylated, while non-clustered CpGs are usually methylated [36]. Therefore, increased methylation in the CpG islands or decreased number of methylated non-clustered CpGs through the whole genome cause two types of abnormalities, called regional hypermethylation and global hypomethylation respec-

tively. Regional hypermethylation can lead to the inactivation of the tumor suppressor genes and global hypomethylation may cause chromosomal instability, mutations, and oncogenes activation [3, 37]. Therefore, both types of abnormalities can serve as biomarkers for different types of cancer, like breast [38], lung [39], gastric [40], prostate, bladder, colorectal, ovarian, and other [41]. The review by Mikeska *et al.* has shown that methylation-based cancer biomarkers can be detected in body liquids, like plasma, stool, sputum, serum, bronchoalveolar lavage, bronchial aspirates, and urine [36]. Jensen *et al.* have used hypermethylation in the C9orf50, KCNQ5, and CLIP4 genes to design a blood-based test for the detection of colorectal cancer [42]. The authors have assessed the test on two different cohorts and achieved a good sensitivity of about 80% at an early stage (even higher at later stages), and a high specificity of 99% for all stages [42]. Furthermore, at least 22 methylation-based cancer kits have already reached the clinical practice [35, 43].

One of the most widely used techniques for DNA point mutation detection is based on the amplification of the target by PCR-based methods and real-time monitoring by fluorescence-based techniques [44]. This versatile method is also applicable for quantifying the expression levels of miRNAs and assessing DNA methylation levels. However, both targets require specific pre-treatment steps: miRNAs should be converted to complementary DNA by the reverse transcription process [16] and the methylated cytosines in the DNA sequence should be converted into thymine with the bisulfite treatment followed by the reverse transcription [45]. This method requires labeling and complex multi-step protocols, which motivates researchers to explore alternative sensing methods. SERS is a powerful vibrational spectroscopy technique with a promising potential for this application. This chapter presents a description of the SERS working principle and an overview of the biological protocol for SERS detection of genomic biomarkers.

1.2 SERS working principle

Figure 1.1 (a) illustrates a schematic of the energy level diagram of a molecule. When a photon is incident on the molecule with energy insufficient to promote it to a higher

energy state, the molecule enters a virtual energy state instead [20]. This state is unstable, prompting the molecule to rapidly return to its original state and release a photon. Typically, this scattered photon has the same energy as the incident one, and the process is called elastic or Rayleigh scattering. Occasionally, the molecule returns to a level higher or lower than its initial state, causing the photon to scatter with a decreased or increased energy which results in Stokes Raman or anti-Stokes Raman scattering respectively [20]. The energy variation leads to a difference in wavelengths between the incident (λ_{inc}) and scattered photons (λ_{sc}), defining a so-called Raman shift (v_{Raman}) [46]:

$$v_{Raman}[cm^{-1}] = \frac{1}{\lambda_{inc}[cm]} - \frac{1}{\lambda_{sc}[cm]} \tag{1.1}$$

Raman scattering is caused by various molecular vibrations associated with structural changes within molecules, including ring deformation, ring breathing, and different bond-related motions such as stretching, bending, twisting, and others [46, 47]. Each structural change corresponds to a specific value of the Raman shift. Therefore, the Raman spectrum, portraying the intensity profile of scattered light as a function of the Raman shift, serves as a unique fingerprint for the illuminated molecule [20]. The positions of the Raman peaks provide a qualitative indication of the molecule's chemical composition, while the intensity can provide approximate quantitative information.

Raman scattering is a rare event, occurring with only 1 out of 10 million photons [20]. Therefore, amplification techniques are necessary for detecting samples in trace concentration ranges [18]. SERS is one of the amplification techniques that utilizes metal NPs for electromagnetic (EM) and chemical enhancement of Raman scattering. Chemical enhancement is achieved through two processes, namely chemical complexation and a change in charge transfer. The former results from the interaction of absorbed light and molecules, forming an absorbate-metal complex and increasing the probability of certain vibrational motions. The latter involves an exchange of electrons between the metal NP and the analyzed sample's molecules, modifying the polarizability (α_0) and contributing to EM enhancement [48].

Figire 1.1 (b) illustrates the principle of EM enhancement. The EM wave with

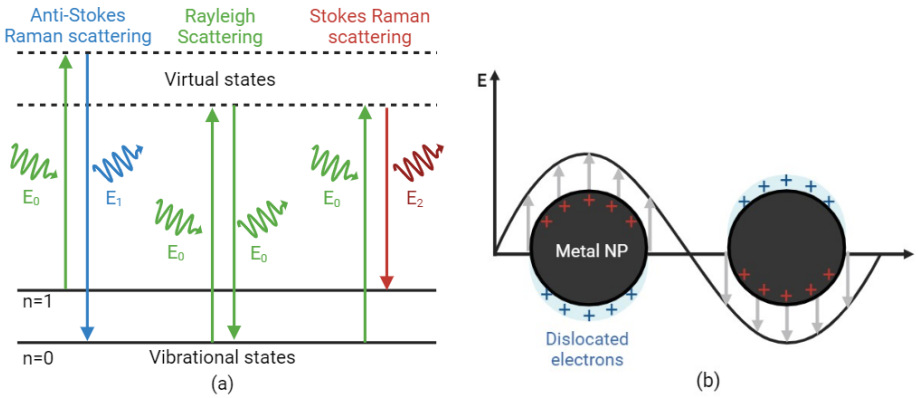

Figure 1.1: (a) Schematic diagrams of energy states of a molecule illustrating Rayleigh, Stokes Raman, and anti-Stokes Raman scattering. (b) Schematics of the localized surface plasmon resonance effect: a dislocation of electrons under the influence of electromagnetic field induces a metal nanoparticle (NP) to become a dipole and enhance the local field.

frequency w_0 and amplitude E_0 incident on the metal NP can drive collective oscillation of its electrons, called plasmons. When the EM wave's frequency matches the natural frequency of oscillation, the electrons can be displaced from their original position forming a cloud with a negative charge. This process of electrons' excitation is referred to as surface plasmon resonance (SPR). As a result, the metal NP acts like an induced dipole, and its induced polarization P_0 depends on the polarizability of the electrons α_0 and the EM field:

$$P_0 = \alpha_0 \times E_0(w_0) \tag{1.2}$$

As a result, the electric field is induced between the poles of the dipolar metal NP which leads to the generation of a local EM field with a Raman-shifted frequency w_R and amplitude E_{loc} near the edges of NPs. The local EM field exceeds the incident EM field, leading to the EM enhancement of the Raman signal by a factor of EF_{ex}:

$$EF_{ex} = \left[\frac{E_{loc}(w_0)}{E_0(w_0)}\right]^2 \tag{1.3}$$

This process occurs in the nearest proximity to the NPs and is called localized SPR (LSPR) [48]. A similar interaction occurs when a molecule of analyte is placed in the local EM field of metal NPs: the molecule transforms into a dipole which results in further Raman signal enhancement by a factor of EF_R:

$$EF_R = \left[\frac{E_{loc}(w_R)}{E_0(w_R)}\right]^2 \tag{1.4}$$

Two enhancement factors are comparable if w_R and w_0 are approximately equal. As a result, the overall enhancement factor EF_{total} of the Raman signal at the fourth power of the EM field can be obtained [48]:

$$EF_{total} = \frac{|E_{loc}(w_R)|^4}{|E_0(w_0)|^4} \tag{1.5}$$

This implies that even a modest increase in the field results in significant SERS enhancement [49]. Since the LSRP effect is localized on the edge of NPs, the enhancement drops significantly with an increased distance from the NPs (D^{-10}) [50]. Overall, chemical and EM enhancement results in the amplification of the Raman fingerprint information by about $10^4 - 10^8$ times [18, 21]. Further enhancement up to $10^9 - 10^{12}$ times is observed in the so-called hot spot, a region between two neighboring NPs, where the coupling of their plasmons results in the increased LSRP [48]. Figure 1.2 (a) shows three types of NP arrangement mainly used as SERS substrates, such as an NP colloidal solution, NPs on a solid substrate, and ordered nanostructures [22]. NP colloidal solutions are synthesized by a bottom-up approach that involves reducing silver or gold ions with the agents and controlling the NPs aggregation [51]. The second type of substrates is produced by a self-organization process when the NPs are attached to a silanized surface [51]. Ordered nanostructures are fabricated through the creation of nanopatterns using lithography-based methods, followed by the deposition of a metal layer [51]. The fabrication procedure of ordered nanostructures is more complex, but they usually provide better reproducibility due to the

uniform arrangement of the hot spots [17].

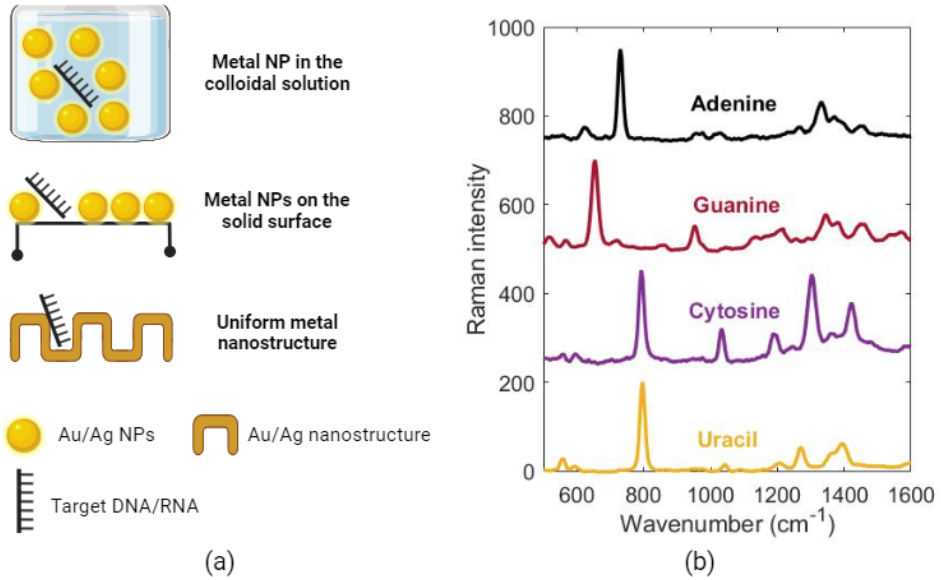

Figure 1.2: Schematics of (a) the types of the SERS substrates and (b) the SERS spectra of RNA bases, such as adenine, guanine, cytosine, and uracil.

1.3 SERS-based bio-protocols for the genomic biomarkers detection

The SERS-based detection of nucleic acids was first presented in 1994 by Vo-Dinh and his colleagues [52]. A single strand of DNA or RNA is a sequence of nucleotides, each consisting of a phosphate group, a sugar group, and one of the nitrogen bases, such as adenine (A), thymine (T), guanine (G), cytosine (C), or uracil (U). There are two pairs of complementary bases, such as G-C and A-T/U (for DNA/RNA respectively), that can bind with each other to form double-stranded DNA (dsDNA) or DNA-RNA structures [53]. Fig. 1.2 (b) shows the normalized SERS spectra of four RNA bases, each having its unique characteristic peaks. For example, a peak at

734 cm^{-1} is found only in the spectrum of adenine, and the peak around 658 cm^{-1} is characteristic of guanine. A peak around 792 cm^{-1} is common for both cytosine and uracil, so these two bases should be discriminated by additional SERS information [54]. The SERS spectra of nucleotides are similar to the respective bases but have additional contributions from a sugar group and a phosphate group [55]. DNAs and RNAs represent a mixture of several nucleotides, so their spectrum is constituted by the peaks of all nucleotides present in the sequence. The contribution from each base in the sequence is different and approximately corresponds to the rule A=2×C=20×G=20×T [56, 57]. This rule can be used to convolute the spectrum of nucleic acid and determine the concentration of each base, thereby differentiating the sequence of analyzed DNA or RNA [58]. Thus, the direct SERS measurement of miRNAs [59–63] and DNA point mutations [64–70] can be achieved by discriminating the sequences based on the intensity of the SERS peaks associated with five bases. This can be done by manual analysis or an application of statistical tools, such as the partial least squares discriminant analysis (PLS-DA) and the principal component analysis (PCA). SERS detection of DNA methylation is conducted by evaluating the shift of the cytosine's peaks occurring when the base is methylated [15, 71–82].

This direct approach is simple because the assay consists only of NPs and the target analyte, but it has been demonstrated only for the measurement in water or buffer solution in the absence of any interfering substances. For liquid biopsy application, the target biomarker should be captured from a pool of DNAs, RNAs, proteins, and other substances, so the target-specific biological protocol should be applied. Most protocols involve the labeling of the target or supporting sequences with the Raman reporter molecule. The protocols usually explore the NPs-analyte distance dependency of SERS: an introduction of the target sequence induces a change in the distance between the reporter and the SERS substrate, leading to a detectable variation of the reporter's SERS signal. Labeled SERS is usually more sensitive than the previously described direct approach because the detection relies on the Raman reporter molecules that have a much stronger signal than DNAs or miRNAs [53]. The amplitude of the signal change should depend on the target's concentration making this method promising for quantitative measurement.

A literature search of the published SERS-based approaches for the detection of miRNA level changes, DNA point mutations, and DNA methylation level alterations has resulted in 158 papers. The earliest works were presented in 2008. The total number of works related to miRNA detection is significantly higher (105) than the number of papers about point mutation (34) and DNA methylation (19). The biological protocols for all three genomic biomarkers have been classified according to their working principle into five common groups: capture-, displacement-, sandwich-, and cleavage-based methods, and a specialized group combining some unique assays. Figure 1.3 illustrates all groups of the protocol and the schematics of their working principles.

1.3.1 Capture of the target

Fig. 1.3 (a1-a4) show the first group of protocols that are based on the immobilization of a single-stranded DNA (ssDNA) on the SERS substrate. This so-called capture DNA is selected to be complementary to the target miRNA or DNA to be able to hybridize with it. Other sequences and interfering substances are blocked from absorption into the SERS substrate, so selective detection is achieved.

Figure 1.3 (a1) shows the simplest capture protocol that can be used to detect the label-free or labeled target sequences. In the label-free version, the change in the SERS signal is caused by the appearance of the hybridized target miRNA or DNA in the SERS active region and a formation of new bonds [83, 84]. Labeling of the target leads to the detection of a strong signal from the Raman reporter, resulting in more sensitive detection [85–88]. This and further presented protocols can be applied to all three types of genomic biomarkers with some modifications. In the case of DNA point mutation, a mismatched DNA is only one nucleotide different from the target DNA, so it can partially hybridize with the capture strand. An additional step of washing or an application of heat or electric potential should be applied to break the unstable partial hybridization [85–90]. DNA methylation does not involve a sequence change, so a preliminary bisulfite treatment is applied to convert all unmethylated cytosines to uracil. When the sequence is changed, the problem is traced back to the detection of DNA point mutation [91, 92].

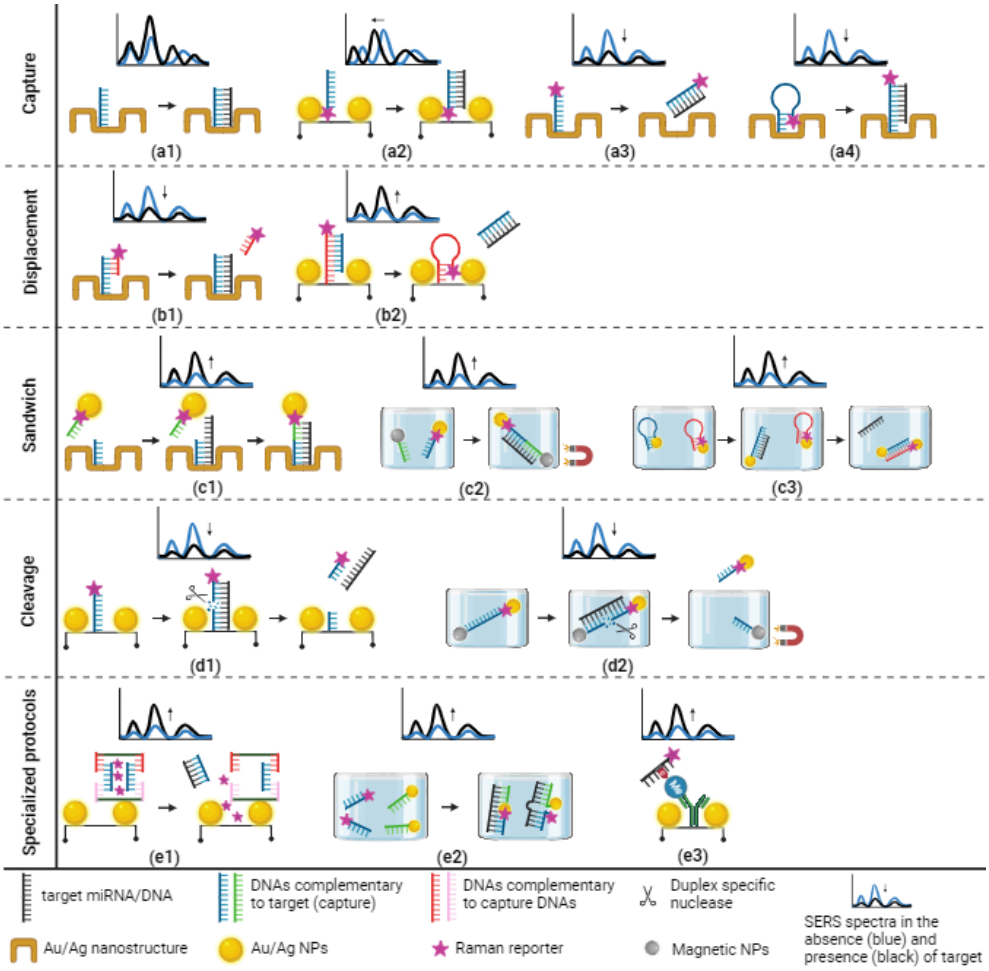

Figure 1.3: Summary of the SERS-based protocols for the detection of the genomic biomarkers grouped according to their working principle.

Labeling of the target used in the previous protocol requires the target to be first captured from the analyzed body fluid to get labeled. Therefore, in real settings, other protocols relying on labeling of the supporting sequences should be practically more convenient. For example, the Raman reporter can be immobilized directly on the

surface of NPs, and the capture DNA can be placed on top of it as illustrated in Fig. 1.3 (a2). The hybridization of the capture DNA with the target leads to mechanical stretching of the reporter's bonds and consequent frequency shift of its SERS peak [93–95]. The peak shifts by about 0.5 cm^{-1} in response to the $10^{-17}M$ target, which is sufficiently large to be distinguished from the average peak's variation of about 0.022 cm^{-1} caused by some non-reproducibility of measurements [95].

The working principle of the protocol shown in Fig. 1.3 (a3) is based on the decrease of the binding affinities of DNA towards the metal and graphene surfaces when the double-stranded complex is formed [96]. Under the optimized conditions, when the labeled capture DNA hybridizes with the target, the formed dsDNA can be detached from the SERS substrate leading to a decrease in the SERS signal [96–99].

Figure 1.3 (a4) illustrates an application of a labeled hairpin DNA that allows good control over a distance between the reporter and the metal surface [100–112]. A hairpin structure is formed by the hybridization of the two complementary ends of the capture DNA. The hairpin brings the reporter in proximity to the SERS surface producing a strong SERS response. The capture DNA is also complementary to the target, causing their mutual hybridization to be sufficiently strong to open up the hairpin. As a result, the reporter is moved at a distance equal to the length of the hairpin DNA, and the SERS signal reduction is observed.

1.3.2 Displacement by the target

The methods schematized in Fig. 1.3 (b1 and b2) are based on disrupting partial hybridization between two DNAs, referred to as capture and placeholder, by hybridizing one of them with the target sequence. Thus, in the first protocol, the target hybridizes with the capture DNA and the labeled placeholder strand is detached from the SERS substrate, resulting in a signal drop [25, 113–124]. The second method shown in Fig. 1.3 (b2) applies the hairpin capture DNA initially open due to hybridization with the placeholder DNA. When the target sequence hybridizes with the placeholder DNA, the liberated hairpin DNA closes and the reporter molecule is brought closer to the substrate producing the enhanced signal [110, 125–130]. The displacement-based methods can be combined with amplification techniques [131, 132].

1.3.3 Formation of a sandwich

Figure 1.3 (c1-c3) combines the protocols based on a molecular sandwich approach that applies two capture DNAs complementary to the two ends of the target. One of them is attached to the SERS substrate, while another DNA is labeled and attached to a metal NP. The hybridization of the target sequence with both captures brings the NP close to the SERS substrate producing the hot spot between them. The signal enhancement in the hot spot is larger than it is near one NP, so the original SERS signal from the reporter molecule increases by about three times [133–145].

The same method can also be extended to the colloidal solution, where two metal NPs play the role of both SERS-active agents [146–155]. Figure 1.3 (c2) shows that one of the NPs can also be a magnetic particle. A magnet applied to the solution forces the magnetic particles to remain in the solution while all other substances are filtered. The target sequence attaches the DNAs on the metal NP and magnetic particles to each other, so the reporter remains in the solution after filtering and produces a strong SERS signal. In the absence of the target miRNAs or DNAs, the SERS-active NPs with labeled DNAs being unattached to the magnets leave the solution and no SERS response from the reporter is observed [110, 156–164]. The sandwich-based assays depicted in Fig.1.3 (c1 and c2) can be used with the pre-amplification techniques, such as strand displacement amplification [165], hairpin-chain reaction [166–168], rolling circle amplification [169], and PCR [170, 171].

Figure 1.3 (c3) presents an application of two hairpin DNAs complementary to each other and attached to the NPs. The first hairpin is labeled, and its reporter is close to the NP, producing a moderate SERS signal. The target nucleic acid opens the first hairpin, and its liberated end hybridizes with the second hairpin due to the more preferable hybridization. The target is released to participate in a new cycle. The reporter molecule in the hot spot between the two NPs exhibits the SERS signal about 3 times stronger than at the initial state [172–186].

Some protocols, mainly hairpin-based, can be considered in combination with fluorescence-based detection. In this case, the appropriately selected Raman reporter can also play the role of a fluorophore, while the NPs can additionally serve as a fluorescence quencher. The hairpins move the reporter to and from the NPs to produce

opposite changes in the fluorescence and SERS signals [102, 110, 172, 179, 182]. This experiment also shows that the two sensing techniques have comparable performance when applied in the same settings, implying the potential of SERS to be used at the same level as the fluorescence-based gold standard [182].

1.3.4 Cleavage by enzymes

The cleavage-based protocols are based on the enzymes that are activated by the formation of dsDNA, such as duplex-specific nuclease (DSN), T7 exonuclease, Exo III, CRISPR-Cas12 enzyme, and S1 nuclease. Figure 1.3 (d1) shows the labeled capture DNA which forms the double-stranded complex through hybridization with the target miRNA or DNA. This dsDNA activates the enzyme urging it to cleave the capture strand. The reporter is detached from the substrate, leading to the SERS signal drop. The target is released to participate in a new cycle, providing signal amplification [129, 187–193].

As shown in Fig. 1.3 (d2), the cleavage-based method can also be integrated with the magnetic separation in the NPs colloidal solution [130, 194–197]. The target hybridization with the capture DNA induces the cleavage of the capture DNA and detachment of the labeled SERS-active NPs from the magnetic particles. The NPs leave the solution after magnetic separation, and the SERS signal reduction is observed.

1.3.5 Specialized protocols

The last group of protocols combines the assays with distinctive working principles. For example, the protocol shown in Fig. 1.3 (e1) is based on a closed microcapsule filled with the reporter molecules and placed on the SERS substrate. Each side wall of the capsule is made of a pair of ssDNAs connected by the capture DNA, while the top and bottom of the capsule are made of the two acrylamide strands [198–200]. The hybridization of the target with the capture DNA forces its detachment from the ssDNAs and opens up the capsule. The capsule can also be formed by putting the reporters on the $CaCO_3$ particle covered by a layer of positively charged oly(allylamine hydrochloride) and a layer of negatively charged ssDNAs. The hybridization of ssD-

NAs with the target activates the cleavage of the formed duplex [201]. In both cases, the reporters are released from the open capsules and the SERS signal is recorded.

Figure 1.3 (e2) demonstrates a protocol designed particularly for DNA point mutation. The technique applies a ligase and two DNA stands complementary to two parts of the target, one labeled and one attached to the metal NP. Two DNAs hybridize with the target so that the NP and the reporter are placed at a point of possible mutation. If the mutation is absent, the ligase joins two DNA strands bringing the reporter close to the NP, so the SERS signal is detected. In case of a point mutation, the ligation does not occur and the reporter does not produce any SERS response [202–205]. A specific point mutation can be also detected by applying a polymerase with the displacement-based method. The capture DNA, that is attached to the labeled placeholder DNA, starts to hybridize with the target or point mutated DNA. The polymerase extends the target sequence displacing the placeholder DNA and reducing the signal from the reporter. However, the mismatched DNA can not be extended due to the mutated nucleotide and cannot displace the placeholder [206].

Figure 1.3 (e3) presents the protocol based on the methylation-specific antibodies (such as methyl-binding domain proteins) and applied for DNA methylation sensing [6]. The antibodies immobilized on the SERS substrate are used as captures that can catch the labeled DNA sequences at their methyl groups. In case of no methylation in the sequence, the DNA is not captured and its reporter does not produce any SERS signal [207–209]. This method is mostly suitable for a global methylation evaluation, while all previously presented techniques combined with bisulfite treatment can be used for the regional methylation level measurement.

1.4 Discussion

The groups of protocols are arranged in Fig. 1.3 according to the complexity of their working principle from the simplest to the most challenging. Thus, the capture-based assays use one supporting DNA, while the displacement-based methods require two DNAs. The sandwich-based approach applies an additional NP, while the cleavage-based methods need enzymes. The specialized protocols require the complex cap-

sules or application of polymerase, ligase, and antibodies. This arrangement can be used to find the protocol that reached a good performance with a relatively simple assay. The performance of the protocols will be assessed by two factors: detection ability evaluated by the protocol's limit of detection (LOD) and applicability in body fluids. The LOD can be estimated by $\frac{3 \cdot \sigma}{m}$, where σ is the standard deviation and m is the slope of the calibration plot [195]. The LOD should be sufficient to measure the physiological concentration of nucleic acids in body fluids: about $10^{-10}M$ for DNAs and about $10^{-14}M$ for miRNAs. Regarding the applicability, the validation of the biological protocols should be conducted in an environment as close as possible to body fluids. The detection of the targets was presented in different media, including water/buffer solution, spiked serum, total RNAs/DNAs extracted from cancer, and real urine, plasma, or serum. The biological protocols will be evaluated using Table 1.1 which provides the best-performed example for each detection method. The best example was selected by first filtering the papers that achieved the LOD sufficient for the detection of the target biomarker or, in the absence of one, the works with the lowest LOD. Then, among those filtered papers, the one that presented the best applicability in body fluid was selected.

As can be seen, most protocols have the labeled techniques as the best-performed examples. The reporters used to achieve sensitive labeled detection are listed in the table and include: p-methoxybenzoic acid (pMBA), 6-Carboxyl-X-Rhodamine (ROX), 6-Carboxyfluorescein (FAM), Cyanine-5 (Cy5), Cyanine-3 (Cy3), Rhodamine 6G (R6G), Adenosine-5'-Triphosphate (ATP), crystal violet (CV), 4-Mercaptobenzoic acid (MBA), 5,5-dithiobis(2-nitrobenzoic acid) (DTNB), 3-mercaptophenylboronic acid (MPBA), 5-Carboxytetramethylrhodamine (TAMRA), 1-tetradecanol (TD), 4-aminobenzenethiol (ABT), 4-mercapto-3-nitro benzoic acid (MNBA), 1,3,3,1',3',3',-hexamethyl-2,2'-indotricarbocyanine iodide (HITC), and texas red (TR). Most labeled protocols have shown the LODs sufficient for measuring the physiological concentration of nucleic acids, except the hairpin-assisted displacement method that detected miRNAs at about $5 \times 10^{-12}M$ [127] and the affinity difference-based capture protocol that recognized point mutation in about $10^{-8}M$ DNA [99]. In terms of applicability, the protocols for miRNA measurement have demonstrated the most promising poten-

tial: all labeled capture- and sandwich-based methods were tested in real serum, and the displacement- and cleavage-based protocols were applied in total RNAs. To compare, only four out of all labeled protocols for DNA point mutation (three capture- and one displacement-based) were tested in complex matrices, like blood, plasma, serum, and total RNA. No protocols for DNA methylation measurement were tested in body fluids and only one labeled sandwich-based approach was applied in total RNA. The length of nucleic acid is another parameter that should be considered to evaluate the applicability. To recall, the length of miRNAs in body fluids is about 17-25 nt long, and most papers have presented their protocols for detecting 22-23 nt long sequences. Circulating DNAs are longer (about 150 nt), but most protocols for their detection were tested for 17-53 nt long sequences. Only the hairpin-assisted capture and displacement protocols have been used for the sufficiently long DNAs detection [105, 117]. Thus, the protocols that achieved both sufficient LODs and applicability in body fluids are the labeled capture and sandwich protocols for miRNA detection and the labeled capture and displacement protocols for DNA point mutation recognition.

According to Table 1.1, the label-free methods are mentioned as best-performing examples for some protocols, including simple and affinity difference-based capture protocols for miRNA detection [83, 98], sandwich-based assay for point mutation recognition [143], and simple capture protocol for methylation measurement [91]. Their LODs are insufficient or at a bare minimum for the miRNAs and DNAs detection. The presented applicability of the label-free techniques is also not sufficient: only the affinity difference-based method for miRNA detection was tested in total RNAs. The potential of some label-free methods is promising, but more work should be conducted to consider them for liquid biopsy application.

The SERS-based techniques were found to be mostly compatible with miRNAs due to their shorter length and higher relative difference in sequences, making manipulations with them easier. Thus, the protocols for the detection of DNA point mutation usually apply additional pre-amplification, and post-washing steps because recognizing the mutation of one nucleotide in a long sequence is challenging. Most protocols for the DNA methylation measurement requires also bi-sulfite treatment.

Table 1.1: Performance of the SERS-based protocols for the measurement of miRNAs, DNA point mutation, DNA methylation level. LOD - limit of detection [24].

Protocol	Fig. 1.3	Label	Matrix	LOD (M)	Ref.
miRNAs					
Capture	(a1)	label-free	buffer	5×10^{-10}	[83]
	(a2)	pMBA	serum	10^{-17}	[94]
	(a3)	label-free	total RNA	5×10^{-12}	[98]
	(a4)	ROX,FAM,Cy5	serum	10^{-18}	[105]
Displacement	(b1)	Cy3	total RNA	5×10^{-17}	[116]
	(b2)	Cy5	total RNA	5×10^{-12}	[127]
Sandwich	(c1)	Cy5	serum	2×10^{-16}	[152]
	(c2)	R6G,4-ATP,CV	serum	3×10^{-16}	[161]
	(c3)	R6G	serum	3×10^{-17}	[181]
Cleavage	(d1)	MBA	total RNA	3×10^{-16}	[188]
	(d2)	DTNB	total RNA	1×10^{-16}	[196]
Specialized	(e1)	MPBA	spiked serum	1×10^{-17}	[199]
DNA point mutation					
Capture	(a1)	Cy3,TAMRA	plasma	5×10^{-11}	[88]
	(a2)	DSNB	serum	10^{-16}	[95]
	(a3)	TR	buffer	10^{-8}	[99]
	(a4)	FAM	total DNA	10^{-13}	[112]
Displacement	(b1)	Cy5	blood	4×10^{-13}	[120]
Sandwich	(c1)	label-free	buffer	10^{-6}	[143]
	(c2)	TD,HITC	buffer	10^{-16}	[163]
Cleavage	(d1)	DTNB	spiked serum	3×10^{-16}	[193]
Specialized	(e2)	ABT	buffer	3×10^{-14}	[205]
DNA methylation					
Capture	(a1)	label-free	water	10^{-10}	[91]
	(a4)	Cy5	buffer	3×10^{-12}	[92]
Sandwich	(c1)	MBA,MNBA	total RNA	10^{-12}	[145]
Specialized	(e3)	R6G	spiked serum	2×10^{-12}	[208]

Thus, the detection of miRNA has not only shown better LOD and applicability but also multiplexing abilities and integration with advanced substrates. For example, the multiplex detection of up to 9 miRNAs [101, 105, 109, 117, 121, 139, 175] and even simultaneous measurement of miRNA and other types of biomarkers (like proteins) have been presented [94]. Moreover, some well-performed protocols for miRNA detection have been applied with the advanced SERS substrates, microfluidic systems [102, 115, 122, 123, 176], and lateral flow assays-based devices [109].

The review has shown that SERS-based methods have some advantages over currently applied fluorescence-based detection. First of all, the sensitivity of the label-free techniques with relatively simple assays can be improved by designing the appropriate SERS sensors, especially for miRNA detection. The labeled protocols based on one-to-two-step detection (capture and displacement) can also decrease the complexity of currently used assays. Furthermore, the labeled SERS techniques can provide better multiplexing abilities due to more narrow signals from the reporters, so the diagnostic accuracy can be improved by relying on several biomarkers. Finally, the labeled SERS can be applied in combination with fluorescence-based methods to overcome their limitations and reach more accurate detection.

1.5 Conclusion

In conclusion, the literature review has shown that the SERS-based detection of genomic biomarkers, especially miRNAs, has gained considerable research attention during the last decade. Some protocols for miRNA detection already reached sufficient LODs and applicability to be implemented in practice. The label-free and some one-to-two-step labeled capture or displacement protocols have shown sensitive detection of genomic biomarkers with relatively simple assays, thus having the potential to outperform or supplement the current fluorescence-based gold standard. Moreover, the detection of up to 9 targets has been presented opening the opportunity for more accurate diagnostics based on several biomarkers. Further research in this direction should be focused on improving the sensitivity and reproducibility of the SERS sensors. Therefore, in the next chapters, different SERS substrates (NPs on a solid sur-

face, NPs colloidal solutions, PCFs with immobilized NPs) will be discussed. The results of this review have been presented in paper [24], which can hopefully attract the interest of many researchers to this topic and stimulate work in this direction.

Chapter 2

SERS measurements of miRNAs and its bases

2.1 SERS substrates development

As previously discussed in chapter 1, there are three types of SERS substrates: metal NPs in a colloidal solution, arrays of NPs on a solid substrate, and uniform metal nanostructures. This section focuses on the fabrication and testing of NPs on a solid substrate and colloidal solutions of NPs.

2.1.1 Fabrication and testing of NPs on the solid substrate

The synthesis and testing of the NPs on a solid substrate have been conducted during the secondment at Politecnico di Torino, Turin, Italy. The NPs which are Au seeds covered with Ag shell were grown on top of the glass slides to achieve a wider SPR band. The fabrication process, illustrated in Fig. 2.1 (a-d), involves the following steps :

- Glass preparation: Glass slides were cleaned using acetone, ethanol, and piranha solution. Then, the slides were incubated in an APTES solution to achieve silanization.

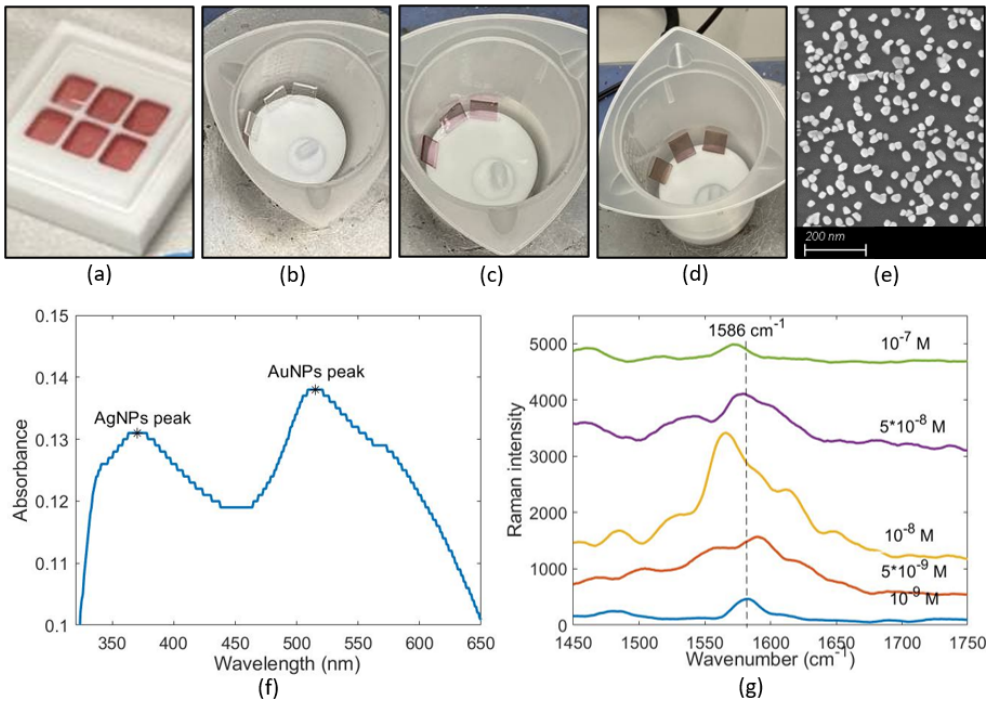

Figure 2.1: The development and testing of the SERS substrate based on Au-Ag NPs on the glass slide: (a-d) fabrication procedure, (e) an SEM image of the substrate, (f) a UV/Vis spectrum of the substrate, (g) a SERS spectra of 4-Mercaptobenzoic acid measured at concentrations from 10^{-9} M to 10^{-7} M.

- Formation of the Au core: The seeding of AuNPs is achieved by incubating the silanized glass slides in a solution of commercial 20 nm AuNPs as shown in Fig. 2.1 (a). AuNPs were further grown to a size of 50-60 nm by a magnetic stirring of the glass slides in a solution of gold chloride ($HAuCl_4$) and hydrogen peroxide (H_2O_2). Figure 2.1 (b) and (c) show the change of the color of the glass from transparent to purple after the growth of AuNPs.

- Formation of the Ag shell: the shell was grown on the surface of AuNPs by a magnetic stirring of the glass slides in a solution containing silver nitrate

($AgNO_3$), trisodium citrate ($Na_3C_6H_5O_7$), and ascorbic acid ($C_6H_8O_6$). Figure 2.1 (d) illustrates the color transition of the glass to a brownish shade signifying the formation of the Ag shell.

The characterization of the NPs has been performed using a scanning electron microscope (SEM) and UV/Vis spectroscopy. According to the SEM image in Fig. 2.1 (e), an arrangement of NPs on the glass is relatively uniform, and their average size is about 90 nm. The UV/Vis spectrum in Figure 2.1 (f) exhibits two distinct SPR peaks associated with Au (470-550 nm) and Ag (350-440 nm) NPs implying the successful formation of Au-Ag NPs.

To evaluate the glass substrate's performance, SERS measurements of MBA used as a test molecule, were conducted. The measurement has been performed using Horiba's commercial Raman equipment with the following parameters: 785 nm wavelength, 50 mW power, 1200 gr/mm grating, 10 s acquisition time, and 3 acquisitions. Figure 2.1 (g) displays SERS spectra of MBA at concentrations ranging from 10^{-9} M to 10^{-7} M, with a prominent peak at approximately 1586 cm^{-1} associated with the molecule. The peak intensity increases up to a concentration of 10^{-8} M, after which it starts to decrease. This decrease may be attributed to the progressive degradation of the Ag shell, as the same substrate was used for all five measurements. The glass substrates were not employed for subsequent SERS measurements of miRNAs due to the Ag shell's rapid degradation and long fabrication time.

2.1.2 Fabrication of NPs colloidal solution

Colloidal solutions of NPs were prepared and employed for SERS measurements during the secondment at Leibniz-IPHT in Jena, Germany. Three colloidal solutions of NPs were fabricated, including gold NPs and two types of silver NPs produced using the Leopold-Lendl and Lee-Meisel protocols, referred to as AgNPs-LL and AgNPs-LM, respectively.

AuNPs were synthesized using the citrate-reduction method introduced by Turkevich and colleagues in 1951 [210] and is still being applied with some modifications [211, 212]. In short, 50 ml of 0.01% gold chloride aqueous solution was boiled in the

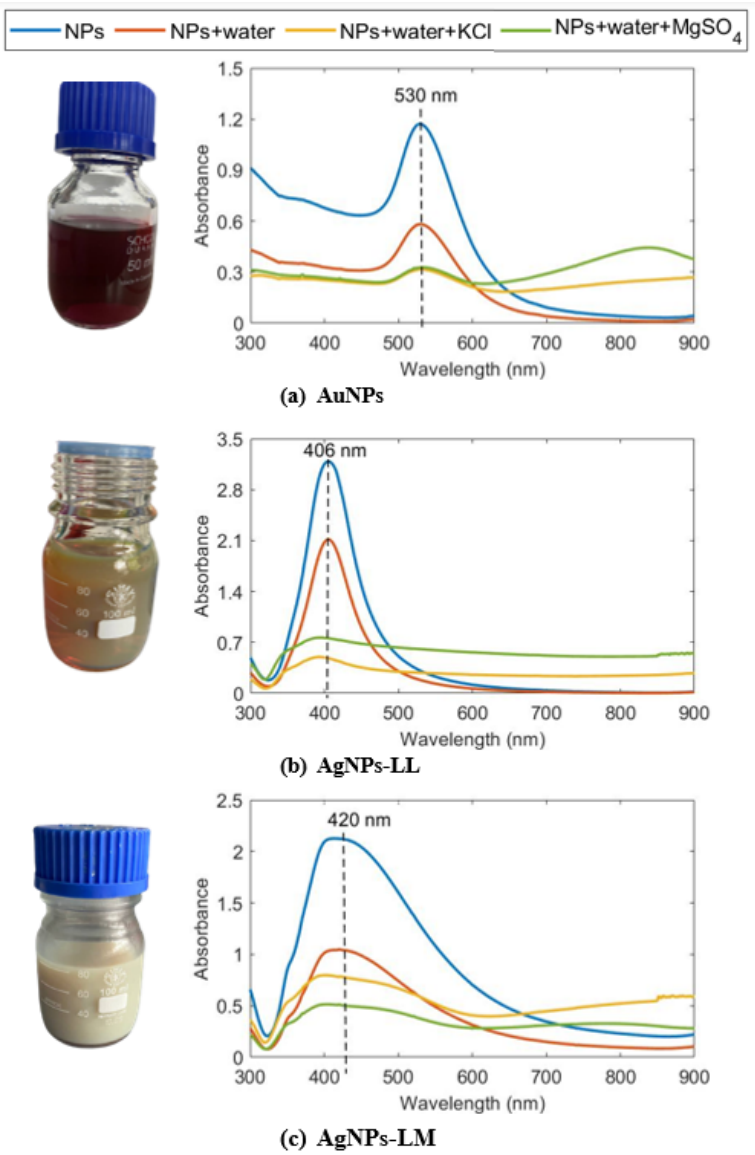

Figure 2.2: UV/Vis spectra of the synthesized NPs colloidal solutions: (a) AuNPs, (b) AgNPs-LL (diluted 1:4), (c) AgNPs-LM (diluted 1:2).

flask under vigorous stirring. Then, 0.6 ml of 1% trisodium citrate aqueous solution was added quickly. The solution turned dark blue and eventually stabilized at purple, as depicted in Fig. 2.2 (a). Boiling was continued for 30 minutes with a reflux system to maintain a constant water level.

AgNPs-LL were fabricated following the protocol presented by Leopold-Lendl in 2003 [213]. This method involves the reaction of 1 mM silver nitrate with 1.5 mM hydroxylamine hydrochloride ($NH_2OH * HCl$) and 3 mM sodium hydroxide ($NaOH$) in the total volume of 100 ml of water [214, 215]. The reaction was held under vigorous stirring at room temperature for 30 minutes. The final color of the NPs solution is brown-gray as illustrated in Fig. 2.2 (b).

AgNPs-LM were synthesized using the citrate-reduction method presented by Lee and Meisel in 1982 [216]. An aqueous solution of 1 mM silver nitrate was boiled in a 100 ml flask, followed by a quick addition of 2 ml of a 1% aqueous solution of trisodium citrate [214]. The solution turned green-yellow and was continuously boiled for 60 minutes under vigorous stirring, utilizing a reflux device. The final appearance of the NPs solution is displayed in Fig. 2.2 (c).

UV/Vis measurements were conducted to characterize the NPs. In Figure 2.2 (a), the spectrum of AuNPs (blue line) exhibits an SPR peak at approximately 530 nm. According to Ali et al., who followed the same protocol and obtained a similar UV/Vis spectrum, the NPs are spherical with an average diameter of around 40 nm [212]. Figure 2.2 (b) displays the UV/Vis spectrum of AgNPs-LL (blue line) with a peak at about 406 nm, consistent with findings in [214]. This suggests that AgNPs-LL are also spherical and fall within the size range of 10-30 nm. In Figure 2.2 (c), the spectrum of AgNPs-LM (blue line) presents a broader peak than that reported in [214]. This indicates a variation in the NPs' sizes, likely ranging from 30-80 nm. Both AgNPs-LL and AgNPs-LM were diluted with water due to oversaturation issues with the pure NP solution.

An aggregation of the NPs with some agents is expected to improve SERS measurements for two reasons. Firstly, adding an aggregating agent after introducing the sample into the NPs solution can lead to the clustering of NPs around the sample molecule, potentially increasing the SERS signal by trapping the sample in hot spots

[58]. Secondly, all three NPs have an SPR peak smaller than the laser wavelength (785 nm) used for SERS measurements. The NPs aggregation is expected to broaden the SPR peak to cover the desired wavelength range. Therefore, various aggregating agents were tested with all three colloidal solutions. Figure 2.2 displays the UV/Vis spectra of each NPs solution after aggregation with potassium chloride KCl (orange line) and magnesium sulfate $MgSO_4$ (green line). Water was used as an analyte in the measurement. For most aggregated NPs, the SPR peak intensity decreased, and a new broad peak in the 600-900 nm range emerged. This indicates cluster formation and the expansion of wavelength range suitable for achieving significant SERS enhancement.

2.2 SERS measurement of RNA bases with NPs colloidal solution

2.2.1 SERS measurements of bases

The next step was determining the optimal NPs colloidal solution and aggregation conditions. All RNA bases at a concentration of 10^{-4} M were measured with nine different colloidal solutions. These include three types of aggregation conditions (no aggregation, aggregation with KCl, and aggregation with $MgSO_4$), each applied to three types of NPs. SERS measurements have been conducted with the WITec Raman system and with the following parameters: 785 nm wavelength, 80 mW power, 300 gr/mm grating, 2 s acquisition time, and 5 acquisitions. The samples have been measured inside a 96-well plate, by mixing 90 μl of NPs, 90 μl of an analyte, and 20 μl of aggregating agents. SERS spectra were subjected to Baek's baseline correction algorithm.

Figure 2.3 illustrates the results of SERS measurement of NPs conducted to check their background (a) and the results of Raman measurement of all RNA bases performed without the application of NPs (b). The SERS spectrum of AgNPs-LL exhibits minimal background, while the spectra of AuNPs and AgNPs-LL show some peaks that may influence the measured samples' spectra. However, if the contribu-

tion from a sample is sufficiently high, the background from AuNPs and AgNPs-LL is expected to be negligible. According to Fig. 2.3 (b), no prominent peaks can be detected by Raman measurement, so the use of NPs to enhance the signal is crucial.

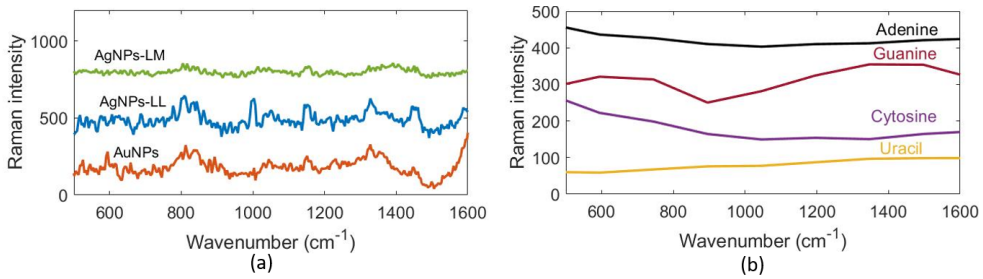

Figure 2.3: (a) The SERS spectra of the bare NPs and (b) the Raman spectra of RNA bases, such as adenine, guanine, cytosine, uracil.

Figure 2.4 displays SERS spectra of all four bases obtained using nine different colloidal solutions. SERS spectra of each base exhibit several prominent peaks, that are listed in Table 2.1. The band assignment for each peak provided in the table has been performed according to [47]. The most distinctive peaks that will be mainly used for the discrimination of each base in further experiments are adenine's peak at 734 cm^{-1}, cytosine's peaks at 792 cm^{-1} and 1303 cm^{-1}, guanine's peak around 658 cm^{-1}, and uracil's peak at 796 cm^{-1}. Notably, uracil exhibits the least intensity of the SERS peaks which is almost commensurate with the background from NPs. Therefore, it was challenging to detect uracil and the best conditions appeared to be the NPs aggregated with $MgSO_4$. Other bases could be measured by most of the conditions, but overall AuNPs without aggregation exhibit a good performance. Consequently, the four most promising solutions have been selected for further tests: AuNPs, AuNPs aggregated with $MgSO_4$, AgNPs-LL aggregated with $MgSO_4$, and AgNPs-LM aggregated with $MgSO_4$.

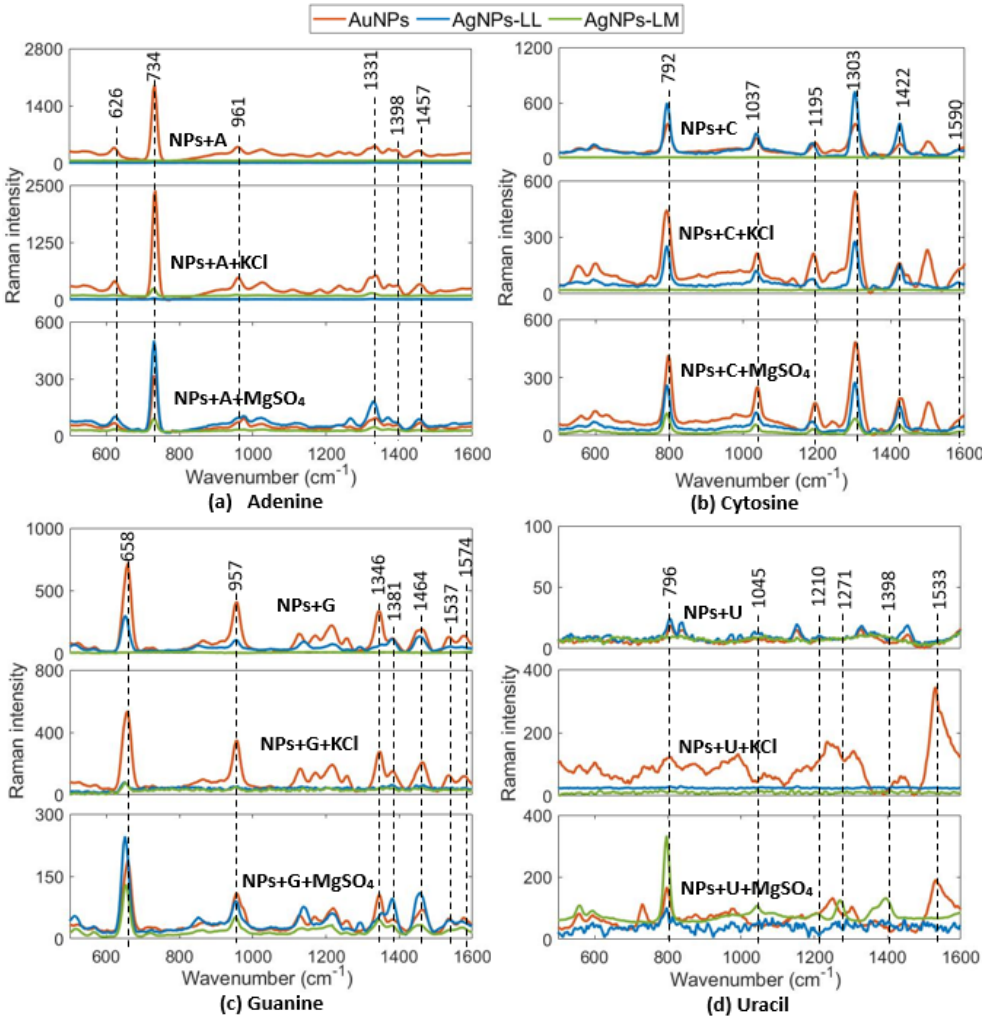

Figure 2.4: The SERS spectra of RNA bases measured at a 10^{-4} M concentration: (a) A - adenine, (b) C - cytosine, (c) G - guanine, (d) U - uracil.

Table 2.1: Band assignment for the SERS spectra of RNA bases [47].

Base	Wavenumber (cm^{-1})	Band assignment
Adenine	626	6-ring deformation
	734	ring breathing
	961	5-ring deformation
	1331	stretching C5-N7, N1-C2, C2-N3, C5-C6, bending C2/8-H
	1398	stretching C4-N9, C4-C5, C6-N10, N7-C8, bending C2-H
	1457	stretching C2-N3, N1-C6, bending C2-H, scissoring NH_2
Cytosine	792	ring breathing
	1037	wagging CH3
	1195	ring stretching C-N
	1303	ring stretching C-N
	1422	bending N1-H, C5-H, C6-H
	1590	bend NH_2
Guanine	658	6-ring breathing, 5-ring deformation, wagging NH_2
	957	5-ring deformation
	1346	bending N1-H, N10-H12, stretching C2-N10
	1381	ring stretching C-N, C-C, rocking NH_2, bending N1/9-H
	1464	ring stretching C-N, bending C8-H, N1-H, N10-H
	1537	ring stretching C-N, scissoring NH_2, bending N1-H
	1574	scissoring NH_2, stretching C2-N10
Uracil	796	ring breathing
	1045	ring deformation
	1210	bending N1-H, C6-H, C5-H, stretching C6-N1
	1271	stretching N3-C4, C4-C5, C6-N1, bending N1-H, C5/6-H
	1398	bending N1-H, C6-H, C5-H
	1533	stretching C5-C6, C6-N1 bending C6-H

2.2.2 SERS measurements of the mixtures of bases

All bases, initially at a concentration of 10^{-4} M, were mixed in equal ratios, resulting in a total of 11 mixtures containing 2 to 4 bases. The mixtures were measured with four colloidal solutions mentioned earlier. For clarity, the SERS spectra of mixtures containing adenine are consolidated and displayed in Fig. 2.5. Each spectrum is denoted by the initial letters of the bases included in the mixture.

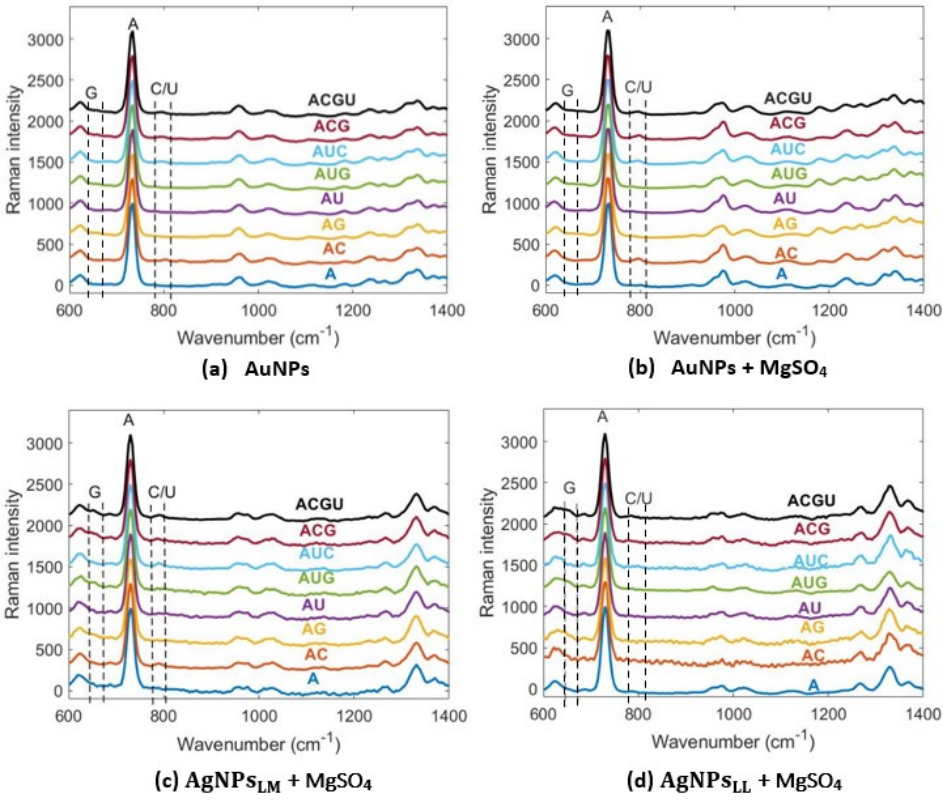

Figure 2.5: The SERS spectra of the mixtures of A (adenine), C (cytosine), G (guanine), U (uracil) at 10^{-4} M measured with (a) AuNPs, (b) AuNPs aggregated with $MgSO_4$, (c) AgNPs-LM aggregated with $MgSO_4$, (d) AgNPs-LL aggregated with $MgSO_4$.

The prevalence of adenine in the mixtures is in agreement with the dominance rule in DNA/RNA sequences mentioned in chapter 1. The peaks of cytosine and uracil around 792 cm^{-1} and 796 cm^{-1} are very small but detectable by all colloidal solutions except AgNPs-LL aggregated with $MgSO_4$. Since the peaks are very close to each other they are combined into one peak for the mixtures containing both bases. Detecting guanine is challenging because its peak at 658 cm^{-1} is close to the adenine's peak at 626 cm^{-1}. Nevertheless, in mixtures containing guanine and measured with AgNPs-LM and AgNPs-LL, the peak broadens, indicating its presence.

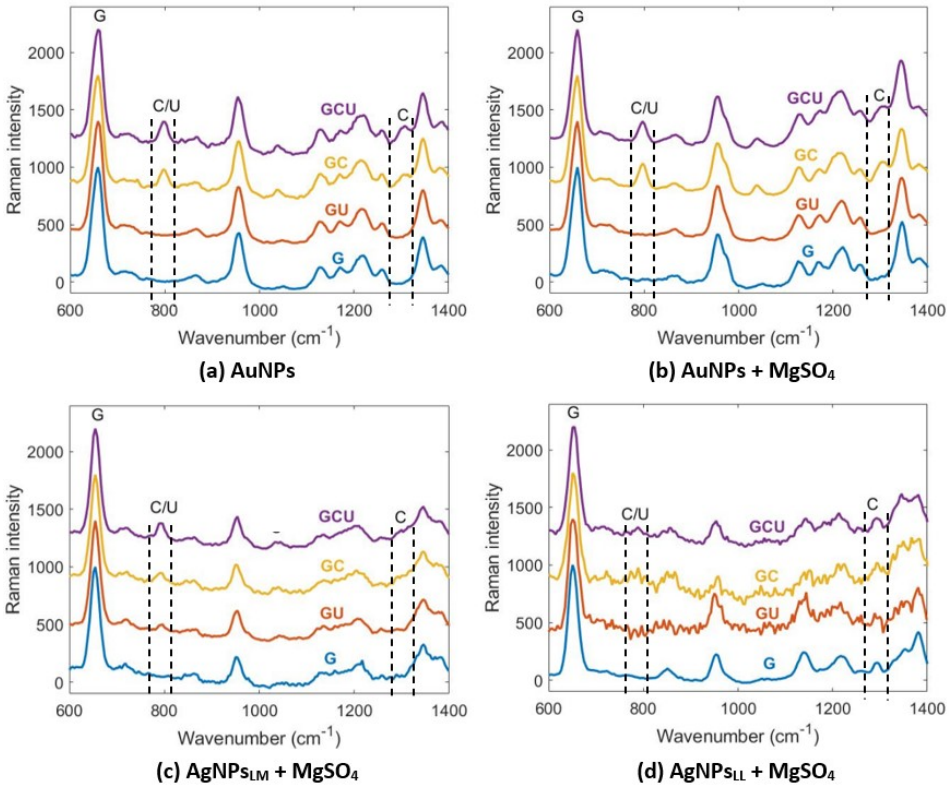

Figure 2.6: SERS spectra of the mixtures of G (guanine), C (cytosine), U (uracil) at 10^{-4} M measured with (a) AuNPs, (b) AuNPs aggregated with $MgSO_4$, (c) AgNPs-LM aggregated with $MgSO_4$, (d) AgNPs-LL aggregated with $MgSO_4$.

Figure 2.6 (a-d) shows that in the absence of adenine, guanine starts to dominate over the other two bases. It is not in agreement with the dominance rule inside the sequence, which states that cytosine should be the second dominating base. In the mixtures, the peaks of cytosine around 792 and 1303 cm^{-1} are detected by all four measurement conditions. The peak of uracil around 796 cm^{-1} is only detected by AgNPs-LM aggregated with $MgSO_4$ (see Fig. 2.6, c).

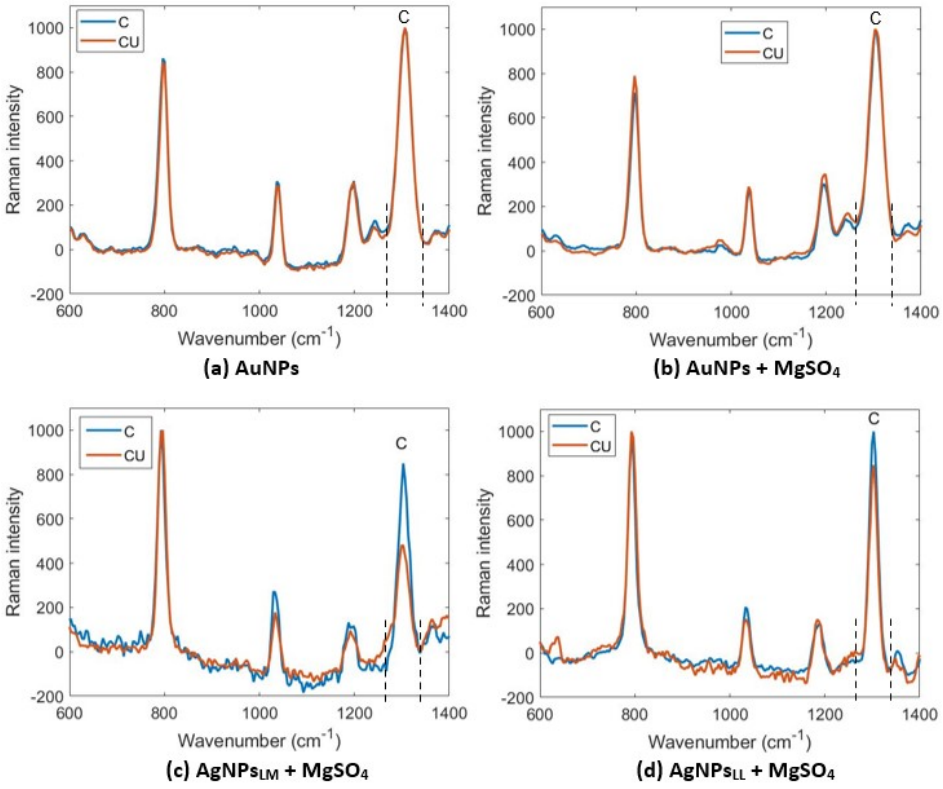

Figure 2.7: The SERS spectra of the mixture of C (cytosine) and U (uracil) at 10^{-4} M measured with (a) AuNPs, (b) AuNPs aggregated with $MgSO_4$, (c) AgNPs-LM aggregated with $MgSO_4$, (d) AgNPs-LL aggregated with $MgSO_4$.

Figure 2.7 (a-d) depicts the SERS spectra of the mixtures of cytosine and uracil measured with four colloidal solutions. The spectra of C and CU have been normal-

ized by their common peak around 792-796 cm^{-1}. There is no significant difference between the two spectra when measured with AuNP, both non-aggregated and aggregated with $MgSO_4$. The most noticeable difference is in the cytosine's peak at 1303 cm^{-1} that can be detected by AgNPs-LM aggregated with $MgSO_4$. It again shows the ability of this solution to discriminate between cytosine and uracil bases.

Thus, the measurement of bases and their mixtures revealed AgNPs-LM aggregated with $MgSO_4$ to be the most sensitive SERS substrate among all tested solutions. This is in agreement with the study of [54], who compared the performance of AgNPs-LM without aggregation, aggregated with $MgCl$, and aggregated with $MgSO_4$ and found out that the latter provides the best SERS enhancement of anions.

2.3 SERS measurement of miRNAs

One of the first discovered miRNAs is the let7 family, which involves 13 miRNAs with similar sequences and functions that are associated with different types of cancer [217, 218]. Thus, let7a is overexpressed in the serum of breast, prostate, renal, and colon cancer patients and is underexpressed in the serum of people with lung and gastric cancer. Let7i is upregulated in the serum of breast and gastric patients and downregulated in the lung and thyroid cancer patients' serum [217]. Two miRNAs being from the same family have highly similar sequences, with a variance of 4 nucleotides. Specifically, let7a has a sequence UGAGGUAGUAGGUUGUAUAGUU, characterized by 5 As, 8 Gs, 9 Us, and no Cs. In contrast, let7i has a sequence UGAGGUAGUAGUUUGUGCUGUU, consisting of 3 As, 8 Gs, 10 Us, and 1 Cs. Two miRNAs and the bases used in this chapter were supplied by Sigma Aldrich.

In this section, four aforementioned NPs solutions will be employed to conduct SERS measurements of miRNAs. The objective is to assess whether AgNPs-LM is indeed the optimal choice for this application. Figures 2.8 depict the SERS spectra of let7a (blue) and let7i (green) across various concentrations ranging from $10^{-4}M$ to $10^{-8}M$. According to Fig. 2.8 (d), the least promising results were obtained with AgNPs-LL. This is evidenced by the absence of characteristic peaks associated with adenine (734 cm^{-1}) and other bases in the miRNAs spectra. The spectra resemble

that of a control sample, comprising RNAse-free water mixed with NPs and the aggregating agent (represented by the dotted black line).

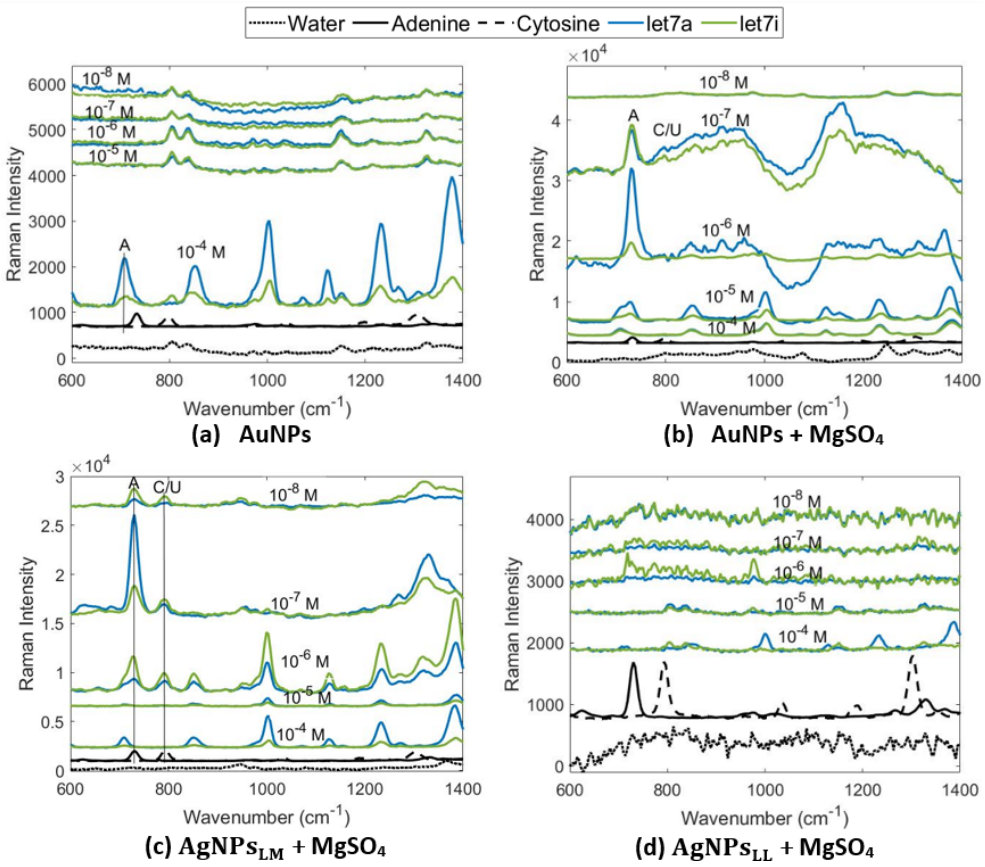

Figure 2.8: The SERS spectra of let7a and let7i at different concentrations measured with (a) AuNPs, (b) AuNPs aggregated with $MgSO_4$, (c) AgNPs-LM aggregated with $MgSO_4$, (d) AgNPs-LL aggregated with $MgSO_4$. The peaks of A (adenine) and C/U (common peak of cytosine and uracil) are noted.

According to Fig. 2.8 (a-c), the SERS spectra of miRNAs at $10^{-4}M$ measured by the other three colloidal solutions contain the peak of adenine around 710 cm^{-1}.

The peak shift can potentially be attributed to the high concentration of DENINE with respect to the NPs size which may have led to a reduced SERS effect and the detection of the Raman signal of adenine instead. As depicted in Fig.2.8 (a), the SERS spectra of miRNAs at a lower concentration, measured using AuNPs, resemble the spectrum of water, leaving miRNAs undetectable. However, AuNPs aggregated with $MgSO_4$ provide distinct SERS spectra of miRNAs at lower concentrations. Fig.2.8 (b) illustrates that the adenine's peak for 10^{-5} M miRNAs is broadened, potentially indicating the presence of both Raman and SERS signals from the molecule. As the concentration decreases further, the adenine's peak not only aligns with the expected 734 cm^{-1} position but also intensifies, likely due to an improved miRNA-to-NP ratio. The lowest miRNA concentration remains undetected. Figure 2.8 (c) demonstrates that AgNPs-LM outperforms other solutions by providing the distinctive adenine's peak at 734 cm^{-1} and the common peak of cytosine and uracil around 792 cm^{-1} for all concentrations down to 10^{-8} M.

Thus, AgNPs-LM resulted in the best performance among all tested solutions because of the lower detection limits and more observable cytosine peak. It confirms the results of SERS measurement of the bases and their mixtures. The second best solution is AuNPs aggregated with $MgSO_4$.

2.3.1 Comparison of SERS spectra of let7a and let7i

The ratio of the number of cytosines and uracils to the number of adenines in let7a and let7i is 1.80 and 3.67, respectively. Consequently, the following relation is expected for the ratio of their peak around 792 cm^{-1} (C/U) and 734 cm^{-1} (A):

$$\frac{peakCU_{let7a}}{peakA_{let7a}} < \frac{peakCU_{let7i}}{peakA_{let7i}} \tag{2.1}$$

This assumption is going to be tested and, if validated, can be used to discriminate two miRNAs from each other.

As shown previously, highly concentrated miRNAs resulted in the left-shifted spectra, so miRNAs at the concentration from $10^{-6}M$ to $10^{-8}M$ with smaller increments have been measured using AgNPs-LM aggregated with $MgSO_4$. Figure 2.9 (a)

illustrates that the SERS spectra have prominent peaks of adenine and cytosine/uracil, but the intensity of these peaks does not follow a linear pattern concerning miRNA concentration. This is because any small variations in the NPs used to measure each sample can make it difficult to obtain quantitative information. In addition, Fig. 2.9 (b) shows that the ratio of the peaks varies for both miRNAs at different concentrations and does not satisfy the ratio in Eq. 2.1. This is probably because the orientation of the miRNAs towards the NPs is not fixed, so the intensity depends on the distance between each base and neighboring NPs.

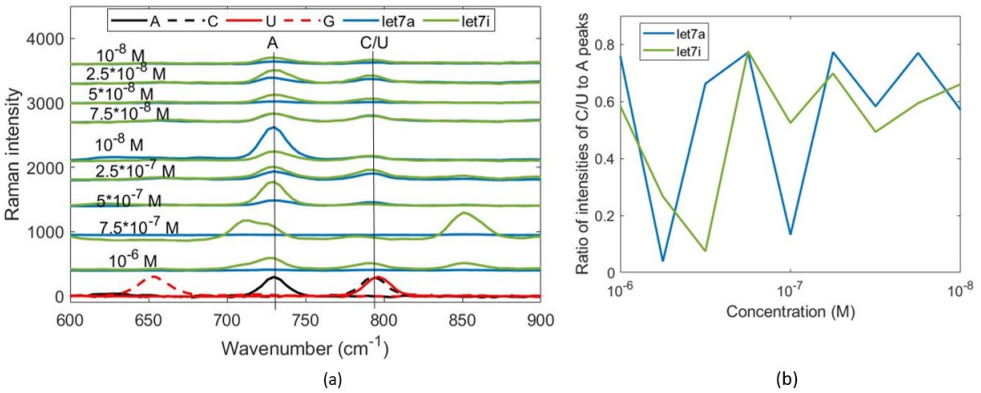

Figure 2.9: (a) The SERS spectra of let7a and let7i at different concentrations measured with AgNPs-LM aggregated by $MgSO_4$. (b) The ratio of the intensity of C/U's (common peak of cytosine and uracil) peak to the intensity of A's (adenine) peak.

For reference, the miRNAs have been also measured with commercial substrates, Silmeco Ag nanorods on the solid surface. Figure 2.10 shows two miRNAs at 10^{-4} to 10^{-7} M concentration measured with the commercial substrates. In general, the results are similar to the ones achieved with AgNPs-LM. The spectra of the highest concentration of miRNAs are left-shifted, so the Raman signal is probably prevailing. The spectra of miRNAs at 10^{-5} and 10^{-6} M contain the expected adenine's and cytosine/uracil's peak. To facilitate a better comparison of peak ratios, these spectra have been normalized based on the adenine's peak. However, the ratio of the cuto-

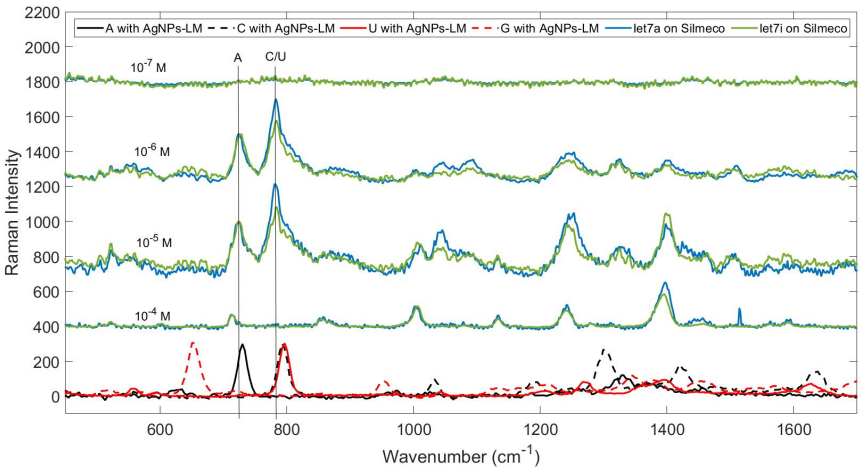

Figure 2.10: The SERS spectra of let7a and let7i at different concentrations measured on the Ag Silmeco commercial substrates. The peaks of A (adenine) and C/U (common peak of cytosine and uracil) are noted. All bases are measured with AgNPs-LM aggregated by $MgSO_4$ and are normalized. SERS spectra of miRNAs are normalized by the A's peak.

sine/uracil's peak around 792 cm^{-1} to the adenine's peak at 734 cm^{-1} is higher for let7a, which does not align with Eq. 2.1. The spectra of miRNAs at 10^{-7} M are not distinctive, indicating that the limit of detection for the commercial substrates falls within the same range as that of the produced AgNPs-LM and AuNPs.

2.4 Conclusion

In conclusion, the produced AuNPs and AgNPs-LM, both aggregated with $MgSO_4$, have demonstrated superior performance among all the combinations of NPs and aggregating agents. The synthesized NPs perform comparably to commercial substrates, but they should be further improved to achieve more sensitive and reproducible detection. Firstly, the achieved LOD of about 10^{-8} M is not sufficient for

the detection of miRNAs because their concentration in body fluids is about $10^{-12} - 10^{-14}M$. Secondly, the random orientation of miRNAs towards metal NPs does not allow the use of the bases' peaks for miRNA discrimination.

One of the possible improvements can be an application of the biological protocols presented in chapter 1 to get not only a target-specific detection but also a more fixed orientation of miRNAs towards NPs. In that case, the intensity of the peaks might offer more reliable insights into the concentration of individual bases within the miRNA and thus be used for miRNA discrimination. Therefore, the application of the capture-based protocol will be presented in the next chapter. Additionally, various strategies for enhancing detection, such as integrating AgNPs-LM with microfluidics and employing TERS probes, will be explored in subsequent chapters.

Chapter 3

Application of the capture-based protocol for miRNAs detection

3.1 Experimental setup and functionalization protocol

In chapter 2, miRNAs have been measured without any biological protocols, but it resulted in the non-fixed orientation of miRNAs and non-specific detection. In this section, the DNAs complementary to the target miRNAs will be used to capture targets. Four oligonucleotides were ordered from Eurofins company: two miRNAs, let7a and let7i, and two fully complementary thiolated DNAs, referred to as DNA7a and DNA7i. The sequences of oligonucleotides are given in Table 3.1.

Table 3.1: Sequence of the miRNAs and DNAs used in the experiments. A - adenine, C - cytosine, G - guanine, U - uracil, T - thymine.

Name	**Sequence**	**Number of A, C, G, U, T**
let7a	5'-UGAGGUAGUAGGUUGUAUAGUU-3'	5, 0, 8, 9, 0
let7i	5'-UGAGGUAGUAGUUUGUGCUGUU-3'	3, 1, 8, 10, 0
DNA7a	5'-thiol-AACTATACAACCTACTACCTCA-3'	9, 8, 0, 0, 5
DNA7i	5'-thiol-AACAGCACAAACTACTACCTCA-3'	10, 8, 1, 0, 3

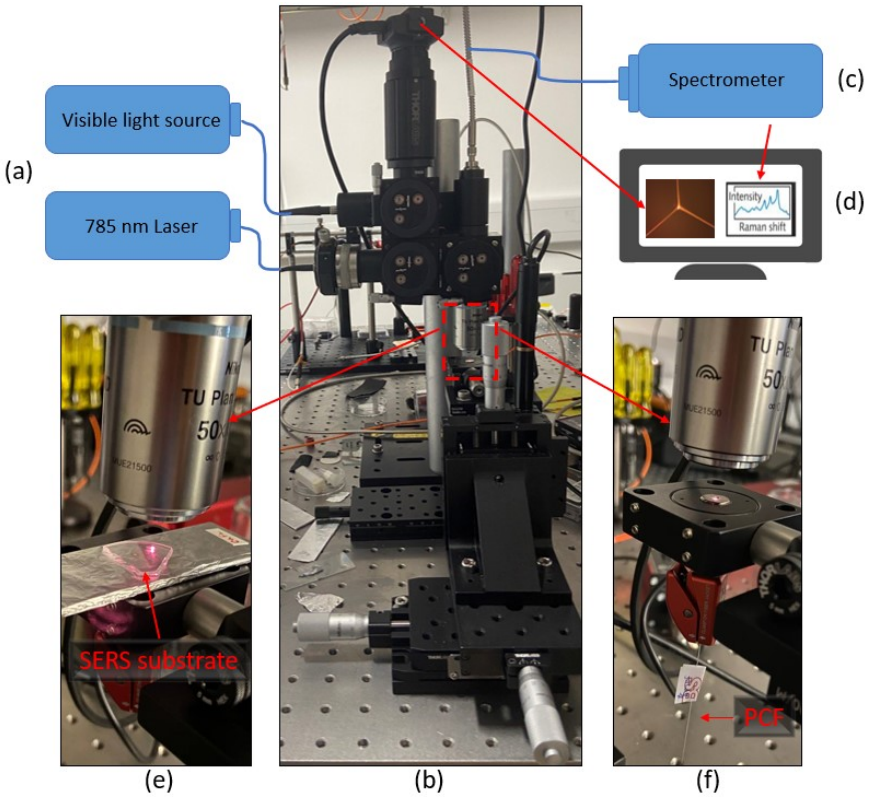

Figure 3.1: Raman setup built at Tyndall National Institute (Ireland) [219, 220] consists of (a) two light sources, (b) a multi-configuration Raman acquisition unit, (c) a spectrometer connected to (d) a computer with software. The acquisition unit can be configured to measure (e) the samples on the solid substrates and inside (f) the Photonic Crystal fibers.

SERS measurements have been performed with a home-built multi-configuration Raman setup developed by [219, 220] and shown in Fig. 3.1. The system consists of two light sources, visible used for camera observations and a 785 nm laser for SERS measurement, a Raman acquisition unit, and a spectrometer connected to a computer with the acquisition software. Two modes of the Raman acquisition unit are used in this thesis: a stage for measurement of the solid and liquid SERS substrates

(Fig. 3.1, e) and a specific fiber's holder for the measurement with Photonic Crystal Fibers (Fig. 3.1, f). SERS measurements have been conducted with 10 mW power, 1200 gr/mm grating, 3 acquisitions, and 10 s acquisition time.

The top-performing NPs from the previous chapter, AgNPs-LM produced using the Lee-Meisel protocol and AuNPs produced using the Turkevich method, are employed in this experiment. The SERS substrate, illustrated in Fig.3.1 (e), was fabricated by depositing a 2 μL droplet of highly concentrated Au/Ag NPs onto a CaF_2 slide and allowing it to dry. Highly concentrated NPs were achieved through centrifugation of 200 μL of the NPs solution at 9800 rpm for 24 minutes, followed by removal of about 195 μL of supernatant. As a result, the NPs left in the pellet are about 40 times more concentrated than in the original solution. Two different methods of immobilizing the capture DNAs on the substrate were investigated. In the first method, 2 μL of each of the two DNAs at a concentration of 0.1 mM were deposited onto the substrate and allowed to dry for 1 hour, anticipating the attachment of DNA molecules to the NPs via their thiol groups. Another approach, adapted from [221], involves the use of tris(2-carboxyethyl)phosphine (TCEP) to achieve a standing configuration of DNAs, facilitating their binding with the target miRNAs. Thus, each of the two DNAs at a concentration of 0.1 mM was mixed with 20 μM TCEP at a 1:1 ratio, resulting in a final concentration of DNAs at 0.05 mM. Subsequently, 2 μL of TCEP-treated DNAs were deposited onto the substrate and left to dry for 1 hour. For SERS measurements, the CaF_2 substrate with the samples was positioned on the glass slide covered by aluminum foil to eliminate the Raman background interference from the glass.

3.2 SERS measurement of DNAs and miRNAs

According to the previous chapter, AgNPs-LM colloidal solution shows the best performance for miRNA detection, followed by AuNPs. In this experiment, the two NPs will be used for the measurement of DNA7a on the CaF_2 substrate. Figure 3.2 presents the SERS spectra of pure and TCEP-treated DNA7a immobilized on AuNPs (a) and AgNPs-LM (b) by following the previously described procedures. As in the

experiments presented in chapter 2, AgNPs-LM have shown better performance for the detection of nucleic acids: there are significant peaks of adenine around 734 and 1331 cm^{-1} in the spectrum of pure DNA7a. The peaks are smaller in the spectrum of TCEP-treated DNA7a probably due to twice less concentration of DNA. AuNPs resulted in a very small adenine's peak only in the spectrum of pure DNA7a. Therefore, in further experiments, the measurements are performed using AgNPs-LM.

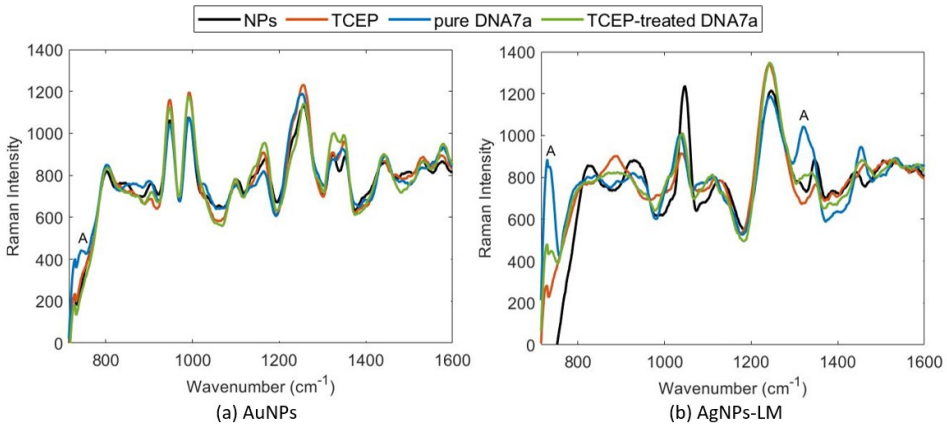

Figure 3.2: The SERS spectra of pure and TCEP-treated DNA7a measured with (a) AuNPs and (b) AgNPs-LM on the CaF_2 slides. The peaks of A (adenine) are noted.

In the next measurement, the immobilized DNAs were rinsed by dropping water and letting it dry for 15 minutes to remove crystalized sediments. Using AgNPs-LM, three trials of measurement of DNA7a and DNA7i (pure and TCEP-treated) have been performed. Figure 3.3 (a,b) shows that the additional washing step resulted in the appearance of a peak around 790 cm^{-1}. It is the combination of thymine's peak around 784 cm^{-1} and C's peak at 792 cm^{-1} [47]. According to Fig. 3.3 (c), the ratio of the intensities of combined C/T's peak to the intensity of A's peak at 734 cm^{-1} for both DNAs varies significantly, but overall it is higher for DNA7i. As can be noticed, the TCEP treatment increases the difference between the ratios for the two DNAs, so the ratio for the TCEP-treated DNA7i has a prominently high value. The expectation was the opposite because the ratio of the number of cytosines and

thymines to the number of adenines in the sequences of DNA7a and DNA7i is 1.44 and 1.10 respectively. As in the previous chapter, the ratio of the peaks was found to be an unreliable parameter for sequence discrimination. However, DNAs can still be used as captures for discrimination of the target miRNAs.

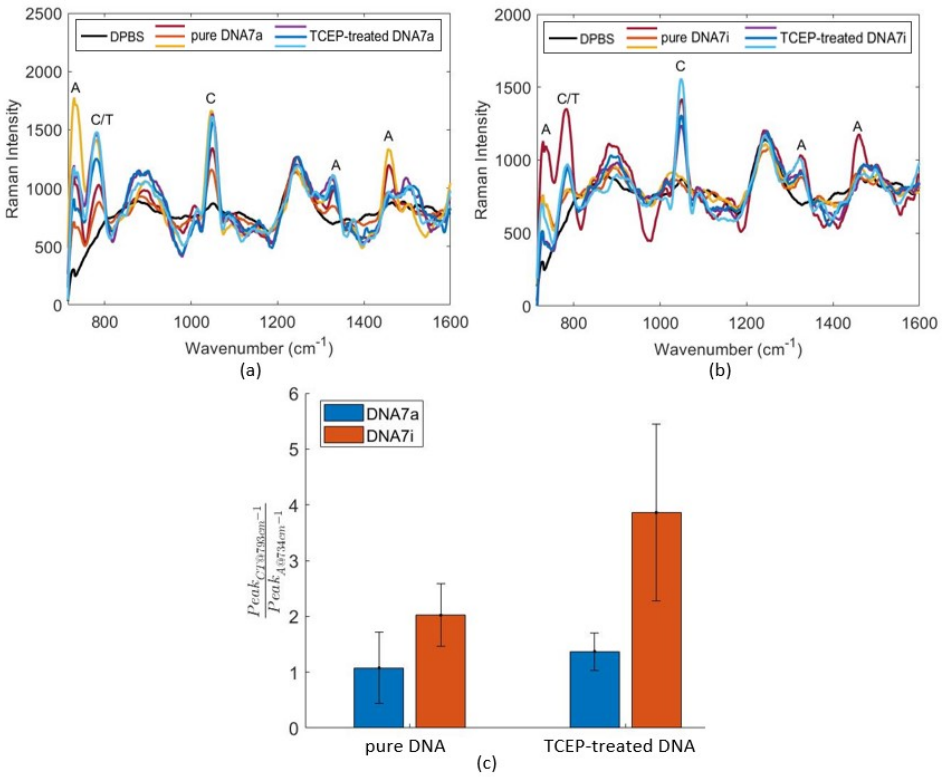

Figure 3.3: The SERS spectra of (a) DNA7a and (b) DNA7i measured with AgNPs-LM on the CaF_2 slides. (c) The ratio of the intensities of the peak of C/T's (cytosine and thymine combined peak) around 790 cm^{-1} to the peak of A (adenine) around 734 cm^{-1} calculated for all pure and TCEP-treated DNAs. The mean and standard deviations are calculated based on 3 trials of each measurement.

The next measurement was aimed at studying the capturing of let7a by both DNAs. After immobilization of pure and TCEP-treated DNA7a and DNA7i by the

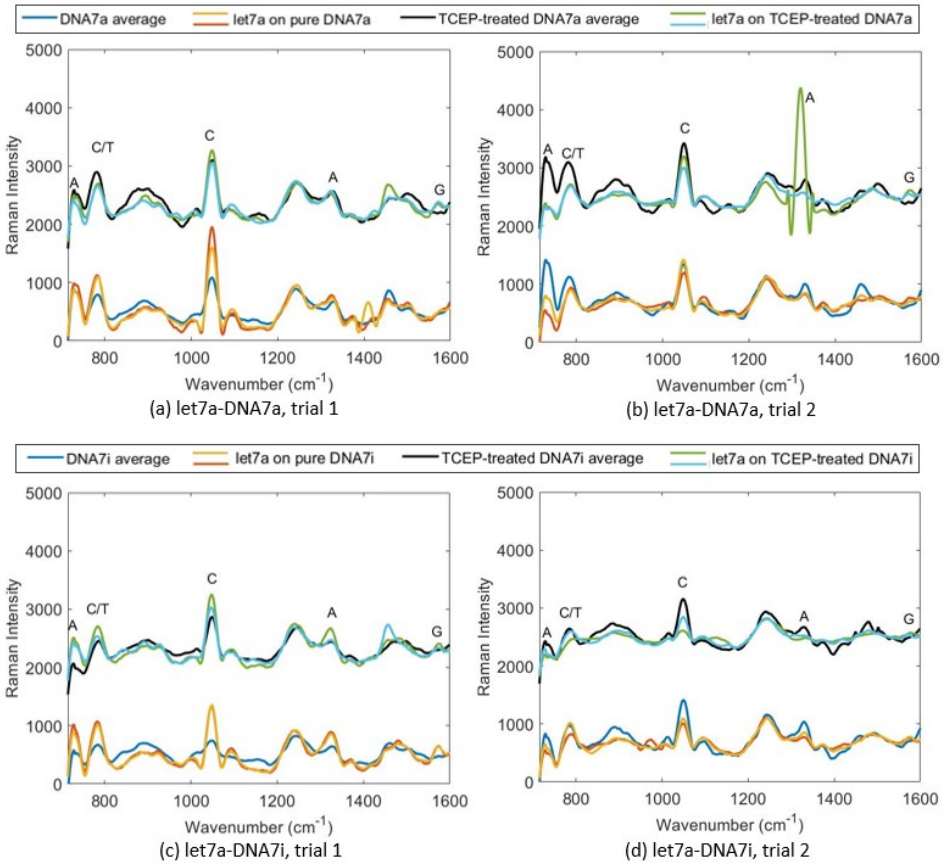

Figure 3.4: The SERS spectra of let7a captured by DNA7a (a,b) and DNA7i (c,d) measured with AgNPs-LM on CaF_2 slides. Two trials have been conducted of each experiment have been conducted. The peaks of A (adenine), C/T (common peak of cytosine and thymine), and G (guanine) are noted.

previous protocol, 2 μL of let7a at $10^{-4}M$ concentration was dropped and left drying for 1 hour. Figure 3.4 illustrates the SERS spectra obtained from two trials of measurement of let7a captured by DNA7a (a,b) and DNA7i (c,d). The spectra of pure and TCEP-treated DNAs are averaged and shown by blue and black lines on each subplot. It should be noted that DNA7a and DNA7i have only 0 and 1 guanine in their

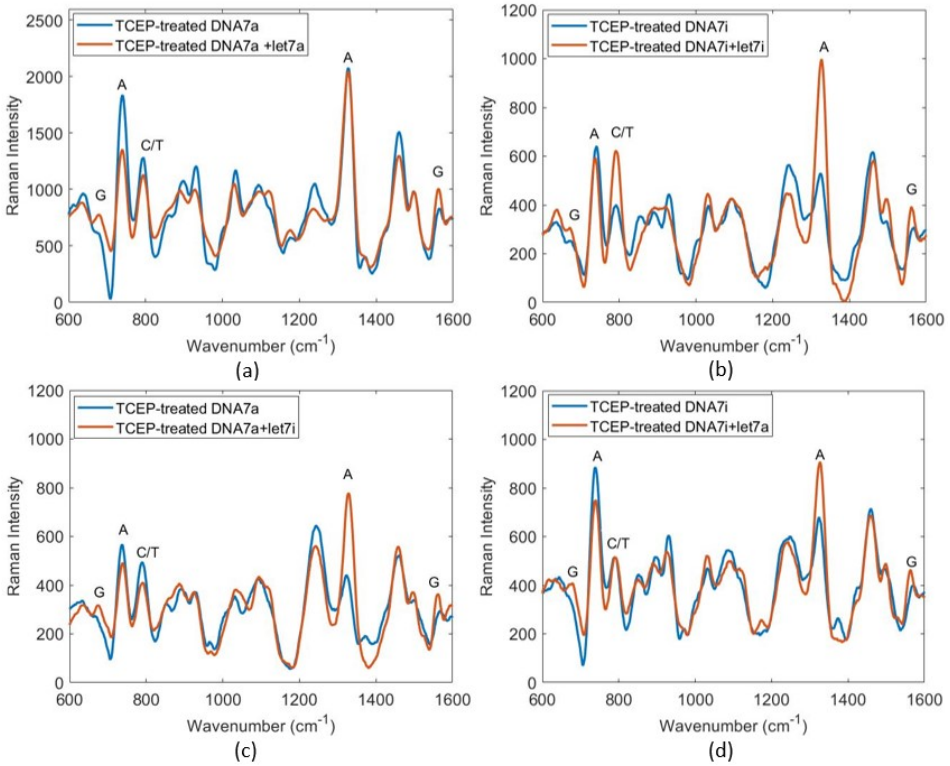

Figure 3.5: The SERS spectra of let7a captured by DNA7a (a) and DNA7i (c) and let7i captured by DNA7a (d) and DNA7i (b). The miRNAs/DNAs were immobilized on AgNPs-LM by long incubation of the CaF_2 slides in their solution. The peaks of A (adenine), C/T (common peak of cytosine and thymine), and G (guanine) are noted.

sequences, so the hybridization with let7a which has 8 guanines should be reflected in the spectrum first of all by the appearance of its peak. Those measurements have been performed in the range of 693.4-2662.4 cm^{-1} due to the original settings of the instrument, so the most prominent guanine's peak around 658 cm^{-1} is out of the range of this measurement. However, an evaluation can be made based on another guanine's peak around 1574 cm^{-1}, which is absent for all spectra with DNAs and starts to appear after the addition of let7a. The peak seems more prominent when the

DNAs are mixed with TCEP because it stimulates the binding with miRNAs. Moreover, the guanine's peak is more intense for the cases when let7a was captured by the fully complementary DNA7a (Fig. 3.4 a,b) rather than by partially complementary DNA7i (Fig. 3.4 c,d): relative intensities are about 150 versus 80-100.

The final measurement was aimed at checking another protocol of the DNAs/miRNAs immobilization on NPs presented by [84]. The CaF_2 slide with AgNPs-LM was immersed into 20 μL solution of TCEP-treated DNA with the concentration of DNA of $1\mu M$ and left for 8-12 hours at room temperature. Then, the slide was washed by immersing it in the well with water for 5 minutes and drying it for 30 minutes. After recording the SERS spectra of TCEP-treated DNA, the slide was further incubated in 20 μL solution of miRNAs at a concentration of $1\mu M$ for 4-6 hours following the wash and dry step. Then, SERS spectra of miRNAs have been recorded. Figure 3.5 illustrates that a long incubation helped to achieve good spectra for low-concentrated sequences: the peaks of all bases are clearly distinguishable. The range of measurement was changed to 221.9-2381.1 cm^{-1} to include the peak of guanine around 658 cm^{-1}. As was expected, this peak is present only when miRNAs are added, but is present both when the target miRNAs are matched with the DNAs (let7a-DNA7a and let7i-DNA7i) and when the sequences are only partially complementary (let7a-DNA7i and let7i-DNA7a).

3.3 Conclusion

In conclusion, this experiment has again demonstrated the superior performance of AgNPs-LM for nucleic acid measurements so they will be used in the next chapter. Measurement with the NPs on the CaF_2 substrate resulted in good SERS spectra for DNAs and miRNAs. Notably, the method of immobilization of DNAs and miRNAs on the substrate influences the sensitivity of SERS measurements. Thus, a long incubation (4-12 hours) of the substrate in each sample of DNAs and miRNAs can provide good spectra at 10^{-6} M concentration, while only 10^{-4} M was detected by dropping the samples on the substrate and leaving it for 1 hour. The hybridization of miRNAs by DNA is detectable by the peak of guanine. However, it is challenging to

distinguish partially mismatched miRNAs from the target due to a lack of sensitivity and reproducibility. The application of PCF for SERS measurement as a way to achieve more sensitive and reproducible results will be explored in the next chapter.

Chapter 4

PCFs as microfluidic devices for the DNA and miRNA detection

4.1 Photonic crystal fibers theory

Photonic crystal fibers (PCFs) are the types of optical fibers that are typically characterized by hollow regions in their cross-section [46]. Due to this feature, PCFs have been widely studied for different applications, including biosensing.

Based on the geometry of PCFs, they are divided into two groups, such as solid-core (SC) and hollow-core (HC) PCFs. There are different types of SC-PCFs and HC-PCFs, some of which are shown in Fig. 4.1. For example, a standard SC-PCF shown in Fig. 4.1 (a) consists of a solid core surrounded by a periodic array of holes. Another type called suspended-core (SuC) PCF has a core suspended in air and held by the three silica struts (Fig. 4.1, b). The standard HC-PCF consists of the hollow core surrounded by the periodic array of holes as shown in Fig. 4.1 (c). Another type of HC-PCF depicted in Fig. 4.1 (d) is called tube lattice fiber (TLF). It consists of a hollow core and some hollow tubes around it.

The light can be guided in PCFs by different mechanisms, including modified total internal reflection (TIR), photonic bandgap, and inhibited coupling [226, 227]. Modified TIR is exploited by some SC-PCFs because their holes-inclusive cladding

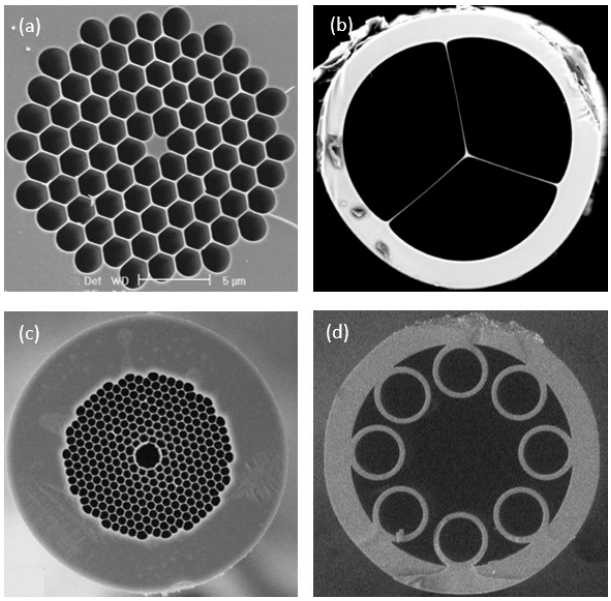

Figure 4.1: Types of PCFs: (a) standard SC-PCF reproduced from [222], (b) suspended-core SC-PCF reproduced from [223], (c) standard HC-PCF reproduced from [224], (d) tube lattice HC-PCF reproduced from [225].

has an effective refractive index lower than that of the solid core [226]. The photonic bandgap mechanism, which is applied in both SC-PCFs and HC-PCFs, relies on the periodic variation in the refractive index within the fiber's cladding. This periodicity leads to the creation of a photonic bandgap, where particular wavelengths of light are not allowed to escape the hollow core and are, thus, effectively trapped within the core [226]. The inhibited coupling confinement mechanism used in HC-PCFs relies on the nature of the coupling between the fundamental mode (FM) of the core and the cladding modes. The inhibited coupling fibers have quasi-continuum cladding modes, some of which exhibit a transverse electric field distribution with rapid spatial oscillations. Those cladding modes have weak coupling with the core's FM, so the latter stays confined inside the core [228].

The hollow regions of PCFs can be used for the incorporation of liquid, and their

interaction with light over the whole length of fiber can be used for different sensing purposes. Since the core of SC-PCFs is solid, the analyte is injected into the holes of the cladding. In that case, it interacts with the evanescent light present in the cladding. On the other hand, the hollow core feature of HC-PCFs allows the incorporation of analytes directly inside the core where it can interact with guided light.

There are many studied applications of PCFs for the measurements of biomolecules, including nucleic acids. For example, DNA can be labeled with a dye, like Cy5, that absorbs light at a particular wavelength range. Then, the aqueous solution of the labeled DNA can be injected into the holes of the standard SC-PCFs. The evanescent light partially absorbed by the dye induces changes in the transmission spectrum, allowing the detection of DNA [229]. Another method is based on the step-by-step immobilization of multiple molecules, including target DNA and its aptamers, inside the TLF in order to form a bio-layer on the fiber's walls. The created layer increases the thickness of the cladding and this small change in geometry results in the detectable shift of transmission spectrum [227, 230].

The PCFs have also been used as a microfluidic platform for the SERS-based measurements of different biomolecules. For example, the detection of haptoglobin has been reached by anchoring AuNPs inside the SuC-PCF and then immobilizing thiol-modified haptoglobin. After that, the injected labeled antibody is captured by the haptoglobin, and the SERS spectrum of the label molecule is detected [223]. The main advantage of using PCFs for SERS measurement is the potential to improve sensitivity and reproducibility due to the increased number of collected photons and the longer interaction area of light with the NPs and analyte in comparison with the single-point SERS measurement [46]. Previous experiments revealed that the tested substrates lacked the sensitivity required for detecting low-concentration miRNAs in body fluids and struggled with reproducibility in distinguishing different miRNAs based on their peaks' ratios. As a result, integrating PCFs with SERS for miRNA measurements can be a promising solution.

In this chapter, two different methods of DNA/miRNA detection inside PCFs will be studied. Firstly, the simulation and experimental results of the SERS-based measurement of DNAs and miRNAs inside SuC-PCFs will be discussed. Then, the

setup and procedure for the transmission spectra shift-based detection inside TLFs will be presented.

4.2 SERS-based measurement of DNAs and miRNAs inside SuC-PCFs

SERS measurements of analytes were conducted inside SuC-PCFs with different core and cladding sizes produced at University of Limoges, France. The PCFs have been selected because of the promising sensitivity, reproducibility, and repeatability that they have shown in the SERS measurement of 4-Aminothiophenol [231]. The measurements were conducted during the secondment at Tyndall National Institute, Cork, Ireland.

4.2.1 Simulations of PCFs

The model used as a reference

Preceding the experimental phase, simulations of PCFs were performed using COMSOL to identify optimal parameters, including NPs concentration and PCF dimensions. The simulation model used in this study was adapted from the model originally proposed by Beffara [46]. As illustrated in Figure 4.2, Beffara's approach involves representing SuC-PCF as a step-index fiber (SIF) with a silica core and hollow cladding filled with water to emulate biofluid. Additionally, an effective layer is introduced where metallic NPs are anchored to the core, facilitating interaction with the evanescent field and analyte. The effective layer, which thickness is approximated as twice the radius of the NPs, is made of a composite material. Its dielectric constant can be determined using the following equation:

$$\varepsilon_{eff}(\lambda) = \varepsilon_w(\lambda)\frac{\varepsilon_m(\lambda)+2\varepsilon_w(\lambda)+2f(\varepsilon_m(\lambda)-\varepsilon_w(\lambda))}{\varepsilon_m(\lambda)+2\varepsilon_w(\lambda)-f(\varepsilon_m(\lambda)-\varepsilon_w(\lambda))} \tag{4.1}$$

In this equation, $\varepsilon_w(\lambda)$ and $\varepsilon_m(\lambda)$ are the electric permitivities of water and metal NPs respectively, and f is a filling factor of NPs. The electric permittivities at a spe-

cific wavelength can be found in the database [232]: $\varepsilon_w(\lambda)$ from Hale and Querry and $\varepsilon_m(\lambda)$ from Rakic. The calculated dielectric constant is used to find the refractive index of the effective layer.

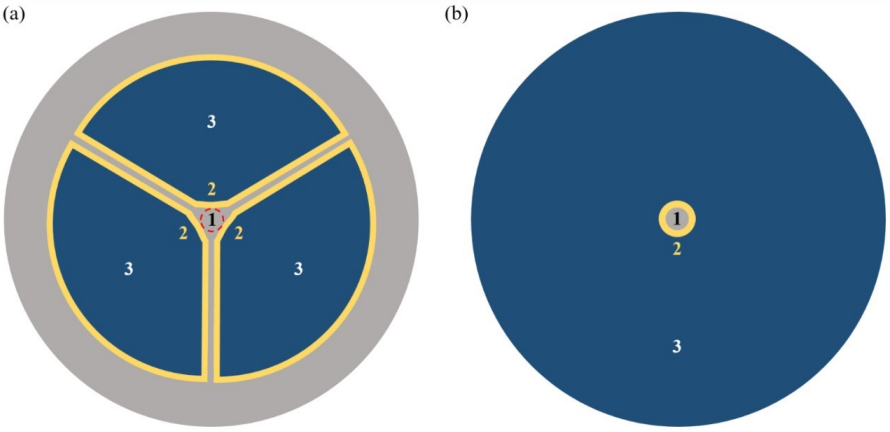

Figure 4.2: (a) Schematics of the model that can be used to correspond closely to the real SuC PCF. (b) Schematics of the SIF approximation that has been simulated by Beffara. In both schematics, 1 (gray) represents the silica region, 2 (yellow) represents the effective layer and 3 (blue) represents water. Reproduced from [46].

The factor proportional to the Raman intensity (F_{RI}) can be calculated by the following equation:

$$F_{RI} = P_{sur} L_{fiber} CD \left[\eta_{eff} \frac{1 - e^{-\alpha L_{fiber}}}{\alpha L_{fiber}} \right]^2 \tag{4.2}$$

It can be seen, that the Raman intensity depends on the fiber's parameters, such as its length (L_{fiber}) and the perimeter of the effective layer's surface (P_{sur}). It also depends on the cover density of NPs (CD), the power of the evanescence field in the effective layer (η_{eff}), and the attenuation coefficient ($\alpha = \frac{4\pi}{\lambda} Im(n_{eff})$).

Suspended-core PCFs model development

To create a more realistic representation of the SuC-PCF, a comprehensive model will be constructed and simulated within COMSOL. As depicted in Figure 4.3 (a), this model comprises a silica core with a diameter D_{core} connected to three silica struts with a thickness of T_{strut} and three holes filled with water, each with a diameter of D_{hole}. The core of the fiber is envisioned as a circle inscribed within the triangular arrangement of the three holes, as illustrated in Figure 4.3 (b), where OK corresponds to the half of D_{core}.

Figure 4.3 (c) shows that the effective layer is drawn by inscribing the composite shape $A_1B_1K_1C_1D_1$ within each hole, offset by twice the radius of the immobilized metal NPs. So, the thickness of the effective layer $T_{eff} = 2 \times R_{NPs}$. The outer layer is omitted from the model because the light beam is significantly smaller than the outer layer's radius, making it reasonable to assume that light does not reach this region.

Figure 4.3 (d) demonstrates the progressive stages of the model's development. Initially, a one-third segment of a circle with a radius $R_{hole} = \frac{D_{hole}}{2}$ was drawn. To form the struts, two rectangles, each with a thickness of $t = \frac{T_{strut}}{2}$ were then subtracted from both sides of this sector. The core was shaped by rounding the upper angle $\angle$BLC by incorporating the arc BKC achieved using the fillet function. The function requires the radius of the arc R_{fillet}, and its calculation becomes a geometric problem. The problem is solved step by step using the schematics in Fig. 4.3 (d):

- Rectangle ANOM: $AN = OM = t$; $AO = R_{hole}$; $\angle AON = \alpha = arcsin(\frac{t}{R_{hole}})$; $NO = AM = t \times cot(\alpha)$
- Quadrilateral $BLCO_1$: $\angle BLC$ is 120°, as BL and LC are parallel to NO and OS, which form a one-third of the circle; angles $\angle O_1CL$ and $\angle O_1BL$ are right, so $\angle BO_1C = 60°$. Thus, $\triangle O_1BC$ is equilateral and $O_1B = O_1C = BC = R_{fillet}$.
- Right triangle $\triangle$LHC scaled and drawn separately: $\angle HLC = \frac{\angle BLC}{2} = 60°, HC = \frac{BC}{2} = \frac{R_{fillet}}{2}, LK = OK - OL = \frac{D_{core}}{2} - \frac{2t}{\sqrt{3}}, KH = O_1K - O_1H = R_{fillet} - \frac{\sqrt{3}}{2}R_{fillet}$.
- Right triangle $\triangle$OML scaled and drawn separately: $\angle MLO = \angle HLC = 60°$, $OM = t, LM = OM \times\ cot(60°) = \frac{t}{\sqrt{3}}, OL = \frac{OM}{sin(60°)} = \frac{2t}{\sqrt{3}}$.

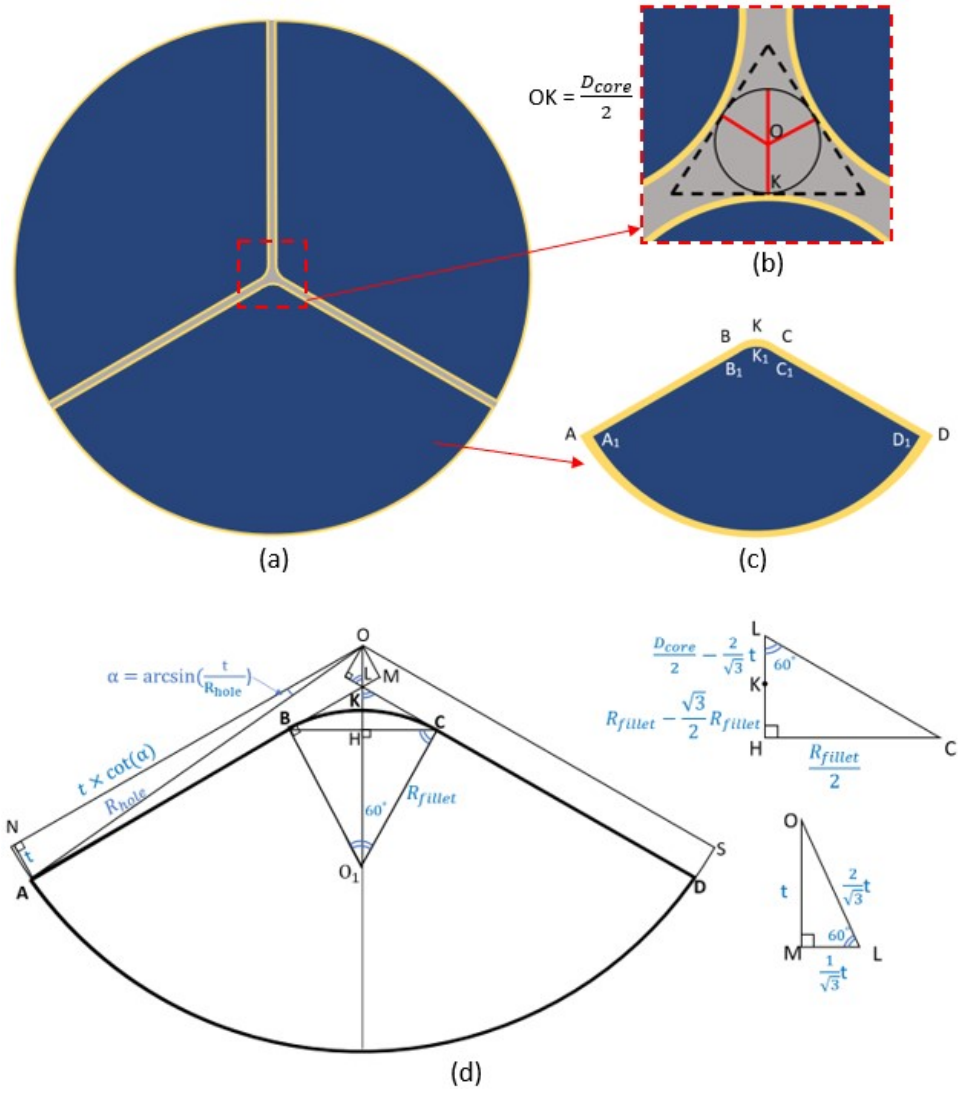

Figure 4.3: Development of a SuC-PCF's model in COMSOL: (a) the model of SuC-PCF consisting of silica core and struts (gray), holes filled with water (blue), effective layer (yellow); (b) schematics of the core; (c) schematics of the hole and effective layer; (d) schematics of the calculations to construct the hole.

Finally, the following relation within triangle △LHC can be used to determine R_{fillet}:

$$\frac{LK+KH}{HC} = cot(60^\circ) \tag{4.3}$$

$$\frac{\frac{D_{core}}{2} - \frac{2t}{\sqrt{3}} + R_{fillet} - \frac{\sqrt{3}}{2}R_{fillet}}{\frac{R_{fillet}}{2}} = \frac{1}{\sqrt{3}} \tag{4.4}$$

$$R_{fillet} = \frac{\sqrt{3}D_{core} - 4t}{4 - 2\sqrt{3}} \tag{4.5}$$

After the construction of the model's geometry, the material properties should be assigned to each region. The core and struts are made from silica, the holes are filled with water considering that the analyzed samples will be dissolved in water and injected into the holes. The effective layer is a composite of metal NPs immobilized on the surface and water. The refractive index of silica (n_{Si}) for a specific wavelength can be determined using the Sellmeier equation [233]. The refractive indices of water and the effective layer are derived from the square root of their respective dielectric constants, $\varepsilon_w(\lambda)$ and $\varepsilon_{eff}(\lambda)$. The value of $\varepsilon_{eff}(\lambda)$ is computed using equation 4.1, in which the filling factor f depends on the volume of all NPs (V_{NPs}) and the volume of the effective layer (V_{eff}) as follows: $f = \frac{V_{NPs}}{V_{eff}}$. The V_{NPs} can be found by multiplying the volume of each spherical NP by the number of NPs, which, in turn, depends on the CD and the perimeter of the effective layer over the length of the fiber:

$$V_{NPs} = \frac{4}{3}\pi R_{NP}^3 \times CD \times P_{sur} \times L_{fiber} \tag{4.6}$$

In this equation, the NPs' radius and CD, as well as the fiber's length are given, while P_{sur} can be computed. According to Fig. 4.3 (c,d), P_{sur} can be calculated by finding the perimeter of the ABKCD curve multiplied by 3 to consider all 3 holes. $P_{sur} = 3 \times (L_{AD} + L_{BC} + 2 \times L_{AB}) = 3 \times (L_{AD} + L_{BC} + 2 \times (L_{AM} - L_{BL} - L_{LM})) = 3 \times (R_{hole} \times (\frac{2\pi}{3} - 2\alpha) + R_{fillet} \times \frac{\pi}{3} - 2 \times (t \times cot(\alpha) - \frac{t}{\sqrt{3}} - \frac{R_{fillet}}{\sqrt{3}}))$.

The V_{eff} can be found by multiplying the area (A) of the effective layer by the fiber's length. The effective layer is a region enclosed between ABKCD and $A_1B_1K_1C_1D_1$, so the V_{eff} is found by the following formula:

$$V_{eff} = (A_{ABKCD} - A_{A_1B_1K_1C_1D_1}) \times L_{fiber} \tag{4.7}$$

According to Fig. 4.3 (d), $A_{ABKCD} = \frac{1}{3}A_{circle} - 2A_{ANOM} + 2A_{\triangle OLM} - A_{BLCJ} + A_{BKCJ} = \frac{\pi R_{hole}^2}{3} - 2R_{hole} \times t + \frac{t^2}{\sqrt{3}} - \frac{2R_{fillet}^2}{\sqrt{3}} + \frac{\pi R_{fillet}^2}{6}$. The value of $A_{A_1B_1K_1C_1D_1}$ can be found by replacing R_{hole} with $R_{in} = R_{hole} - (\frac{4}{\sqrt{3}} + 2) \times R_{NPs}$.

The model can be further applied for simulation after inserting the initial parameters and selecting the mesh (free triangular in this case).

Result of the simulation

Two models, the SIF approximation presented by Beffara and the newly developed SuC-PCF model have been simulated. The values of the parameters are selected based on the available equipment and fibers: $\lambda = 785\ nm, n_{Si} = 1.4536, \varepsilon_w(785) = 1.7678 + 3.6910 \times 10^{-7} \times i$. In chapters 2 and 3, it was demonstrated that AgNPs-LM exhibited the best performance for miRNA detection, thus making them the choice for the upcoming experiments involving PCFs. The AgNPs-LM were characterized by $\varepsilon_{AgNPs} = -23.821 + 1.7882 \times i$ and $R_{AgNPs} = 50\ nm$. Three types of PCFs are available, each with distinct specifications: PCFs with $D_{core} = 2\ \mu m$, $D_{hole} = 90\ \mu m$, $T_{strut} = 0.86\ \mu m$, PCFs with $D_{core} = 3\ \mu m$, $D_{hole} = 150\ \mu m$, $T_{strut} = 0.5\ \mu m$, PCFs with $D_{core} = 3.5\ \mu m$, $D_{hole} = 150\ \mu m$, $T_{strut} = 0.55\ \mu m$. The experiments involve varying the fiber's length within the range of 5 to 15 cm and the CD from 0.01 to 20 $\frac{NPs}{\mu m^2}$ to maximize the Raman intensity (F_{RI}). All parameters used in the simulation are listed in Table 4.1. Figures 4.4-4.7 provide a comprehensive comparison between the results obtained by simulating the SIF and SuC-PCF models.

Figures 4.4 and 4.5 show the field distribution in PCFs obtained by both models at CD=0.01 and 20 $\frac{NPs}{\mu m^2}$ respectively. As can be seen, the field distribution in SIF-approximated PCFs is similar regardless of the difference in geometry and CDs. In the SuC-PCF model, the field varies with the geometry of the core, and its con-

Table 4.1: Parameters used for the simulation of three PCFs using SuC-PCF model.

Parameter	**Segment or region from Fig. 4.3**	**PCF 1**	**PCF2**	**PCF3**
D_{core}	$2 \times OK$	2 μm	3 μm	3.5 μm
D_{hole}	$2 \times OA$	90 μm	150 μm	150 μm
T_{strut}	AN	0.86 μm	0.5 μm	0.55 μm
λ	-	785 nm		
$n_{Si}(785nm)$	Gray region	1.4536 [233]		
$\varepsilon_w(785)$	Blue region	$1.7678 + 3.6910 \times 10^{-7} \times i$ [232]		
$\varepsilon_{AgNPs}(785)$	Yellow region	$-23.821 + 1.7882 \times i$ [232]		
$R_{AgNPs}(785)$	-	50 nm		
T_{eff}	$BB_1 = 2 \times R_{NPs}$	100 nm		
L	-	5, 10, 15 cm		
CD	-	$0.01 - 20 \frac{NPs}{\mu m^2}$		

finement changes with CDs. Moreover, at CD=20 $\frac{NPs}{\mu m^2}$ the field in the smallest fiber extends beyond the core into the end of struts (see Fig. 4.5). This PCF has the largest struts-to-core size ratio, so the field escapes from the small core into the large struts. The SIF model, having no struts, is not able to consider this scenario showing that the field remains concentrated within the core.

Figure 4.6 presents the percentage of field in the silica region ($\eta_{core,struts}$) and the effective layer (η_{eff}) relative to the CD. This percentage is an overlap calculated in COMSOL as a ratio of the average field in the region over the field in the whole PCF. The decrease in $\eta_{core,struts}$ and the opposite increase of η_{eff} for all PCFs is explained by losses of guided light due to the interaction with NPs. The sharp decrease of $\eta_{core,struts}$ at CD=19.1 $\frac{NPs}{\mu m^2}$ in the smallest PCF of the SuC-PCF model signifies a significant change in the field distribution. According to Fig. 4.5, this is because of the migration of the field from the core to one of the struts. The graph still shows the presence of 60% of the field in the silica region, but it is all concentrated in silica struts, so the light is no longer guided. Thus, 19.1 $\frac{NPs}{\mu m^2}$ is the limit of NP concentration

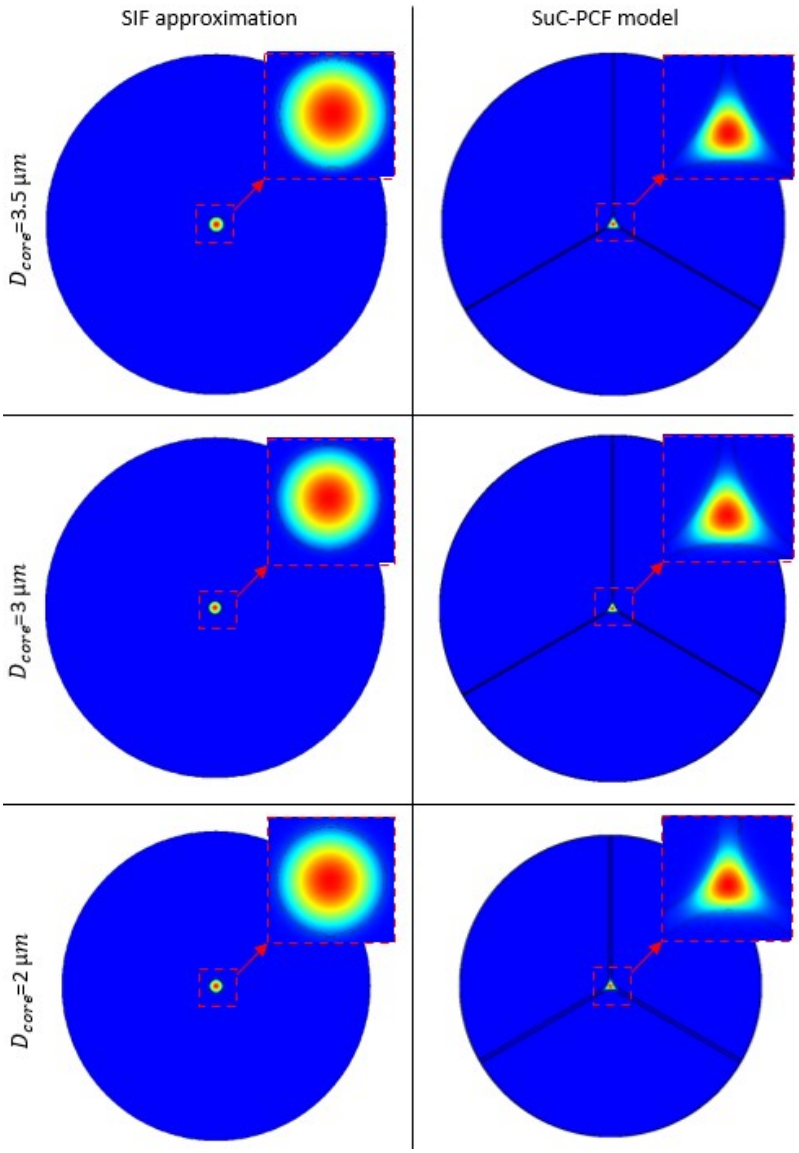

Figure 4.4: Field distribution within the PCFs at CD=0.01 $\frac{NPs}{\mu m^2}$ obtained using the SIF approximation (left) and developed SuC-PCF model (right).

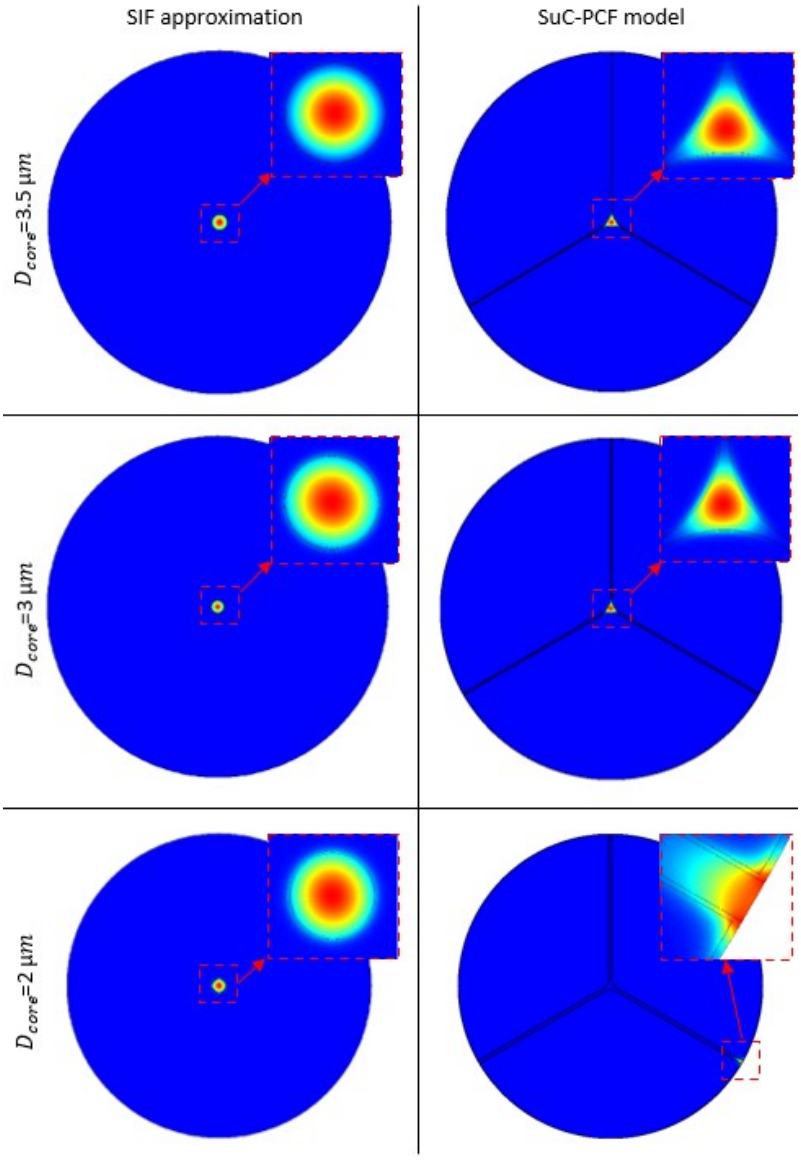

Figure 4.5: Field distribution within the PCFs at CD=20 $\frac{NPs}{\mu m^2}$ obtained using the SIF approximation (left) and developed SuC-PCF model (right).

for the good performance of PCFs with $D_{core} = 2\ \mu m$. The presented SuC-PCF model considers the struts and the core's non-circular geometry, so it should provide more accurate information and be more suitable for the simulation of real fibers.

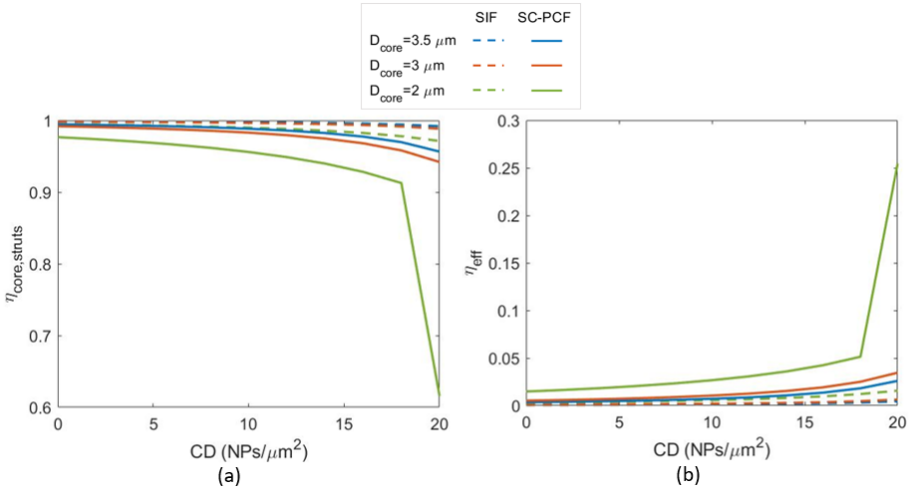

Figure 4.6: Field distribution in the (a) silica region $\eta_{core,struts}$ and (b) effective layer η_{eff} of the PCFs obtained using the SIF approximation and the developed SuC-PCF model.

Figure 4.7 presents the factor proportional to Raman intensity, denoted as F_{RI}, plotted against the CD, as obtained by simulating two models. Initially, in all PCFs, the intensity grows because of the increasing field within the effective layer and subsequently more light interaction with NPs and analytes. However, as CD further increases the losses from NPs start to prevail, so a significant decline of the F_{RI} is observed. The effect of length variation follows a similar trend in both models. At smaller CDs, longer PCFs provide larger F_{RI} due to the extended area for light, NP, and analyte interaction. As CD increases, high losses due to the long light path outweigh the advantage of the extended area of interaction, so shorter PCFs perform better. The SuC-PCF model suggests longer PCFs are preferable only at CDs below approximately 1 $\frac{NPs}{\mu m^2}$, and the SIF model extends this range up to 5 $\frac{NPs}{\mu m^2}$.

According to Fig. 4.7, the optimal size of the PCF also depends on the CD. At

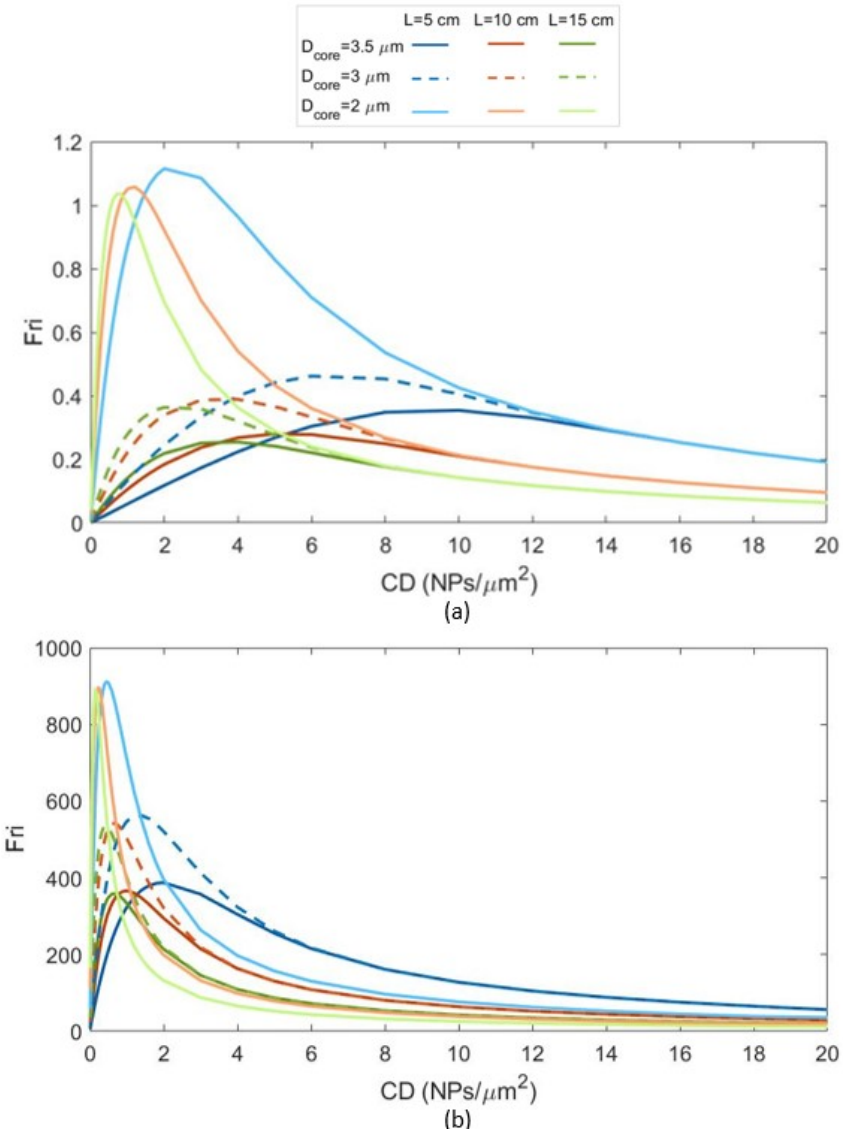

Figure 4.7: Factor proportional to Raman intensity F_{RI} over cover density (CD) obtained for PCFs with different core sizes and lengths by simulating (a) the SIF and (b) SuC-PCF models.

lower CDs, fibers with a $D_{core} = 2\ \mu m$ demonstrated the best performance. At larger CDs, the two models provide different predictions. The SIF model indicates that the core size of the fiber does not affect its performance. It is supported by Fig. 4.5, where all SIF-modeled PCFs have similar field distributions at CD= 20 $\frac{NPs}{\mu m^2}$. The SuC-PCF model suggests that the PCFs with $D_{core} = 3\mu m$ and 3.5 μm show the same performance, while the PCF $D_{core} = 2\mu m$ is expected to provide lower F_{RI}.

Thus, the SIF model suggests that the PCF with a $D_{core} = 2\mu m$ and a length of 5 cm demonstrates the best performance for CDs exceeding 2 $\frac{NPs}{\mu m^2}$, covering most of the range. At CDs larger than 14 $\frac{NPs}{\mu m^2}$, the other two PCFs achieve the same performance and the three fibers can be used interchangeably. On the other hand, the SuC-PCF model predicts that a 5 cm long PCF with $D_{core} = 3\ \mu m$ maximizes F_{RI} for all CDs larger than 2 $\frac{NPs}{\mu m^2}$. PCF with $D_{core} = 3.5\ \mu m$ becomes also an option at CDs exceeding 5 $\frac{NPs}{\mu m^2}$. Consequently, the two models resulted in two different conclusions, highlighting the necessity for experimental validation to determine the model that offers a closer prediction.

4.2.2 SERS measurements in the PCFs

Functionalization of PCFs

There are two ways of immobilization of NPs inside the PCFs, such as injection and anchoring [46]. In the injection method, NPs are mixed with the analyte solution and injected into the PCF. This results in the NPs being distributed freely within the holes of the fiber. In the anchoring method, the PCF's surface is initially silanized, and NPs are then anchored to the walls of the fiber's holes. Then, the aqueous solution of the analyte is injected and the SERS measurement is conducted. The injection method is more suitable for direct detection of the target, as it can be challenging to immobilize DNAs on NPs in a solution. The anchoring method allows the immobilization of the capture DNAs on the anchored NPs and the subsequent injection of the target miRNAs.

In this experiment, the following anchoring method will be used for the SERS measurement:

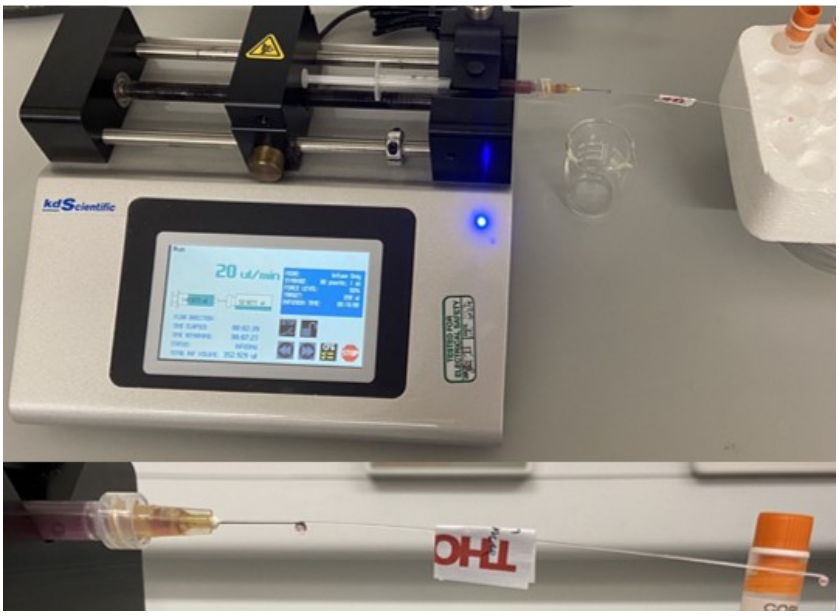

Figure 4.8: Setup for the injection of solutions into the PCFs.

- Preparation of PCFs: Cleaning the PCF by pumping acetone into the PCF at 40 $\mu L/min$ for 10 min, and then drying the PCF by injecting air for 5 minutes. Silanization of the PCF by injecting 2% of APTES in acetone at 40 $\mu L/min$ for 30 min and leaving the solution inside the PCF for 24 hours. Washing by pumping acetone again to remove any unbound molecules of APTES, then drying.

- NPs immobilization: Injecting the colloidal solution of AgNPs at 20 $\mu L/min$ for 30 min and leaving the solution inside the PCF for 24 hours. Washing by pumping deionized water at 40 $\mu L/min$, then drying.

- DNAs immobilization: Injecting $10^{-4}M$ solution of DNAs into the PCF at 20 $\mu L/min$ for 30 min and leaving the solution inside the PCF for 8-12 hours. Washing by pumping deionized water at 40 $\mu L/min$, then drying.

- miRNAs capturing: Injecting $10^{-4}M$ solution of miRNAs into the PCF at 20

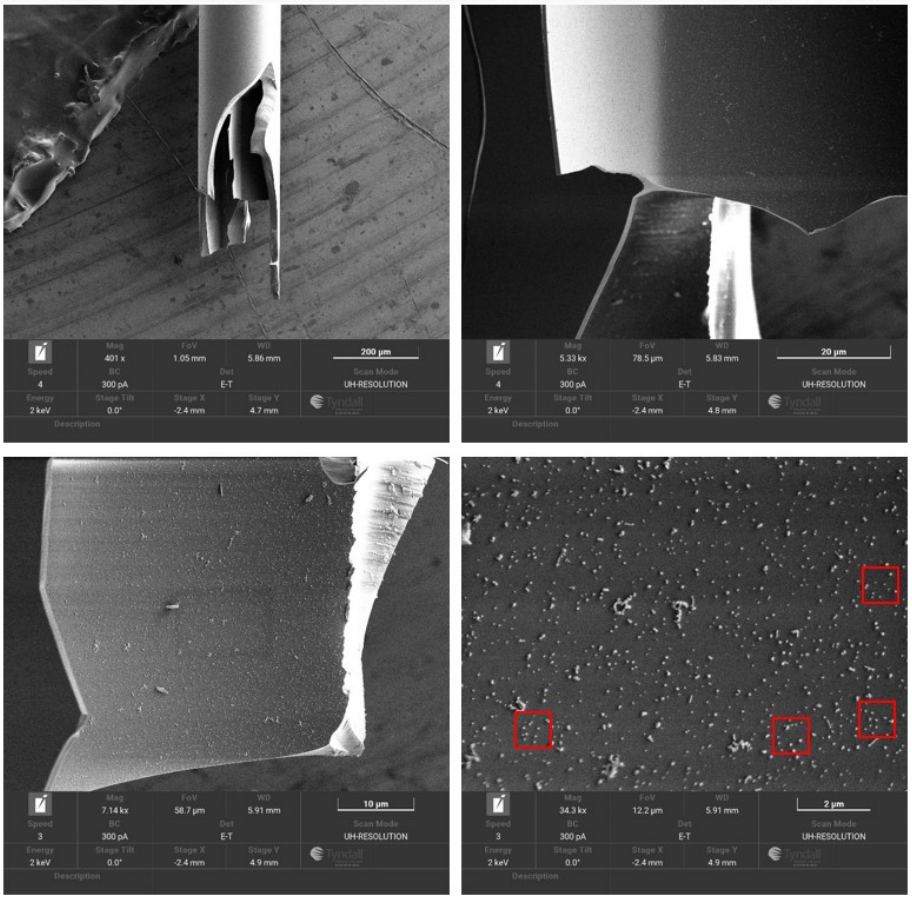

Figure 4.9: The SEM images of the PCF with anchored AgNPs-LM.

$\mu L/min$ for 30 min and leaving the solution inside the PCF for 8-12 hours.

The injection of all solutions was conducted by using a 25G medical needle: a solution was filled into the syringe, then the PCF was inserted into the needle from one end. The syringe was fixed on a pumping system shown in Fig. 4.8, where the rate and volume of injection can be controlled.

In Figure 4.9, the SEM images of the PCF with AgNPs anchored inside it are presented at various scales. These images were captured by intentionally breaking

one end of the PCF. The CD of NPs was determined by analyzing 1 μm by 1 μm squares at four randomly selected locations within the SEM image with the highest magnification. The estimated CD of approximately 13 $\frac{NPs}{\mu m^2}$ will serve as a constant for future analyses.

Measurements of adenine

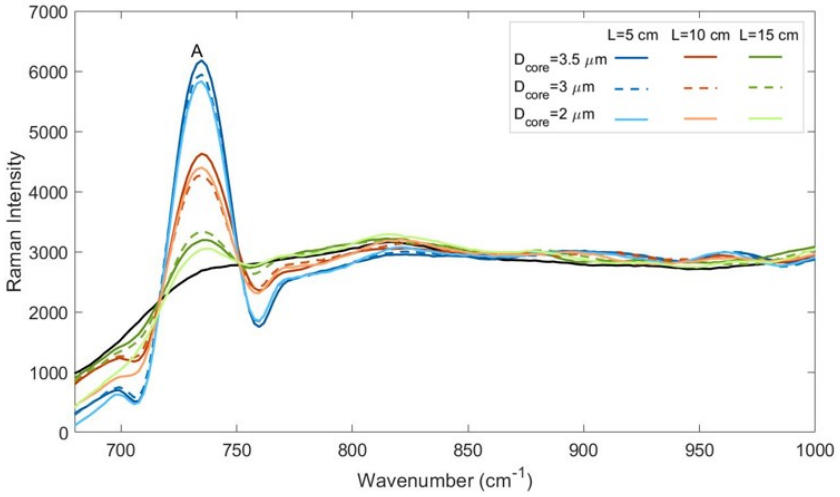

Figure 4.10: SERS measurement of adenine in PCFs with the three different core sizes and three different lengths.

The initial SERS measurement using PCFs aimed to validate the simulations discussed earlier. Adenine at a concentration of $10^{-4}M$ was injected into three PCFs anchored with AgNPs. These PCFs initially had a length of 15 cm and then, to study the influence of the fiber's length, the PCFs were cut twice to 10 cm and 5 cm. Figure 4.10 depicts the SERS spectra of adenine recorded in PCFs of varying lengths. Notably, the length of PCF significantly affects the intensity of the adenine's peak, with shorter PCFs yielding higher peak intensities. The core size demonstrates negligible influence on the peak's intensity. Both findings are in agreement with the results of the simulation of both models obtained at CD=13 $\frac{NPs}{\mu m^2}$ as shown in Fig.4.7. There-

fore, both models provide sufficiently accurate information for the PCF simulation at large CDs.

The selection of PCFs with optimal parameters was based on simulation results, experimental findings, and practical considerations. PCFs with $D_{core} = 2\ \mu m$ were not considered due to lower performance and the practical difficulty of injecting samples into such small cores. The difference between $D_{core} = 3\ \mu m$ and $3.5\ \mu m$ PCFs is minimal, but since more PCFs with $D_{core} = 3\ \mu m$ were available, they were selected for subsequent experiments. Regarding length, while the best results are achieved with 5 cm long PCFs, practical limitations arise: the fiber holder's depth is about 5 cm, making manipulations challenging. Moreover, trimming the ends before each measurement reduces the length, so PCFs of approximately 8 cm will be used for SERS measurements of DNAs and miRNAs.

Measurements of miRNAs and DNAs

Two trials of SERS measurement of miRNAs have been performed and the results are illustrated in Fig. 4.11. In each trial, one PCF with anchored NPs was used for the three subsequent measurements of the following: water (reference), 10^{-4} M thiolated DNA7a immobilized on NPs, and 10^{-4} M let7a captured by DNA7a. In both trials, the measurement of DNA7a alone and with captured let7a provide similar spectra with a peak around 734 cm^{-1}. It corresponds to the peak of adenine that is not present in the reference spectrum of water. The similarity of the results achieved in the two trials shows a good reproducibility of the measurements. However, the intensity of the peak is very small considering the high concentration of the nucleic acids. Moreover, there are no noticeable differences in the spectra of DNA alone and DNA with let7a, like it was in the measurement with CaF_2 substrates.

In the last measurement, the injection and anchoring methods were combined to achieve better performance of PCFs. DNA7a mixed with AgNPs-LM were injected inside the PCF with already anchored NPs. According to Fig. 4.11, the intensity of the adenine's peak is, indeed, significantly higher. However, even this spectrum does not contain prominent peaks of other bases making it hard to distinguish between the two different nucleic acids and the occurrence of the hybridization event.

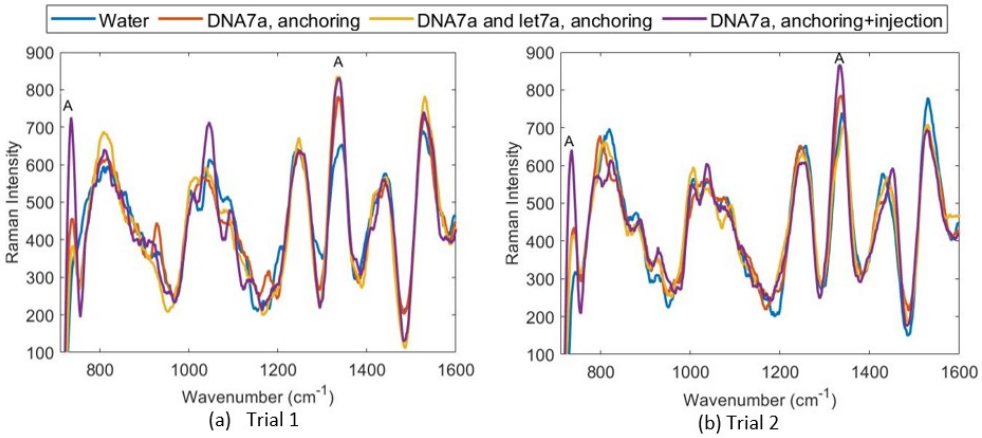

Figure 4.11: SERS measurement of DNA7a and let7a inside the PCF with $D_{core} = 3\ \mu m$ and L=8 cm: (a) trial 1, (b) trial 2. The peaks of A (adenine) are noted.

Figure 4.12 illustrates the comparison of SERS spectra of DNA7a and let7a at 10^{-4} M measured on the CaF_2 substrate and inside PCF anchored with AgNPs-LM. The spectra measured on the substrate and inside PCF have different backgrounds because of the additional SERS signal from the substrate and fiber itself, so the respective reference spectrum of water was subtracted. The original spectra measured on the substrate are taken from Fig. 3.4 (b) in Chapter 3. The spectra obtained from measurements in PCF are taken from Fig. 4.12 (a). The spectra measured with PCFs via anchoring DNA and miRNA have slightly lower intensity than the ones obtained on the CaF_2 substrate. The spectrum of DNA7a measured by injecting the sample into the PCF with already anchored DNA7a resulted in the peak of adenine having almost the same intensity as it is in the spectra measured on the substrate. The common peak of cytosine/thymine/uracil in the spectra measured inside PCF starts to appear when the reference spectrum is subtracted, but it is left-shifted with respect to this peak in the spectra obtained on the substrate. Thus, fabrication and measurement procedures should be optimized to obtain more promising results.

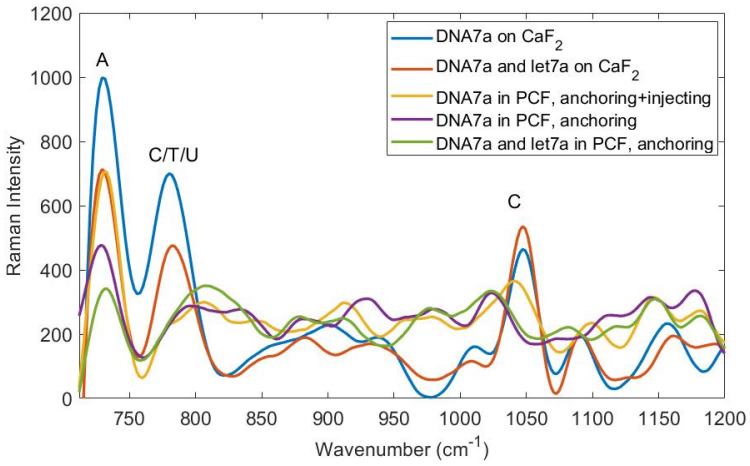

Figure 4.12: Comparison of the SERS spectra of DNA7a and let7a measured on CaF_2 substrate with AgNPs-LM and in PCF with anchored AgNPs-LM obtained by subtracting the respective spectrum of water from each spectrum. The peaks of A (adenine), C (cytosine), T (thymine), and U (uracil) are noted.

4.3 Transmission spectra shift-based measurement of DNAs in HC-PCFs

This section presents another PCF-based setup for the measurement of nucleic acids, namely DNA. The setup is based on the formation of a bio-layer on the inner walls of HC-PCFs. The bio-layer is created by the step-by-step functionalization of the PCFs consisting of the following steps: cleaning, surface silanization, immobilization of the peptide nucleic acid (PNA), capturing of the target DNA by the PNA, binding of DNA with the second biotinylated PNA, and capturing of the streptavidin by biotin. The formed bio-layer increases the thickness of the cladding and changes its effective refractive index leading to a detectable shift of transmission spectrum [227]. The transmission spectrum is recorded after each functionalization step to evaluate its shift in response to a newly formed layer. Good reproducibility is crucial to achieve reliable results, so the same conditions must be preserved at each measurement step.

This same condition is ensured by exciting the same mode in all measurements, and the FM is selected as a reference. The optical setup used to record the transmission spectrum has two limitations: an excitation of the FM is difficult and the method of checking the mode is not sufficiently reliable. The transmission spectrum shift-based method for DNA measurement has been presented by Khozeymeh *et al.* [227]. This section discusses the ways of improving the optical setup to solve the two mentioned challenges and achieve better reproducibility of DNA detection inside HC-PCFs.

4.3.1 HC-PCF for DNA detection

The type of HC-PCF used in this experiment is TLF which consists of a silica hollow cylinder and multiple smaller hollows attached to its inner side (see Fig. 4.13). The number of holes in the cladding can vary, but in this experiment, TLF with 6 holes (TLF-6) will be used. The holes have a radius of 12 μm and a thickness of 1.5 μm, and the radius of the core is 17.5 μm.

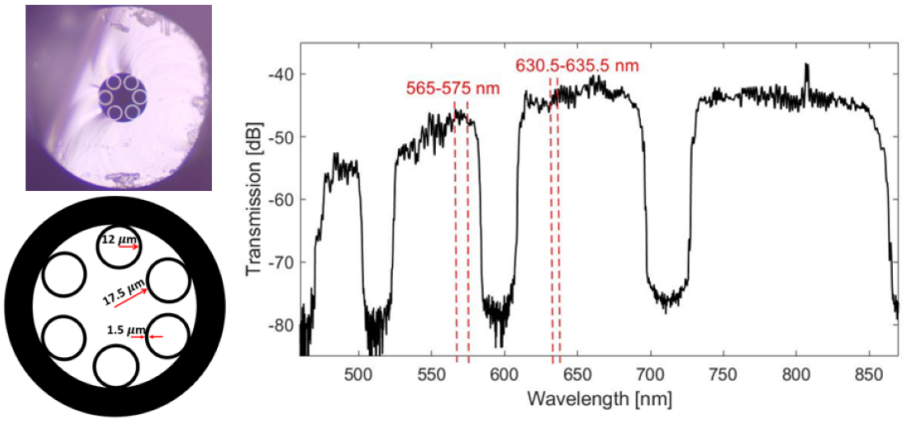

Figure 4.13: Microscopic image, schematics, and the transmission spectra of the TLF-6.

The light guidance in TLF-6 is based on inhibited coupling. Its transmission spectrum appears as an alternating sequence of high and low transmission bands as shown in Fig. 4.13. The positions of high and low transmission bands of the spectrum can

be estimated with the following equations respectively:

$$\lambda_{m+\frac{1}{2}} = \frac{2t}{m+\frac{1}{2}}\sqrt{{n_d}^2 - 1} \tag{4.8}$$

$$\lambda_m = \frac{2t}{m}\sqrt{{n_d}^2 - 1} \tag{4.9}$$

In both equations, m is an integer number and t is the thickness of holes [227]. The multi-step functionalization protocol for DNA detection described in [227] creates a bio-layer on the inner walls of the holes. The refractive index of the bio-layer is about 1.5 which is very close to the refractive index of silica. Therefore, the formed bio-layer can be considered as an extension of the hole's walls, so the increased thickness changes the position of bands $\lambda_{m+\frac{1}{2}}$ and λ_m. The previous experiments have shown that the bands can be shifted in response to the formed bio-layer by 2.48-14.08 nm [227].

4.3.2 Experimental setup

Figure 4.14 shows the old optical setup used for employing HC-PCFs as biosensors. A light emitted by a super-continuum white light source in the range of 450-2400 nm is coupled into the HC-PCF by an appropriate lens. Then, the light from the PCF passes through another lens to a CCM1–PBS252/M cage cube-mounted beam splitter working in the 620–1000 nm range. One of the beams of light is then directed into an AQ-6315A/-6315B optical spectrum analyzer which can measure the transmission spectrum in a 350–1750 nm range. Another beam is guided to a Zelux Camera working in a visible range (400-700 nm). All components of the setup are placed on the 3-axis micropositioning stages to achieve their precise small-step movements in 3 directions. The stages are used for the alignment of the system's components to the coupling of light into the PCF and later into the optical spectrum analyzer.

The spectrum analyzer and the camera are connected to a laptop for real-time recording of the spectrum and monitoring of the mode excited in the fiber. The camera records the modes over the whole visible range and then provides an average. It is important to excite the same mode, preferably fundamental, in each step of the

measurements in order to have consistency between the steps. The transmission spectrum is recorded after ensuring the excitation of FM by the camera in each step of the functionalization process.

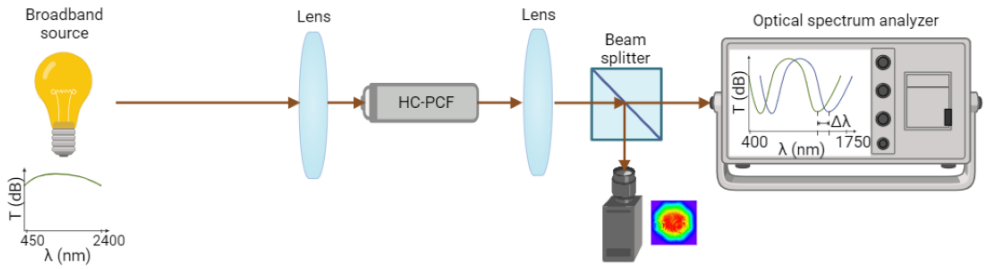

Figure 4.14: Schematics of the optical setup previously applied in the HC-PCFs experiments.

There are two main challenges faced while working on this setup:

- It is difficult and time-consuming to excite FM inside the PCFs. The light should enter the PCF perpendicular to its edge, but the micropositioning stages under the light source and lens do not give sufficient control of the incident angle of light.
- Using the averaged FM as a reference to achieve consistency between different measurements can be unreliable because the wavelengths at which that mode is achieved can vary from one measurement to another. As a result, the shift of the transmission spectrum may be a result of the divergence in measurements, rather than a response to the formed bio-layer.

Figure 4.15 demonstrates the schematics and photo of the new setup that has two main improvements. First of all, two mirrors placed at the 3-axis micropositioning stages are added in between the light source and the lens. The movement of the mirrors in three directions allows changing the angle at which the light enters the PCF. As a result, the FM's excitation is achieved faster and easier. Secondly, two band-pass

filters are placed between the beam splitter and the camera. They pass the light with the center wavelength at 570 nm and 633 nm and a range of 10 nm and 5 nm respectively. As a result, the camera averages the modes over a small range of wavelengths and at different places of the spectrum. By conducting three camera recordings, average (with no filter), at 570 nm and at 633 nm, the excitation of FM can be ensured with better accuracy. The band-pass filters have been selected so that the passed light is in the range of the wavelengths that correspond to the high transmission bands of TLF-6. According to Fig. 4.13, the 570±5 nm and 633±2.5 nm regions are in the second and third high transmission bands respectively.

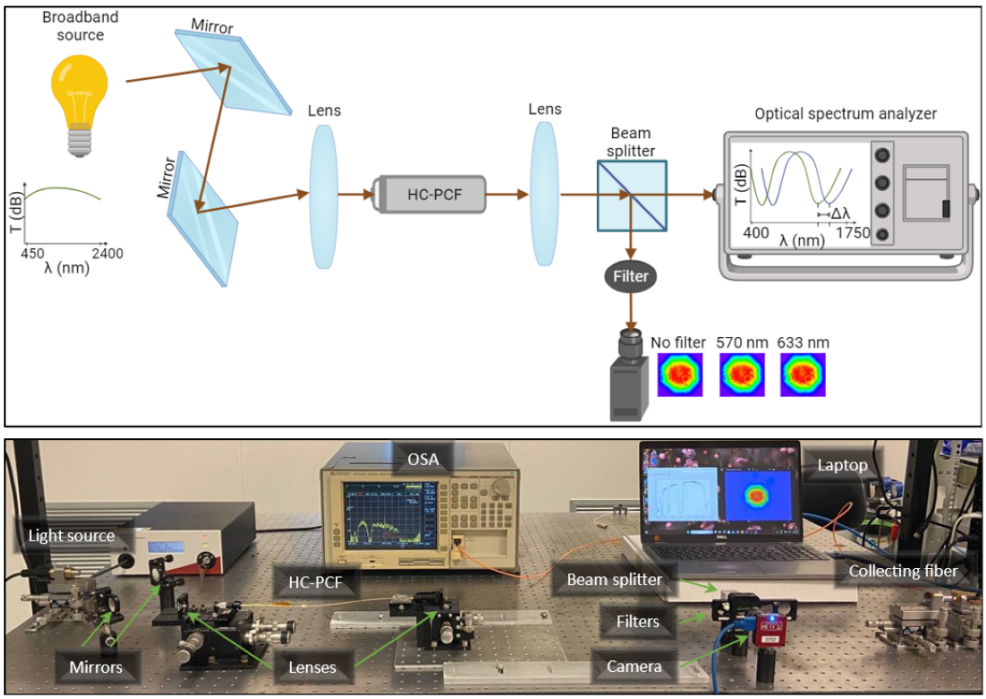

Figure 4.15: The schematics and photo of the optical setup with the addition of two mirrors and two band-pass filters.

In total, four sets of experiments have been conducted with the 40 cm long empty

TLF-6. The procedure of each experiment is as follows:

- Fiber preparation: the fiber was cleaved at both ends in order to ensure a cut perpendicular to the incident light. Two ends of the fiber were fixed at the two micropositioning stages as shown in Fig. 4.15.
- Mirrors and filter application: A holder that allows the incorporation of up to 4 filters was used to hold 2 filters and leave 2 empty spots used as a "no filter" case. The holder was first set to the "no filter" position. The mirrors were aligned until the FM was detected by the camera. Then, the mode was checked at 570 and 633 nm by setting the right filter. The mode obtained at one or both of the wavelengths was not necessarily FM, which supports the assumption that the average mode is not a reliable reference.
- Measurement of case 1: the mirrors were used to achieve FM at both wavelengths. This case is called consistent FM because the FM was excited without the filter (average), and at both checked wavelengths. All three camera recordings were saved and the transmission spectrum was recorded. Then, trial 2 was recorded by aligning the mirrors slightly to achieve different excitation but still preserve the FM at all checked wavelengths. This process was repeated again in order to achieve a total of three trials of the consistent FM case.
- Measurement of case 2: the mirrors were rotated so that the average mode was FM, but at least one filtered mode was not. This case is called inconsistent FM to point out the discrepancy of the mode distributed over the visible wavelength range and delusion of the FM measured without the filter. Three trials of measurement were recorded.
- Measurement of case 3: the mirrors are aligned so that the average mode was a higher-order mode, which resulted in the case called "not FM". Three trials of this case were also recorded.
- Next experiments: within each experiment, the fiber was fixed in order to check how the mirrors' position influenced the mode when all other conditions were

not changed. However, the functionalization process for DNA measurement requires cleavage of the fiber's ends after each injection step due to their damage or contamination. Therefore, it is important to check how the cleavage and change in the fiber's position may influence the transmission spectra shift. After the first experiment, the fiber's ends were cleaved and the fiber was fixed on the stages. A new experiment with 9 measurements (3 cases $\times$ 3 trials) was performed. Then, the fiber was cleaved again and the experiment was repeated twice more.

It should be noted that the range by which the mirrors can be rotated in 3 axes and still remain within case 1 is smaller compared to cases 2 and 3. It already indicates that the deviation between the trials in case 1 should be the smallest. However, the final conclusions can be made by discussing the results in the next section.

4.3.3 Results and Discussion

Camera recordings of all measurements with and without filters are shown in Fig.4.16. All measurements are grouped vertically according to 4 experiments and horizontally according to 3 cases (consistent FM, inconsistent FM, and not FM).

Two conclusions can be made from this figure. Firstly, several cases have been achieved within one experiment, so the mirrors indeed gave an opportunity to excite different modes without cleaving the fiber or changing its position. It not only saves time but also is important for the accuracy of the technique. Previously, the PCF was cleaved until the required mode was excited, so it could be cleaved several times before each measurement. This led to a significant reduction in the fiber's length at the end of the experiment. As a result, the length of the fiber starts to become another parameter that brings the variation in the measurements. After the application of mirrors, the cleavage can be conducted once before each measurement step, so the length will not change significantly.

Secondly, some differences between the average FM in cases 1 and 2 can be noticed: in the inconsistent FM cases, the average FM can be more prolongated (like in trials 2 and 3 of experiment 4) or have some sharp edges (like in trial 3 of experiment

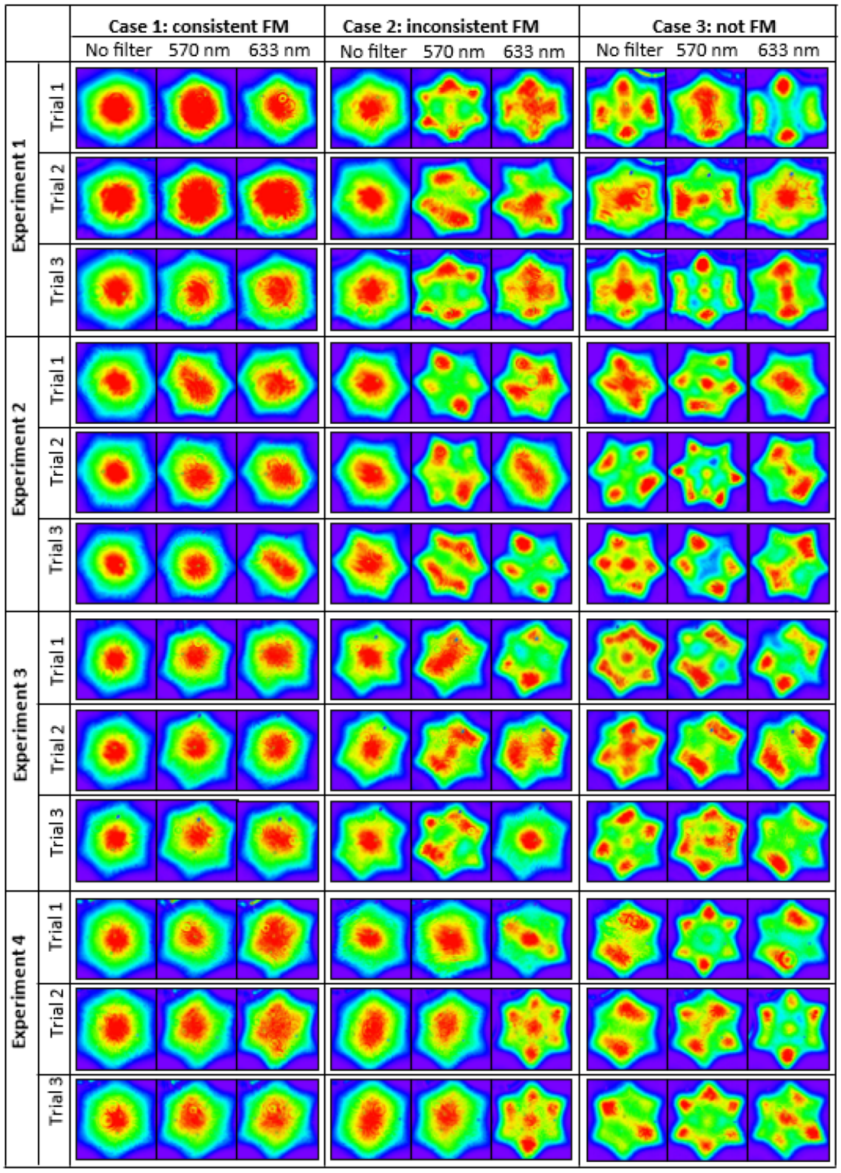

Figure 4.16: Modes recorded by the camera (with and without filters) during the experiments with the empty TLF-6.

2 and all trials in experiment 3). However, the differences in those patterns are not reliable signatures of inconsistent FM and are not present in all the measurements in case 2. Therefore, without checking the mode with different band-pass filters it is hard to distinguish between consistent and inconsistent FMs. In the future, it is planned to use more band-pass filters with different center wavelengths covering all high-transmission bands of TLF-6 in order to check the mode at other positions.

Therefore, the optical setup has significantly improved by the addition of mirrors and filters. The next step is to check how the difference in the excited mode may influence the transmission spectra.

Figures 4.17 (a-d) demonstrate the transmission spectra of all trials within experiments 1-4 respectively. The spectra are shown as green, yellow, and red to represent cases 1, 2, and 3 respectively. The shift of the spectra is compared in a region when a high transmission band is going into a low transmission band at transmission equal to -61 dB. The mean and standard deviations are also depicted by green, yellow, and red colors corresponding to each case. The general pattern in all 3 experiments is that the mean for case 3 when the average mode is not FM (red) is noticeably left-shifted with respect to the consistent FM case (green). The shift varies from 1.09 to 2.94 nm, which can be significant considering that the shift in response to the bio-layer is expected to be in the range of 2.48-14.08 nm. Therefore, preserving the same average excited mode in different measurements was important in the experiments presented in previous works.

The shift of the mean for the inconsistent FM case (yellow) with respect to the consistent FM scenario (green) is smaller. It varies from 0.09 to 1.23 nm which still can influence the accuracy of measurements. Moreover, in most cases, the deviation within the trials of the inconsistent FM case is larger than it is in the measurements with consistent FM. This shows that it is insufficient to check the average mode only and the filters should be used to improve reproducibility and decrease the errors in DNA measurements.

An interesting feature can also be noticed in the results of experiment 4. According to Fig. 4.16, in the inconsistent FM case, the mode recorded at 570 nm is FM in all trials of experiment 4. According to Fig. 4.17 (d), the mean is still shifted with respect

to the consistent FM case by about 0.17 to 1.07 nm and the deviation is larger than in the consistent FM case. Therefore, even if the average mode and the mode checked at one of the wavelengths are FM, there can still be a shift. So, the application of one band-pass filter is not sufficient.

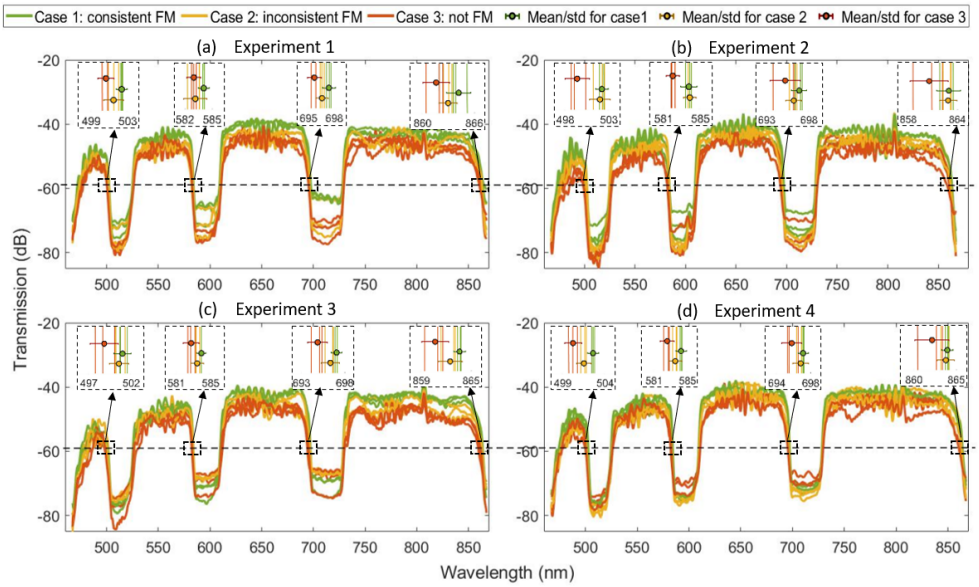

Figure 4.17: Transmission spectra recorded during each of the four experiments with the empty TLF-6.

Figure 4.18 demonstrates the transmission spectra from all experiments combined into one figure in order to evaluate the reproducibility of all experiments. As can be seen, the mean value for cases 3 and 2 has been left-shifted with respect to case 1 by 1.4-2.4 and 0.5-0.7 nm respectively. Since the values are within a similar range as the shifts in each individual experiment, it shows that the cleavage and small changes in the fiber's position do not contribute significantly to the transmission spectrum shift and the experiment-to-experiment reproducibility is good.

The standard deviation for case 1 varies from 0.75 to 1.24 nm, which is slightly

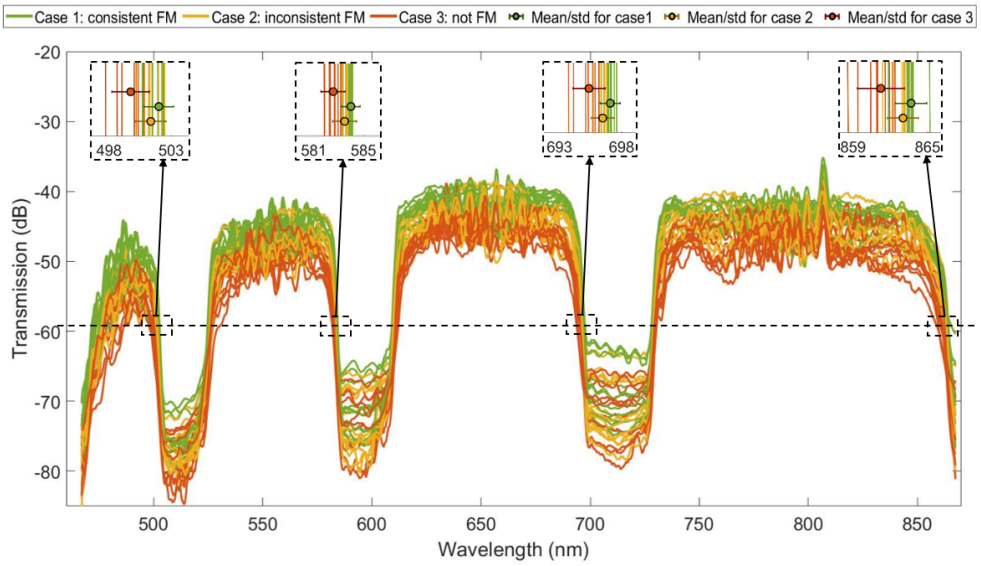

Figure 4.18: Transmission spectra recorded during all experiments with the empty TLF-6.

smaller than for case 2 (0.93-1.25 nm) and case 3 (0.97-1.88 nm). These deviations seem to be smaller for the second and the third bands probably because the wavelength ranges checked with the filters are located there. It can also explain the relatively large standard deviation within case 1 found for the first transmission band in experiment 1 (see Fig. 4.17 c) and for the last high transmission band in experiments 1 and 2 (see Fig. 4.17 a and b respectively). There is a possibility that some of the trials did not achieve the FM in the first or last bands, contributing to the increased deviation. Therefore, the application of the band-pass filters with the center wavelengths within each of the high transmission bands can be advantageous.

In general, reducing the deviation between the measurements is important considering that the transmission spectra shift due to the bio-layer formation is about 2.48-14.08 nm. The application of filters allows to reliably assign the whole detected shift to the changed bio-layer so the accuracy and sensitivity of the PCF-based biosensor

can be increased.

4.4 Conclusion

To conclude, this chapter has presented the PCFs used as an optofluidic device for the detection of nucleic acids by two different approaches: SERS measurement and transmission spectra shift-based measurement.

SERS measurement of miRNAs inside SuC-PCFs was achieved by anchoring NPs and immobilizing the thiolated capture DNAs. The optimal parameters for the experiments were selected by simulating the newly developed SuC-PCF model in COMSOL. According to the simulations, the PCF with $D_{core} = 3\mu m$ and a length of 8 cm has been selected for the measurement of $10^{-4}M$ of capture DNAs and miRNAs. SERS measurement of DNA and miRNA immobilized by anchoring method resulted in SERS spectra slightly less intense than that achieved during the measurements on the CaF_2 substrates conducted in the previous chapter. SERS measurement of DNA mixed with AgNPs-LM and injected into the PCF with already anchored NPs and DNA (to enhance detection abilities) has resulted in a better SERS signal. However, in this way, it is more challenging to use a capture-based protocol because DNAs are not fixed on the walls. The peak of adenine around 734 cm^{-1} is the only sufficiently intense peak in both types of measurement in the PCFs, so it is hard to discriminate different DNAs and the event of miRNA hybridization. Although the expected enhanced performance was not reached, there is room for improvement. As shown in Chapter 3, the method of DNA and miRNA immobilization on the substrate can significantly influence the results. The process of PCF functionalization can also be optimized. The type or size of NPs can be adjusted by conducting more simulations with the proposed model. Other parameters can be optimized by conducting more experiments, like the CD of NPs and the PCF's functionalization protocol (time of incubation, speed of injection). Moreover, the injection method for NP immobilization can also be simulated in the model and tested experimentally by comparing the detection in PCFs and in NPs colloidal solution.

The transmission spectra shift-based measurement of DNAs inside HC-PCFs is

also a promising research direction. Therefore, the optimization of the optical setup for this measurement has been presented in this chapter. The first improvement is achieved by the addition of two mirrors in between the light source and the lens that direct the light into the fiber. In the previous setup, the excited mode could only be changed by cleaving the fiber, so the excitation of FM required multiple cleavages in each step of the experiment and took time. The application of mirrors has allowed changing the incident angle of light and achieving many different modes without cleavage or changing the fiber's position (about 9 modes are shown within 1 trial). The FM can be excited faster and easier. The number of cleavages per measurement can be reduced preserving the length of the fiber during the several-step experiment and thus, reducing the influence of changed length on the results. Another improvement was the introduction of the two band-pass filters between the beam splitter and the camera. An application of the band-pass filters revealed that the mode recorded at particular wavelength regions can differ from the average one. The left-shifted mean value and increase of the standard deviation were observed when the excited FM was not consistent over the whole wavelength range. Therefore, the averaged FM should not be used as a reliable reference to obtain stable measurement conditions and instead, the mode should be checked at least at two other wavelength regions. Future work will be focused on the application of more band-pass filters in other high-transmission band regions to achieve further improvement in measurement reproducibility. Then, the optimized optical setup will be used for DNA measurements.

It should be noted that the step-to-step deviation in both types of measurement inside PCFs (SERS and transmission shift spectra-based) can be reduced by designing setups that do not require PCF's dismounting for each functionalization step. This can be considered as a future work.

Chapter 5

MiRNAs measurement with TERS probes

5.1 TERS working principle

Tip-enhanced Raman Spectroscopy (TERS) is an emerging technique that combines Raman spectroscopy with scanning probe microscopy (SPM) [234]. As shown in Fig. 5.1, the working principle of TERS is based on a sharp nm-sized SPM tip coated with plasmonic metals, like silver or gold. As silver oxidizes more quickly, gold is usually preferred for its higher long-term stability. When the last metal NP on the tip's apex is illuminated by the laser and brought in contact with the sample, it induces chemical and EM enhancements similar to those discussed for SERS in Chapter 1. Overall TERS enhancement factor can be calculated as follows [235]:

$$EF_{TERS} = \left(\frac{I_{nf} + I_{ff}}{I_{ff}} - 1 \right) \frac{V_{ff}}{V_{nf}} \tag{5.1}$$

In this equation, I_{nf} and I_{ff} are the near-field and far-field Raman peak's intensities measured when the tip is in and out of contact with the sample respectively. V_{ff} is a far-field focal volume that is calculated by multiplying a laser beam area by the height of the effective focus depth. V_{nf} is a near-field focal volume found from the

volume of a cone with the radius equal to the tip's radius of curvature (R_{tip}) and the height equal to the near-field separation [235].

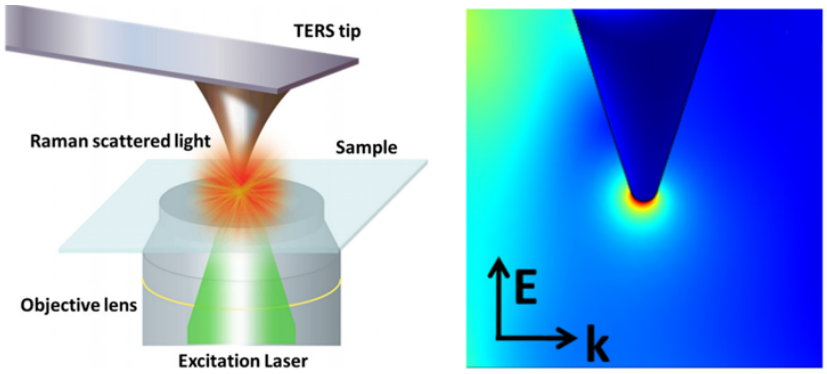

Figure 5.1: (a) Schematics illustrating the working principle of TERS: the metal-coated TERS tip is illuminated by the excitation laser and brought into contact with the sample, so Raman scattering is amplified by the chemical and EM enhancement. (b) COMSOL simulation of the TERS tip: the wave with electric field E and wave vector k is incident on the apex of the metal-coated tip causing the local EM field enhancement. Adapted from Kumar *et al.* [236].

The main advantage of TERS over SERS is its ability to provide accurate spatially resolved chemical analysis of the sample. As was mentioned, enhancement of the local EM field via the LSRP mechanism is heavily influenced by the size, shape, and roughness of the metal NPs. In SERS, different regions of the sample interact with different NPs located within a SERS substrate. Moreover, a laser has a broad spot size, so the SERS signal even in a single measurement arises from the contribution of several NPs [237]. Any non-uniformity of NPs introduces variations in the EM enhancement, so the intensity of the SERS signal can vary within the substrate. On the other hand, TERS measurement of different regions of the sample and even of various samples can be performed by the same NP on the apex of the single TERS tip. The enhancement factor is expected to be constant and spatially resolved measurement can be achieved.

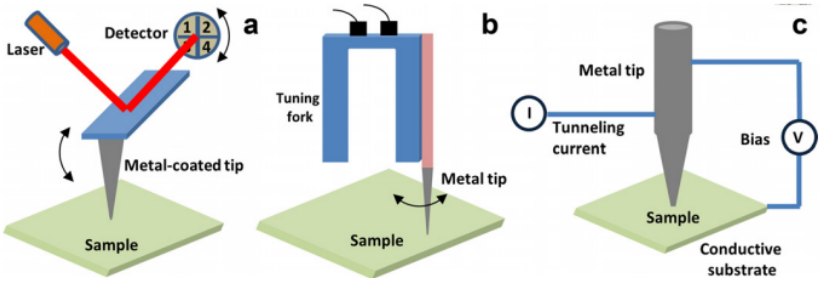

Figure 5.2: Feedback mechanisms used in TERS: contact/tapping AFM (a), shear force AFM (b), and STM (c). Adapted from Kumar *et al.* [236].

The control of the tip's position relative to the sample is achieved through one of the SPM techniques, such as contact/tapping atomic force microscopy (AFM), shear force AFM, or scanning tunneling microscope (STM) [236]. In the contact/tapping AFM, illustrated in Fig. 5.2 (a), the metal-coated tip is attached to a cantilever. In contact mode, a deflective force is applied on the cantilever, so that the tip has a repulsive interaction with the sample surface. In tapping mode, the tip is forced to oscillate with a certain amplitude. The deflective force in contact mode and the amplitude of oscillation in tapping mode are kept constant by the feedback, while the tip scans the surface. The feedback mechanism controls the tip's movement according to the change in the height of the sample surface. The light coming from a small diode laser is focused on top of the cantilever and detected by a photodetector which can detect any deviation caused by the tip's movement. This light is different from the light of the Raman instrument, which focuses on the tip apex. Thanks to the photodiode sensitivity and the feedback rapidity, AFM allows imaging surface topographies with a spatial resolution down to 20 nm [235, 236]. In the shear-force AFM, the tip is mounted on one of the prongs of the tuning fork that oscillates in the lateral direction as depicted in Fig. 5.2 (b). The oscillation is affected by the movement of the tip that tries to preserve the same shear force with the sample's surface. Change in the oscillations is used to reconstruct the sample's topography with a resolution of about 100 nm [236, 238]. According to Fig. 5.2 (c), the working principle of STM-TERS is based on a bias voltage applied between the metal tip and the sample placed on

the conductive substrate. An induced tunneling current is used as feedback to keep a constant tip-to-sample distance and reconstruct the surface topography with high resolution (0.5-1.7 nm) [236].

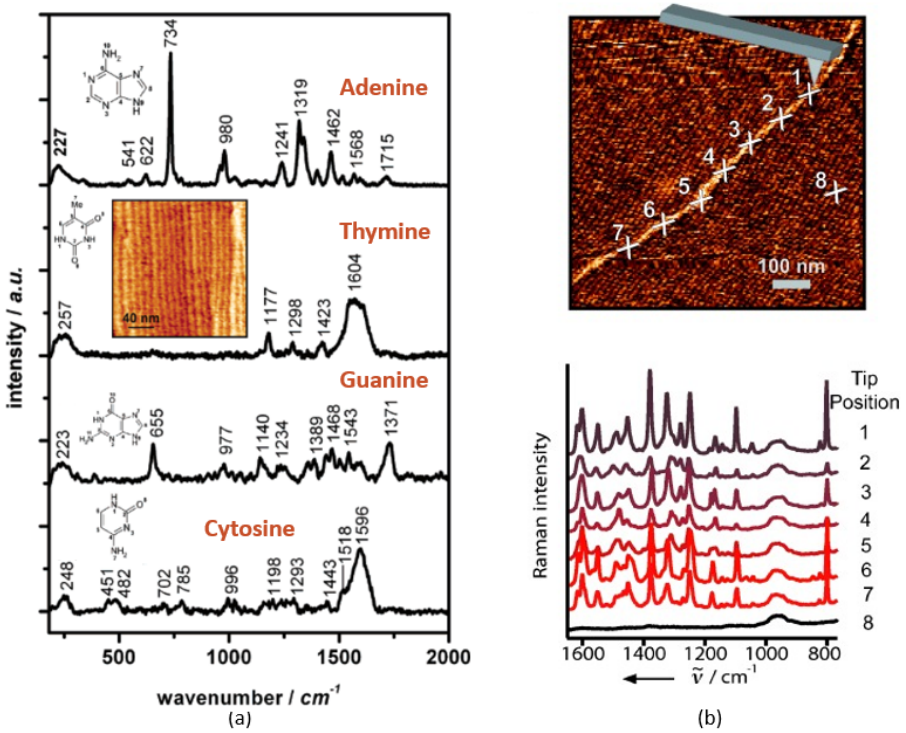

Figure 5.3: (a) TERS spectra of DNA bases (adenine, thymine, guanine, cytosine) at picomole concentration absorbed on Au substrate and measured with Au STM tip. The measurement was conducted by a 632.8 nm laser with 2 mW power. Adapted from Domke *et al.* [239]. Copyright 2007 American Chemical Society. (b) AFM image and TERS spectra of RNA strand. The measurement was performed by a 530.9 nm laser with 1 mW power. Adapted from Bailo *et al.* [240]. Copyright 2008, Wiley-VCH Verlag GmbH and Co. KGaA, Weinheim, Germany.

The concept of TERS was first proposed in 1985 by Wessel and experimentally validated in 2000, making TERS a relatively new technology. However, TERS has

already been studied for label-free measurement of various biological samples, including nucleic acids, peptides, proteins, pathogens, and others [236]. Thus, Domke *et al.* conducted STM-TERS measurements of four bases of DNA, namely adenine, thymine, guanine, and cytosine, at picomole concentration. The experiment was conducted by the 632.8 nm laser with 2 mW power. Figure 5.3 (a) illustrates that the obtained TERS spectra of bases are similar to the SERS spectra presented in Chapter 2. Bailo *et al.* presented AFM-TERS measurements of a single-stranded 20 nm-long RNA homopolymer of cytosine. According to Fig. 5.3 (b), TERS spectra are reproducible along the strand of RNA. The spectra consist of the peaks of cytosine, most prominent of which are around 792 cm^{-1}, 1248 cm^{-1}, 1303 cm^{-1}, 1373 cm^{-1}, and 1590 cm^{-1}. The peaks around 1248 cm^{-1} and 1373 cm^{-1} are very intense in the TERS spectrum of RNA, but almost negligible in the TERS (Fig. 5.3, a) and SERS (Fig. 2.4, b) spectrum of cytosine.

5.2 Experimental setup

The experimental setup used for AFM-TERS measurement has been developed by Horiba company and is shown in Fig. 5.4. The setup consists of the *LabRAM HR Evolution* Raman spectrometer (a) connected to the *OmegaScope* 1000 platform (b) that hosts an optical microscope and an SPM microscope (c). Au-coated AFM-TERS tip and Au-coated silicon substrate with a sample are placed inside the SPM microscope as depicted in Fig. 5.4 (d). The measurements of four bases of miRNA at $10^{-4}M - 10^{-3}M$ concentrations have been performed by dropping 2 μL of each sample on the substrate and drying it with the compressed air. Then, the substrate is placed on a movable stage inside the SPM microscope. AFM-TERS probe (Fig. 5.4, e) is placed under the substrate and a laser is focused on the apex of the tip to produce a hot spot as illustrated in Fig. 5.4 (f). In this setup, the tip is fixed and the substrate is moved relative to the tip by using the AFM feedback. The detailed description of the setup is presented by [235, 241].

The measurements have been conducted with the 633 nm laser. Firstly, a grating with 150 gr/mm has been used for measuring adenine, cytosine, uracil, and guanine

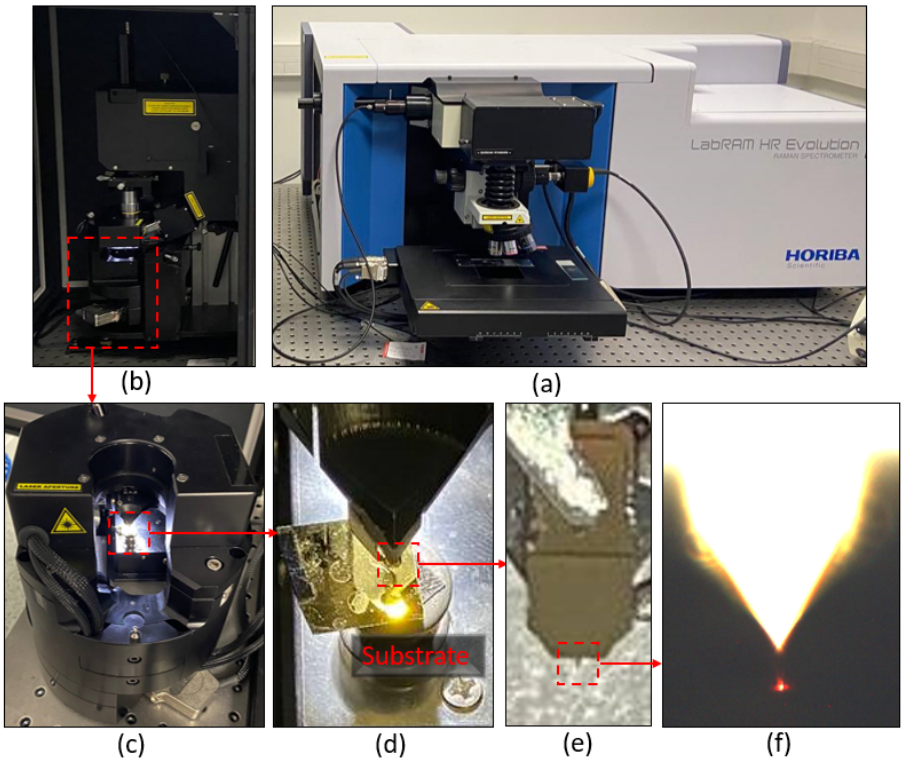

Figure 5.4: AFM-TERS setup in Horiba SAS company (Lille, France) consists of a *LabRAM HR Evolution* Raman spectrometer (a) connected to an *OmegaScope* 1000 platform (b) with a piezo-controlled objective and a *SmartSPM* microscope (c) [235]. Au-coated silicon substrate with a dried drop of sample (d) is fixed on a movable stage of the SPM microscope under the AFM-TERS probe (e). The laser is focused on the tip of the AFM-TERS probe (f) for TERS measurements.

at $10^{-4}M$. Guanine has been remeasured at a higher concentration because a good spectrum of guanine at $10^{-4}M$ has not been achieved. Since the range of interest is not broad, the grating has been changed to 600 gr/mm to get higher resolution in the subsequent measurements of guanine and miRNA at $10^{-3}M$. The laser power was adjusted to each sample during the measurement: adenine was measured with 0.124 mW; cytosine and guanine were measured with 0.397 mW; uracil and miRNA with

0.62 mW. TERS spectra of bases have been collected with 50 acquisitions and 0.45 s acquisition time, a TERS map of guanine was measured with 40 acquisitions and 0.45 s acquisition time, and miRNA was detected with 3 acquisitions and 10 s acquisition time.

5.3 AFM-TERS measurements of bases and miRNA

Figure 5.5 illustrates the AFM image and TERS spectrum of each of the bases of RNA, such as adenine (a), cytosine (b), guanine (c), and uracil (d). The AFM images reveal grain-like particles of about 100-500 nm in size present for all bases. TERS measurements were performed at the places marked by a red cross on each AFM image. TERS spectra of each base shown by red color in Fig. 5.5 contain the peaks that are shifted by several cm^{-1} with respect to the SERS peaks of the respective bases listed in Table 2.1. For example, the following TERS peaks correspond to the SERS peaks given in parentheses: 740 (734), 960 (961), 1334 (1331), and 1461 (1457) cm^{-1} for adenine; 795 (792) and 1041 (1037) cm^{-1} for cytosine; 660 (658), 962 (957), 1353 (1346), 1384 (1381), and 1461 (1464) cm^{-1} for guanine; 797 (796), 1051 (1045), and 1397 (1398) cm^{-1} for uracil. The far-field spectra of all bases (blue), recorded when the tip is out of contact with the samples, do not contain the observable peaks of the bases. Therefore, the peaks detected in the TERS spectra are indeed coming from the TERS enhancement.

Figure 5.6 illustrates the results of the AFM-TERS measurement of the let7i miRNA at $10^{-3}M$ concentration. The large-scale AFM image (a) reveals structures that may be clusters of miRNA strands. At a smaller scale (b), a 500 nm long strand, probably a strand of miRNA, can be observed. The far-field and TERS spectra were recorded on a spot of the strand marked by the red cross. Figure 5.6 (c) shows that the far-field spectrum (blue) does not contain any significant peaks, while the TERS spectrum (red) has multiple intense peaks. The peaks mostly correspond to the SERS/TERS peaks of miRNA bases shown in Fig. 2.4 and 5.5, but are shifted by several cm^{-1}. For example, the highest guanine peak around 660 cm^{-1} is combined with the adenine's peak around 626 cm^{-1} in the miRNA spectrum resulting

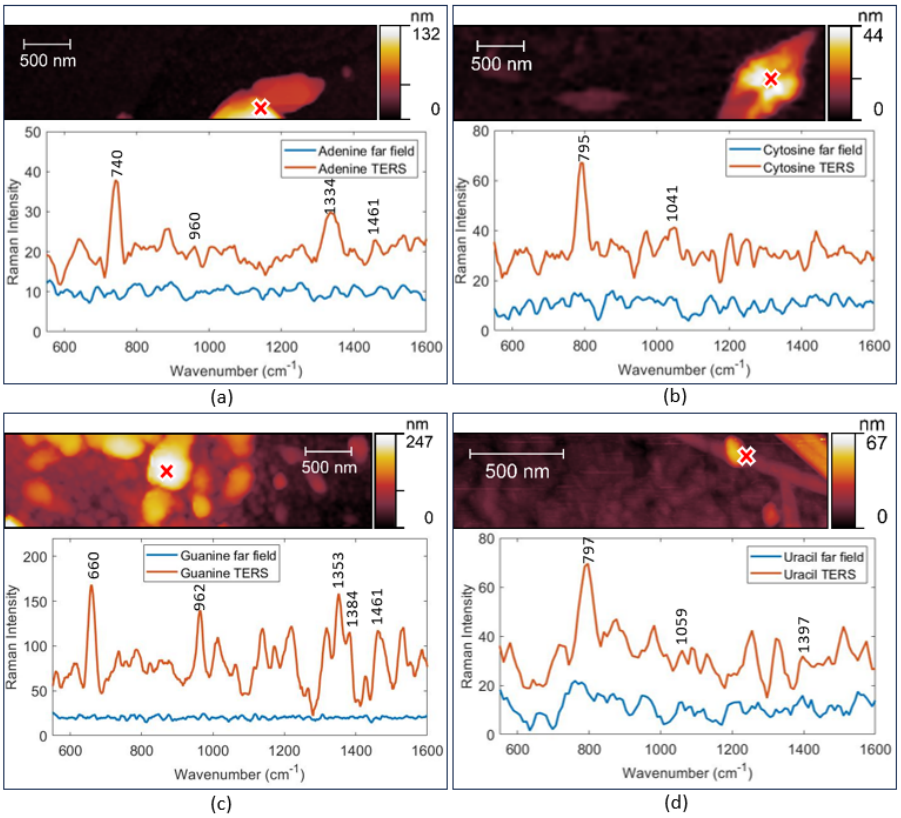

Figure 5.5: AFM images and TERS spectra of RNA bases: (a) $10^{-4}M$ adenine, (b) $10^{-4}M$ cytosine, (c) $10^{-3}M$ guanine, (d) $10^{-4}M$ uracil. A red cross shows the points where the TERS spectra were taken. The bases were measured by 633 nm laser, 0.45 s acquisition time, and 50 acquisitions. Power and grating have been adjusted to each base: adenine - 0.124 mW and 150 gr/mm; cytosine - 0.397 mW and 150 gr/mm; guanine - 0.397 mW and 600 gr/mm; uracil - 0.62 mW and 150 gr/mm.

in a single peak around 641 cm^{-1}. The most intense peaks of adenine (around 740 cm^{-1}), cytosine (around 795 cm^{-1}), and uracil (around 797 cm^{-1}) can be found in the miRNA spectrum at around 731 cm^{-1} and 801 cm^{-1}. Notably, those peaks are not the most intense in the miRNA spectrum and are dominated by other peaks (around

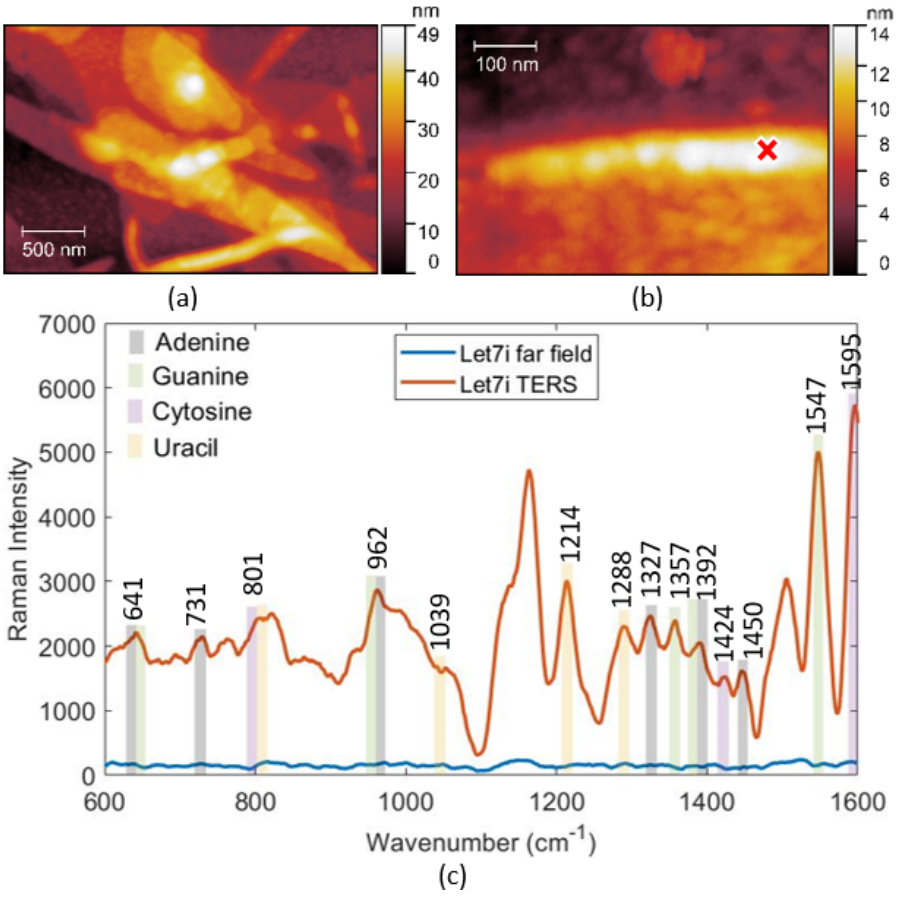

Figure 5.6: AFM images (a, b) and TERS spectra (c) of let7i at $10^{-3}M$ concentration. A red cross shows the points where the TERS spectra were taken.

1214 cm^{-1}, 1547 cm^{-1}, 1595 cm^{-1}). This is in agreement with the results presented by Bailo *et al.*, where the spectrum of RNA shown in Fig. 5.3 (b) exhibits more intense peaks in the 1200-1500 cm^{-1} region compared to the spectrum of the cytosine base shown in Fig.5.3 (a).

The ability of TERS to measure a particular point of interest selected on the AFM map is one of its advantages over SERS. Another benefit of this technology,

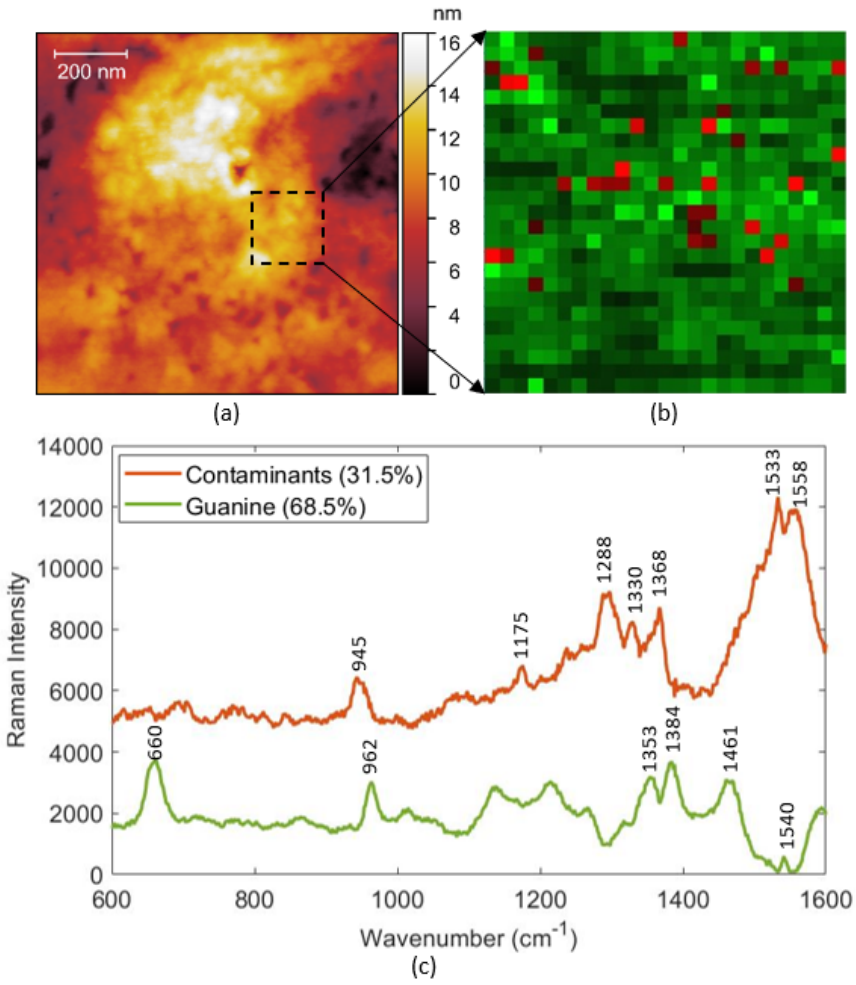

Figure 5.7: AFM-TERS measurement of guanine at $10^{-3}M$ concentration: (a) AFM map, (b) TERS map groping the regions with similar spectra (red, green, black), (c) Average TERS spectra of the signals collected at red (contaminants) and green (guanine) regions from TERS map.

such as spatially resolved chemical measurement was exploited for the acquisition of an AFM-TERS map of the guanine sample at $10^{-3}M$ concentration. The AFM

image was recorded over the 1×1 μm^2 region given in Fig. 5.7 (a), consists of dark regions with the lowest height and bright areas representing up to 16 nm high protuberances which are probably clusters of guanine molecules. The TERS map consisting of 25×25 TERS measurements have been recorded over a 200×200 nm^2 region of the guanine sample marked by a black square on the AFM image. The analysis of the hyperspectral TERS map has shown the variation of spectra from one pixel to another. Although only guanine was expected to be on the sample, some contaminants (probably other bases) might have polluted it during the phase of preparation and rinsing. Multivariate Curve Resolution (MCR) with two principal components has been applied for treating the hyperspectral TERS map and resulted in two loadings accounting together for 90.9% of the spectral variance. Figure 5.7 (c) shows that the first loading corresponds to the guanine spectrum (green), while the other indeed contains signatures of contaminants. Figure 5.7 (b) shows the MCR-treated TERS map, in which the green and red regions correspond to the zones with the predominance of the guanine and contaminants loading, respectively. In darker zones on the TERS map, both signals are weaker, probably because of the non-uniform distribution of the sample. Thus, TERS measurement can be useful to conduct chemical analysis over the area of the sample and discriminate which types of molecules are present in different regions.

5.4 Conclusion

In conclusion, AFM-TERS measurements presented in this chapter have shown the ability of TERS to provide localized and spatially resolved chemical information about the sample. The measurements have been conducted with highly concentrated bases and miRNAs, but good spectra were achieved with a small power of 0.124-0.63 mW. In comparison, the power used by Domke *et al.* for the TERS measurement of miRNAs is 2 mW, and the SERS measurement of miRNAs presented in Chapter 1 was performed with 80 mW power (with another laser and in liquid). Therefore, TERS has a good potential but more experiments with lower concentrated miRNAs and more resolved maps should be conducted.

Conclusion

This thesis aimed to study different methods of the detection of genomic biomarkers of cancer for liquid biopsy application as a potential non-invasive population screening method. Chapter 1 discussed three types of alterations in nucleic acids that may serve as cancer genomic biomarkers, including deregulation of miRNAs, point mutations in DNAs, and altered DNA methylation levels. This chapter also describes the working principle of SERS and reviews the biological protocols for target-specific sensing of the mentioned genomic biomarkers. The protocols were grouped into 5 categories and arranged according to the complexity of their design. Performance evaluation of the protocols was conducted based on two parameters, such as detection abilities and applicability in body fluids. The assessment has shown that the labeled on-to-two-step capture and displacement protocols with relatively simple assays can achieve optimal performance for liquid biopsy applications. Some label-free methods also have good potential if more advanced and sensitive SERS sensors are developed. The findings of this chapter have been summarized in the review paper.

After that, different types of SERS substrates were developed and tested, starting from Au-Ag NPs grown on the glass substrate, colloidal solutions of Au and AgNPs synthesized by different methods, and AgNPs dropped on the CaF_2 substrates. The work with those substrates has been conducted during the secondments at different Universities, including Politecnico di Torino, Leibniz-IPHT, and Tyndall National Institute. The results are presented in Chapters 2-3. The measurement of RNA bases has shown that out of all substrates the best LOD has been achieved by AgNPs-LM colloidal solution produced by the Lee-Meisel approach. Two miRNAs, let7a

and let7i, were successfully measured down to 10^{-8} M. However, their physiological concentration in body fluids is about $10^{-14} - 10^{-12}$ M and the detection was not target-specific. Therefore, AgNPs-LM were dropped on the CaF_2 substrate and the label-free capture-based protocol was implemented. Two capture DNAs, complementary to each miRNA, were immobilized on the substrate by dropping a sample or a long incubation of the substrate inside the sample. The second approach was more effective and resulted in the detection of capture DNAs and target miRNAs at 10^{-6} M. The event of miRNA hybridization to capture was detected, but the discrimination of the 3-nucleotide mismatched miRNA was found to be challenging due to partial hybridization.

The next research topic studied in this thesis was the SERS measurement of nucleic acids in PCFs presented in Chapter 4. The expected advantage of using PCF was the longer interaction of light with NPs and analyte, promising increased sensitivity and reproducibility. The special COMSOL model to simulate SuC-PCFs SERS response was developed and tested. The results of the simulation of this model were validated by SERS measurement of adenine with sizes of PCFs. The optimal PCF with $D_{core} = 3\ \mu m$ and a length of 8 cm was used for the measurement of capture DNA and target miRNA at 10^{-4} M. The prominent peak of adenine around 734 cm^{-1} was detected in the spectra of both DNA and miRNA capture by DNA, but due to the low intensity of other peaks, it was hard to distinguish between them. The spectra were compared with the spectra of the same DNA and miRNA measured at the same concentration on the CaF_2 substrate after removing the respective reference spectra of water. According to this evaluation, the performance of PCFs at the current stage of development is slightly worse than the one of substrates. However, this type of measurement involves many different parameters that should be carefully optimized (size and types of NPs, process of functionalization, and others). The developed COMSOl model and future experiments can be used to improve the detection abilities of this technique.

As can be seen, the main detection technique that has been explored in this thesis is SERS. Other two methods, transmission spectra shift-based technique and TERS, have been studied to complement the SERS-based experiments. Thus, the first one

allowed a better understanding of the working principle of PCFs and their functionalization process. This knowledge was useful in planning the working process of SERS-based measurement inside PCFs. The transmission spectra shift-based detection can be applied for the measurement of DNA at 5 μm concentration inside HC-PCF. In this thesis, two methods of the optimization of the optical setup for the measurement were presented: an addition of mirrors for better control of light coming into PCF and an application of the band-pass filters for a more accurate monitoring of the excited mode. The measurements were conducted at the University of Parma and the results are presented in Chapter 4.

The second technique discussed in Chapter 5 is TERS, which is the combination of Raman spectroscopy and SPM, used to provide spatially resolved chemical measurements. The measurement of RNA bases has been achieved with a much lower power (less than 1 mW) than the SERS measurement in colloidal solution (80 mW), but the detection limit is about 10^{-4} M. The AFM-TERS map of the guanine base was recorded to show the ability for spatially resolved chemical measurement that is hard to achieve with SERS due to the non-uniformity of NPs on a single substrate. TERS measurement of let7i at 10^{-3} M resulted in a quite intense signal with peaks similar to the SERS peaks. The measurements were performed in Horiba SAS company to gain more knowledge of the principles of Raman signal amplifications. The technique is not widely explored for the measurement of nucleic acids and the results presented in this thesis do not show sufficient LODs. However, AFM-TERS is highly dependent on the condition of the tip, so due to the potential of localized and spatially resolved analysis, this technique should be studied more.

In conclusion, SERS and TERS measurements of nucleic acids, especially miRNAs, have promising potential for the detection of genomic biomarkers in body fluids. SERS-based detection on the substrates is the most studied and developed technique that has already achieved promising applicability and LOD with relatively simple protocols. The main challenge to be addressed by the researchers is to design reproducible and sensitive SERS sensors. The application of PCFs could help to improve the sensitivity and reproducibility but requires a careful design of functionalization protocol. The application of TERS is also a relatively new approach that

can bring advantage of the spatially resolved measurement but needs to be further studied.

List of publications

The results of the work achieved during this PhD are reflected in the following Journal publications:

1) A. Issatayeva, C. Fornaini, M. Masino, A. Cucinotta. Potential role of Er:YAG laser and fluoride in the dental enamel remineralization: a Raman spectroscopy preliminary ex vivo study. *Laser Therapy Journal*, 29: 87-93, 2022.

2) A. Issatayeva, E. Farnesi, D. Cialla-May, M. Schmitt, F. M. A. Rizzi, D. Milanese, S. Selleri, A. Cucinotta. SERS-based methods for the detection of genomic biomarkers of cancer. *Talanta Journal*, 267: 1-17, 2023.

The results have been also presented at the following conferences and events:

1) A. Issatayeva, A. Cucinotta, D. Milanese, T. Poli, F.M.A. Rizzi, C. Sciancalepore. Photonics for Healthcare: multiscale cancer diagnosis and therapy (PHAST). *2021 Workshop on Engineering and Medicine*, September 2021, Parma, Italy [online].

2) A. Issatayeva, A. Cucinotta, D. Milanese, F.M.A. Rizzi, C. Sciancalepore. Review of Raman Spectroscopy-based methods for cancer detection via genomic biomarkers. *2021 European Biosensor Symposium: Raman-Based Biosensors*, September 2021, Digital Seminar Series [online].

3) A. Issatayeva, C. Fornaini, M. Masino, D. Milanese, A. Cucinotta. A Raman spectroscopy ex vivo study of the potential role of Er:YAG laser and fluoride in the dental enamel remineralization. *2022 Italian Conference on Optics and Photonics (ICOP) conference*, July 2022, Trento, Italy.

4) A. Issatayeva, C. Sciancalepore, D. Milanese, A. Cucinotta. Application of

Surface-Enhanced Raman Spectroscopy for the detection of miRNA-based cancer biomarkers. *2022 Italian Conference on Optics and Photonics (ICOP) conference*, July 2022, Trento, Italy.

5) A. Issatayeva, C. Sciancalepore, D. Milanese, M. Giardino, D. Janner, A. Cucinotta. Integrated liquid biopsy for cancer diagnosis via genomic biomarkers detection. *2021 Biophotonics Summer School*, July 2022, Island of Ven, Sweden.

6) A. Issatayeva, C. Sciancalepore, D. Milanese, A. Cucinotta. Overview of the SERS-based methods for the measurement of the miRNAs' expression level in body liquids. *2022 Riunione Nazionale di Elettromagnetismo (RiNEM) conference*, September 2022, Catania, Italy.

7) F. Khozeymeh, A. Issatayeva, E. Farnesi, D.Cialla-May, M. Schmitt, F. M. A. Rizzi, A. Cucinotta. SERS-based detection of the miRNAs as a potential tool for early-stage cancer diagnosis. *2023 D-Photon conference*, July 2023, Bari, Italy.

8) A. Issatayeva, E. Farnesi, D. Cialla-May, M. Schmitt, S. Maryam, K.W. Kho, S. Andersson-Engels, A. Cucinotta. Application of SERS for the detection of miRNAs as a tool for cancer diagnosis. *2023 Workshop del Gruppo Interdivisionale Sensori*, December 2023, Rome, Italy "

Bibliography

[1] H. Sung, J. Ferlay, R.L. Siegel, M. Laversanne, I. Soerjomataram, A. Jemal, and F. Bray. Global Cancer Statistics 2020: GLOBOCAN Estimates of Incidence and Mortality Worldwide for 36 Cancers in 185 Countries. *Cancer Journal for Clinicians*, 71:209—249, 2021.

[2] J. Marrugo-Ramirez, M. Mir, and J. Samitier. Blood-Based Cancer Biomarkers in Liquid Biopsy: A Promising Non-Invasive Alternative to Tissue Biopsy. *International Journal of Molecular Sciences*, 19:1—21, 2018.

[3] V.V. Levenson. Biomarkers for early detection of breast cancer: What, when, and where? *Biochimica et Biophysica Acta*, 1770:847—856, 2007.

[4] I. Avital, R.C. Langan, S.R. Steele T.A. Summers, S.A. Waldman, V. Backman, J. Yee, A. Nissan, P. Young, C. Womeldorph, P. Mancusco, R. Mueller, K. Noto, W. Grundfest, Anton J. Bilchik, M. Protic, M. Daumer, J. Eberhardt, Y.G. Man, B. Brücher, and A. Stojadinovic. Evidence-Based Guidelines for Precision Risk Stratification-Based Screening (PRSBS) for Colorectal Cancer: Lessons Learned from the US Armed Forces: Consensus and Future Directions. *Journal of Cancer*, 4:172—192, 2013.

[5] S. Abalde-Cela, L. Wu, A. Teixeira, K. Oliveira, and L. Diéguez. Multiplexing Liquid Biopsy with Surface-Enhanced Raman Scattering Spectroscopy. *Advanced Optical Materials*, 9:1—21, 2021.

[6] B. Sadikovic, K. Al-Romaih, J.A. Squire, and M. Zielenska. Cause and Con-

sequences of Genetic and Epigenetic Alterations in Human Cancer. *Current Genomics*, 9:394—408, 2008.

[7] G. Novelli, C. Ciccacci, P. Borgiani, M. Amati, and E. Abadie. Genetic tests and genomic biomarkers: regulation, qualification and validation. *Clinical cases in mineral and bone metabolism*, 5:149–154, 2008.

[8] X. Zhang, S. Shi, B. Zhang, Q. Ni, X. Yu, and J. Xu. Circulating biomarkers for early diagnosis of pancreatic cancer: facts and hopes. *American Journal of Cancer Research*, 8:332—353, 2018.

[9] C.E. Condrat, D.C. Thompson, M.G. Barbu, O.L. Bugnar, A. Boboc, D. Cretoiu, N. Suciu, S.M. Cretoiu, and S.C. Voinea. miRNAs as Biomarkers in Disease: Latest Findings Regarding Their Role in Diagnosis and Prognosis. *MDPI cells*, 9:1—32, 2020.

[10] Y. Chu, Y. Gao, W. Tang, L. Qiang, Y. Han, J. Gao, Y. Zhang, H. Liu, and L. Han. Attomolar-Level Ultrasensitive and Multiplex microRNA Detection Enabled by a Nanomaterial Locally Assembled Microfluidic Biochip for Cancer Diagnosis. *Analytical chemistry*, 93:5129–5136, 2021.

[11] Y. Wang, S.L. Kong, and X.D. Su. A centrifugation-assisted visual detection of SNP in circulating tumor DNA using gold nanoparticles coupled with isothermal amplification. *RSC Advances*, 10:1476—1483, 2020.

[12] J.H. Choi S.S. Kim, J.W. Eun, H.G. Woo, H.J. Cho, H.R. Ahn, C.W. Suh, G.O. Baek, S.W. Cho, and J.Y. Cheong. MLH1 single-nucleotide variant in circulating tumor DNA predicts overall survival of patients with hepatocellular carcinoma. *Scientific reports*, 10:17862—17870, 2020.

[13] A.A. Hussein, T. Forouzanfar, E. Bloemena, J. Visscher, R.H. Brakenhoff, C.R. Leemans, and M.N. Helder. A review of the most promising biomarkers for early diagnosis and prognosis prediction of tongue squamous cell carcinoma". *British Journal of Cancer*, 119:724—736, 2018.

[14] A.S. Alzahrani, A.K. Murugan, E. Qasem, M. Alswailem, H. Al-Hindi, and Y. Shi. Single Point Mutations in Pediatric Differentiated Thyroid Cancer. *Thyroid*, 27:189—198, 2017.

[15] R. Daum, E.M. Brauchle, D.A.C. Berrio, T.P. Jurkowski, and K. Schenke-Layland. Non-invasive detection of DNA methylation states in carcinoma and pluripotent stem cells using Raman microspectroscopy and imaging. *Scientific Reports*, 9:1—13, 2019.

[16] J. Ye, M. Xu, X. Tian, S. Cai, and S. Zeng. Research advances in the detection of miRNA. *Journal of Pharmaceutical Analysis*, 9:217–226, 2019.

[17] J. Plou, P.S. Valera, I. Garcia, C.D.L. de Albuquerque, A. Carracedo, and L.M. Liz-Marzan. Prospects of Surface-Enhanced Raman Spectroscopy for biomarker monitoring toward precision medicine. *ACS Photonics*, 9:333–350, 2022.

[18] J. Langer, D.J. de Aberasturi, J. Aizpurua, R.A. Alvarez-Puebla, B. Auguie, J.J. Baumberg, G.C. Bazan, S.E.J. Bell, A. Boisen, A.G. Brolo, J. Choo, D. Cialla-May, V. Deckert, L. Fabris, K. Faulds, F.J.G. de Abajo, R. Goodacre, D. Graham, A.J. Haes, C.L. Haynes, C. Huck, T. Iton, M. Kall, J. Kneipp, N.A. Kotov, H. Kuang, E.C. Le Ru, H.K. Lee, J.F. Li, X.Y. Ling, S.A. Maier, T. Mayerhofer, M. Moskovits, K. Murakoshi, J.M. Nam, S. Nie, Y. Ozaki, I. Pastoriza-Santos, J. Perez-Juste, J. Popp, A. Pucci, S. Reich, B. Ren, G.C. Schatz, T. Shegai, S. Schlucker, L.L. Tay, K.G. Thomas, Z.Q. Tian, R.P. Van Duyne, T. Vo-Dinh, Y. Wang, K.A. Willets, C. Xu, H. Xu, Y. Xu, Y.S. Yamamoto, B. Zhao, and L.M. Liz-Marzan. Present and future of surface-enhanced Raman Scattering. *ACS Nano*, 14:28—117, 2020.

[19] M. Gaidi, K. Daoudi, A. Tlili, S. Columbus, J. Leblanc-Lavoie, K. Ramanchandran, B. Suleiman, A.N. Alhazaa, and M.A. El Khakani. Fast, highly sensitive and label free detection of small genetic sequence difference of DNA using novel Surface-Enhanced Raman Spectroscopy nanostructured sensor. *Sensing and Bio-Sensing Research*, 32:1—10, 2021.

[20] G.W. Auner, S.K. Koya, C. Huang, B. Broadbent, M. Trexler, Z. Auner, A. Elias, K.C. Mehne, and M.A. Brusatori. Applications of Raman spectroscopy in cancer diagnosis. *Cancer and Metastasis Reviews*, 37:691—717, 2018.

[21] C.L. Haynes, A.D. McFarland, and R.P. Van Duyne. New substrates and single-molecule detection are just two of the advances that are fueling interest in SERS. *Analytical Chemistry*, pages 338—346, 2005.

[22] M. Jahn, S. Patze, I.J. Hidi, R. Knipper, A.I. Radu, A. Muhlig, S. Yuksel, V. Peksa, K. Weber, T. Mayerhofer, D. Cialla-May, and J. Popp. Plasmonic nanostructures for surface enhanced spectroscopic methods. *Analyst*, 141:756–793, 2012.

[23] J. Wang, K.M. Koo, Y. Wang, and M. Trau. Engineering State-of-the-Art Plasmonic Nanomaterials for SERS-Based Clinical Liquid Biopsy Applications. *Advance Science*, 6:1—35, 2019.

[24] A. Issatayeva, E. Farnesi, D. Cialla-May, M. Schmitt, F.M.A. Rizzi, D. Milanese, S. Selleri, and A. Cucinotta. SERS-based methods for the detection of genomic biomarkers of cancer. *Talanta*, 267:1—57, 2023.

[25] Y. Han, L. Qiang, Y. Gao, J. Gao, Q. He, H. Liu, L. Han, and Y. Zhang. Large-area surface-enhanced Raman spectroscopy substrate by hybrid porous GaN with Au/Ag for breast cancer miRNA detection. *Applied surface science*, 541:148456–148465, 2021.

[26] C.H. Lawrie, S. Gal, H.M. Dunlop, B. Pushkaran, A.P. Liggins, K. Pulford, A.H. Banham, F. Pezzella, J. Boultwood, J.S. Wainscoat, C.S.R. Hatton, and A.L. Harris. Detection of elevated levels of tumour-associated microRNAs in serum of patients with diffuse large B-cell lymphoma. *Britich Journal of haematology*, 141:672—675, 2008.

[27] L.J. Galvão-Lima, A.H.F. Morais, R.A.M. Valentim, and E.J.S.S. Barreto.

miRNAs as biomarkers for early cancer detection and their application in the development of new diagnostic tools. *Biomedical Engineering*, 20:1–20, 2021.

[28] K. Sundarbose, R.V. Kartha, and S. Subramanian. MicroRNAs as Biomarkers in Cancer. *Diagnostics*, 3:84—104, 2013.

[29] D.C.C. Poo, S. Cai, and J.T.L. Mah. UASIS: Universal Automatic SNP Identification System. *BMC Genomics*, 12:1–10, 2011.

[30] N. Deng, H. Zhou, H. Fan, and Y. Yuan. Single nucleotide polymorphisms and cancer susceptibility. *Oncotarget*, 8:110635–110649, 2017.

[31] T. Van den Broeck, S. Joniau, L. Clinckemalie, C. Helsen, S. Prekovic, L. Spans, L. Tosco, H. Van Poppel, and F. Claessens. The role of single nucleotide polymorphisms in predicting prostate cancer and therapeutic decision making. *BioMed Research International*, 2014:1–17, 2014.

[32] R.J. Maclnnis, A.C. Antoniou, R.A. Eeles, G. Severi, A.A. Al Olama, L. McGuffog, Z. Kote-Jarai, M. Guy, L.T. O'Bried, A.L. Hall, R.A. Wilkinson, E. Sawyer, A.T. Ardern-Jones, D.P. Dearnaley, A. Horwich, V.S. Khoo, C.C. Parker, R.A. Huddart, N. Van As, M.A. McCredie, D.R. English, G.G. Giles, J.L. Hopper, and D.F. Easton. A risk prediction algorithm based on family history and common genetic variants: application to prostate cancer with potential clinical impact. *Genetic Epidemiology*, 35:549–556, 2011.

[33] M.E. Penney, P.S. Parfrey, S. Savas, and Y.E. Yilmaz. Associations of single nucleotide polymorphisms with mucinous colorectal cancer: genome-wide common variant and gene-based rare variant analyses. *Biomarker Research*, 6:1–10, 2018.

[34] C. Garrigos, M. Espinosa, A. Salinas, I. Osman, R. Medina, M. Taron, S. Molina-Pinelo, and I. Duran. Single nucleotide polymorphisms as prognostic and predictive biomarkers in renal cell carcinoma. *Oncotarget*, 8:106551–106564, 2017.

[35] T. Mikeska and J.M. Craig. DNA methylation biomarkers: cancer and beyond. *Genes*, 5:821–864, 2014.

[36] T. Mikeska, C. Bock, H. Do, and A. Dobrovic. DNA methylation biomarkers in cancer: progress towards clinical implementation. *Expert Review of Molecular Diagnostics*, 12:473–487, 2012.

[37] H. Suzuki, M. Toyota, H. Sato, T. Sonoda, F. Sakauchi, and M. Mori. Roles and causes of abnormal DNA methylation in gastrointestinal cancers. *Asian Pacific Journal of Cancer Prevention*, 7:177–185, 2006.

[38] B.P. de Almeida, J.D. Apolonio, A. Binnie, and P. Castelo-Branco. Roadmap of DNA methylation in breast cancer identifies novel prognostic biomarkers. *BMC Cancer*, 19:1–12, 2019.

[39] C. Kneip, B. Schmidt, A. Seegebarth, S. Weickmann, M. Fleischhacker, V. Liebenberg, J.K. Field, and D. Dietrich. SHOX2 DNA Methylation Is a Biomarker for the Diagnosis of Lung Cancer in Plasma. *Journal of Thoracic Oncology*, 6:1632–1638, 2011.

[40] C. Li, Y. Zheng, K. Pu, D. Zhao, Y. Wang, Q. Guan, and Y. Zhou. A four-DNA methylation signature as a novel prognostic biomarker for survival of patients with gastric cancer. *Cancer Cell International*, 20:1–10, 2020.

[41] C. Leygo, M. Williams, H.C. Jin, M.W.Y. Chan, W.K. Chu, M. Grush, and Y.Y. Cheng. DNA methylation as a noninvasive epigenetic biomarker for the detection of cancer. *Hindawi*, 2017:1–13, 2017.

[42] S.O. Jensen, N. Ogaard, M.W. Orntoft, M.H. Rasmussen, J.B. Bramsen, H. Kristensen, P. Mouritzen, M.R. Madsen, A.H. Madsen, K.G. Sunesen, L.H. Iversen, S. Laurberg, I.J. Christensen, H.J. Nielsen, and C.L. Andersen. Novel DNA methylation biomarkers show high sensitivity and specificity for blood-based detection of colorectal cancer - a clinical biomarker discovery and validation study. *Clinical Epigenetics*, 11:1–14, 2019.

[43] W.J. Locke, D. Guanzon, C. Ma, Y.J. Liew, K.R. Duesing, K.Y.C. Fung, and J.P. Ross. DNA Methylation Cancer Biomarkers: Translation to the Clinic". *Frontiers in Genetics*, 10:1—22, 2019.

[44] S.A. Deepak, K.R. Kottapalli, R. Rakwal, G. Oros, K.S. Rangappa, H. Iwahashi, Y. Masuo, and G.K. Agrawal. Real-Time PCR: Revolutionizing Detection and Expression Analysis of Genes. *Current Genomics*, 8:234–251, 2007.

[45] C. Delaney, S.K. Garg, and R. Yung. Analysis of DNA methylation by pyrosequencing. *Methods in Molecular Biology*, 1343:249–264, 2015.

[46] F. Beffara. SERS biosensors based on special optical fibers for clinical diagnosis. *Ph.D. thesis, University of Limoges*, pages 1–168, 2021.

[47] F. Madzharova, Z. Heiner, M. Guhlke, and J. Kneipp. Surface-Enhanced Hyper-Raman Spectra of Adenine, Guanine, Cytosine, Thymine, and Uracil. *The journal of physical chemistry C*, 120:15415–15423, 2016.

[48] A.I. Perez-Jimenez, D. Lyu, Z. Lu, G. Liu, and B. Ren. Surface-enhanced Raman spectroscopy: benefits, trade-offs and future developments. *Chemical Science*, 11:4563–4577, 2020.

[49] S. Schlucker. Surface-Enhanced Raman spectroscopy: concepts and chemical applications. *Angewandte Chemie*, 53:4756–4795, 2014.

[50] C. Yuan, J. Fang, M.L. Chapelle, Y. Zhang, X. Zeng, G. Huang, X. Yang, and W. Fu. Surface-enhanced Raman scattering inspired by programmable nucleic acid isothermal amplification technology. *Trends in Analytical Chemistry*, 143:1—15, 2021.

[51] P.A. Mosier-Boss. Review of SERS Substrates for Chemical Sensing. *Nanomaterials*, 7:1—30, 2017.

[52] T. Vo-Dinh, K. Houck, and D.L. Stokes. Surface-enhanced Raman gene probes. *Analytical Chemistry*, 66:3379—3383, 1994.

[53] D. Cialla, S. Polloka, C. Steinbrücker, K. Weber, and J. Popp. SERS-based detection of biomolecules. *Nanophotonics*, 3:383—411, 2014.

[54] S.E.J. Bell and N.M.S. Sirimuthu. Surface-Enhanced Raman Spectroscopy (SERS) for Sub-Micromolar Detection of DNA/RNA Mononucleotides. *Journal of the American Chemical Society*, 128:15580—15581, 2006.

[55] K. Kneipp, H. Kneipp, V.B. Kartha, G. Deinum R. Manoharan, I. Itzkan, R.R. Dasari, and M.S. Feld. Detection and identification of a single DNA base molecule using surface-enhanced Raman scattering (SERS). *Physical Review*, 57:6281—6284, 1998.

[56] A. Barhoumi, D. Zhang, F. Tam, and N.J. Halas. Surface-Enhanced Raman Spectroscopy of DNA. *Journal of the American Chemical Society*, 130:5523–5529, 2008.

[57] M. Green, F.M. Liu, L. Cohen, P. Kollensperger, and T. Cony. SERS platforms for high density DNA arrays. *Faraday Discussion* , 132:269–280, 2006.

[58] E. Prado, N. Daugey, S. Plumet, L. Servant, and S. Lecomte. Quantitative label-free RNA detection using surface-enhanced Raman spectroscopy. *Chemical Communication*, 47:7426–7427, 2011.

[59] M. Muniz-Miranda, C. Gellini, M. Pagliai, M. Innocenti, P.R. Salvi, and V. Schettino. SERS and Computational Studies on MicroRNA Chains Adsorbed on Silver Surfaces. *The Journal of Physical Chemistry C*, 114:13730–13735, 2010.

[60] D. Li, L. Xia, Q. Zhou, L. Wang, D. Chen, X. Gao, and Y. Li. Label-Free Detection of miRNA Using Surface-Enhanced Raman Spectroscopy. *Analytical Chemistry*, 92:12769–12773, 2020.

[61] J.D. Driskell, A.G. Seto, L.P. Jones, S. Jokela, R.A. Dluhy, Y.P. Zhao, and R.A. Tripp. Rapid microRNA (miRNA) detection and classification via

surface-enhanced Raman spectroscopy (SERS). *Biosensors and Bioelectronics*, 24:917–922, 2008.

[62] X. Cao, M. Bao, Y. Shan, W. Li, and H. Shi. Rapid Detection and Identification of miRNAs by Surface-Enhanced Raman Spectroscopy Using Hollow Au Nanoflowers Substrates. *Journal of Nanomaterials*, 2017:1–12, 2017.

[63] J. Cui, Q. Guan, H. Lv, K. Fu, R. Fu, Z. Feng, F. Chen, and G. Zhang. Three-dimensional nanorod array for label-free surface-enhanced Raman spectroscopy analysis of microRNA pneumoconiosis biomarkers. *Spectrochimica Acta Part A: Molecular and Biomolecular Spectroscopy*, 261:1–7, 2021.

[64] E. Papadopoulou and S.E.J. Bell. Label-Free Detection of Single-Base Mismatches in DNA by Surface-Enhanced Raman Spectroscopy. *Angewandte Chemie International Edition*, 50:9058–9061, 2011.

[65] L.J. Xu, Z.C. Lei, J. Li, C. Zong, C. J. Yang, and B. Ren. Label-Free Surface-Enhanced Raman Spectroscopy Detection of DNA with Single-Base Sensitivity. *Journal of the American Chemical Society*, 137:5149–5154, 2015.

[66] Y. Li, T. Gao, G. Xu, X. Xiang, B. Zhao, X.X. Han, and X. Guo. Direct Approach toward Label-Free DNA Detection by Surface-Enhanced Raman Spectroscopy: Discrimination of a Single-Base Mutation in 50 Base-Paired Double Helixes. *Analytical chemistry*, 91:7980–7984, 2019.

[67] J. Zeng, M. Dong, B. Zhu, D. Chen, and Y. Li. A new method towards the detection of DNA mutation by Surface-Enhanced Raman Spectroscopy. *Talanta*, 223:121746–121753, 2021.

[68] J. Zeng, M. Dong, B. Zhu, X. Gao, D. Chen, and Y. Li. Label-Free Detection of CT Mutations by Surface-Enhanced Raman Spectroscopy Using Thiosulfate-Modified Nanoparticles. *Analytical chemistry*, 93:1951–1956, 2021.

[69] J. Morla-Folch, P. Gisbert-Quilis, M. Masetti, E. Garcia-Rico, R.A. Alvarez-Puebla, and L. Guerrini. Conformational SERS Classification of K-Ras Point

Mutations for Cancer Diagnostics. *Angewandte Chemie International Edition*, 129:2421–2425, 2017.

[70] D. Lin, Q. Wu, S. Qiu, G. Chen, S. Feng, R. Chen, and H. Zeng. Label-free liquid biopsy based on blood circulating DNA detection using SERS-based nanotechnology for nasopharyngeal cancer screening. *Nanomedicine: Nanotechnology, Biology, and Medicine*, 22:102100–102109, 2019.

[71] A.J. Hobro, S. Abdali, and E.W. Blanch. SERS study of methylated and non-methylated ribonucleosides and the effect of aggregating agents. *Journal of Raman Spectroscopy*, 43:187–195, 2012.

[72] A. Barhoumi and N.J. Halas. Detecting Chemically Modified DNA Bases Using Surface-Enhanced Raman Spectroscopy. *The Journal of Physical Chemistry Letters*, 2:3118–3123, 2011.

[73] L. Guerrini, Z. Krpetic´and D. Lierop, R.A. Alvarez-Puebla, and D. Graham. Direct Surface-Enhanced Raman Scattering Analysis of DNA Duplexes. *Angewandte Chemie International Edition*, 53:1–6, 2014.

[74] S. Ganesh and K. Venkatakrishnan annd B. Tan. Quantum scale organic semiconductors for SERS detection of DNA methylation and gene expression. *Nature communications*, 11:1135–1150, 2020.

[75] S.M.A. Hasan, Y. He, T.W. Chang, J. Wang, and M.R. Gartia. Detecting DNA Methylation Using Surface-Enhanced Raman Spectroscopy. *The journal of physical chemistry*, 123:698–709, 2019.

[76] X. Luo, L. Jiang, T. Kang, Y. Xing, E. Zheng, P. Wu, C. Cai, and Q. Yu. Label-Free Raman Observation of TET1 Protein-Mediated Epigenetic Alterations in DNA. *Analytical chemistry*, 91:7304–7312, 2019.

[77] X. Luo, Y. Xing, D.D. Galvan, E. Zheng, P. Wu, C. Cai, and Q. Yu. Plasmonic Gold Nanohole Array for Surface-Enhanced Raman Scattering Detection of DNA Methylation. *ACS Sensors*, 4:1534–1542, 2019.

[78] V. Moisoiu, V.Sas, A. Stefancu, S.D. Iancu, A. Jurj, S. Pasca, S. Iluta, A.A. Zimta, A. Tigu, P. Teodorescu, C. Turcas, C. Blag, D. Dima, G. Popa, S. Arghirescu, S. Man, A. Colita, N. Leopold, and C. Tomuleasa. SERS-Based Evaluation of the DNA Methylation Pattern Associated With Progression in Clonal Leukemogenesis of Down Syndrome. *Frontiers in Bioengineering and Biotechnology*, 9:703268–703275, 2021.

[79] J.G. Kelly, G.M. Najand, and F.L. Martin. Characterisation of DNA methylation status using spectroscopy (mid-IR versus Raman) with multivariate analysis. *Journal of Biophotonics*, 4:345–354, 2011.

[80] V. Moisoiu, A. Stefancu, S.D. Iancu, T. Moisoiu, L. Loga, L. Dican, C.D. Alecsa, I. Boros, A. Jurj, D. Dima, C. Bagacean, R. Tetean, E. Burzo, C. Tomuleasa, F. Elec, and N. Leopold. SERS assessment of the cancer-specific methylation pattern of genomic DNA: towards the detection of acute myeloid leukemia in patients undergoing hematopoietic stem cell transplantation. *Analytical and Bioanalytical Chemistry*, 411:7907–7913, 2019.

[81] A. Stefancu, V. Moisoiu, M. Desmirean, S.D. Iancu, A.B. Tigu, B. Petrushev, A. Jurj, R.G. Cozan, L. Budisan, B. Fetica, A. Roman, G. Dobie, C. Turcas, M. Zdrenghea, P. Teodorescu, S.Pasca, D. Picio, D. Dima, Z. Balint, N. Leopold, and C. Tomuleasa. SERS-based DNA methylation profiling allows the differential diagnosis of malignant lymphadenopathy. *Spectrochimica Acta Part A: Molecular and Biomolecular Spectroscopy*, 264:120216–120223, 2022.

[82] X. Li, T. Yang, C.S. Li, Y. Song, D. Wang, L. Jin, H. Lou, and W. Li. Polymerase chain reaction – surface-enhanced Raman spectroscopy (PCR-SERS) method for gene methylation level detection in plasma. *Theranostics*, 10:898–909, 2020.

[83] A. Chiado, C. Novara, A. Lamberti, F. Geobaldo, F. Giorgis, and P. Rivolo. Immobilization of Oligonucleotides on Metal-Dielectric Nanostructures for miRNA Detection. *Analytical Chemistry*, 88:9554–9563, 2016.

[84] J.L. Abell, J.M. Garren, J.D. Driskell, R.A. Tripp, and Y. Zhao. Label-Free Detection of Micro-RNA Hybridization Using Surface Enhanced Raman Spectroscopy and Least-Squares Analysis. *Journal of Americal chemical society*, 134:12889–12892, 2012.

[85] A. Kamińska, A. Sivanesan, E. Witkowska, J. Golab, M. Winiarska, D. Nowis, I. Dzięcielewski J.L. Weyher, and J. Waluk. Detection of DNA Mutations Using Novel SERS (Surface-Enhanced Raman Spectroscopy) Diagnostic Platform. *Journal of Chemistry and Chemical Engineering*, 7:972–978, 2013.

[86] T. Abdallah, H. Awad, and H. Talaat. SERS detection of DNA cancer with single-base mutation for KRAS-gene. *Egyptian Journal of Solids*, 43:144–157, 2021.

[87] Y.U. Kayran, N. Cinar, D. Jambrec, and W. Schuhmann. Monitoring Potential-Induced DNA Dehybridization Kinetics for Single Nucleotide Polymorphism Detection by using In Situ Surface Enhanced Raman Scattering. *ChemElectroChem*, 5:756–760, 2018.

[88] X. Li, T. Yang, C.S. Li, Y. Song, H. Lou, D. Guan, and L. Jin. Surface Enhanced Raman Spectroscopy (SERS) for the Multiplex Detection of Braf, Kras, and Pik3ca Mutations in Plasma of Colorectal Cancer Patients. *Theranostics*, 8:1678–1689, 2018.

[89] S. Mahajan, J. Richardson, T. Brown, and P.N. Bartlett. SERS-Melting: A New Method for Discriminating Mutations in DNA Sequences. *Journal of the American Chemical Society*, 130:15589–15601, 2008.

[90] S. Mahajan, J. Richardson, N.B. Gaied, Z. Zhao, T. Brown, and P.N. Bartlett. The Use of an Electroactive Marker as a SERS Label in an E-melting Mutation Discrimination Assay. *Electroanalysis*, 21:2190–2197, 2009.

[91] J. Kim, H.J. Park, J.H. Kim, B. Chang, and H.K. Park. Label-free Detection for a DNA Methylation Assay Using Raman Spectroscopy. *Chinese Medical Journal*, 130:1961–1967, 2017.

[92] J. Hu and C. Zhang. Single base extension reaction-based surface enhanced Raman spectroscopy for DNA methylation assay. *Biosensors and Bioelectronics*, 31:451–457, 2012.

[93] W.F. Zhu, L.X. Cheng, M. Li, D. Zuo, N. Zhang, H.J. Zhuang, D. Xie, Q.D. Zeng, J.A. Hutchison, and Y.L. Zhao. Frequency Shift Raman-Based Sensing of Serum MicroRNAs for Early Diagnosis and Discrimination of Primary Liver Cancers. *Analytical chemistry*, 90:10144–10151, 2018.

[94] L. Cheng, Z. Zhang, D. Zuo, W. Zhu, J. Zhang, Q. Zeng, D. Yang, M. Li, and Y. Zhao. Ultrasensitive Detection of Serum MicroRNA Using Branched DNA-Based SERS Platform Combining Simultaneous Detection of alpha-Fetoprotein for Early Diagnosis of Liver Cancer. *ACS applied materials and interfaces*, 10:34869–34877, 2018.

[95] J. Zhang, Y. Dong, W. Zhu, D. Xie, Y. Zhao, D. Yang, and M. Li. Ultrasensitive Detection of Circulating Tumor DNA of Lung Cancer via an Enzymatically Amplified SERS-Based Frequency Shift Assay. *ACS Applied materials and interfaces*, 11:18145–18152, 2019.

[96] J.D. Driskell and R.A. Tripp. Label-free SERS detection of microRNA based on affinity for an unmodified silver nanorod array substrate. *Chemical Communications journal*, 46:3298–3300, 2010.

[97] Y. Song, T. Xu, L.P. Xu, and X. Zhang. Nanodendritic gold/graphene-based biosensor for tri-mode miRNA sensing. *Chemical Communications journal*, 55:1742–1745, 2019.

[98] J. Zheng, J. Bai, Q. Zhou, J. Li, Y. Li, J. Yang, and R. Yang. DNA-templated in situ growth of AgNPs on SWNTs: a new approach for highly sensitive SERS assay of microRNA. *Chemical Communications journal*, 51:6552–6555, 2015.

[99] E.O. Ganbold, T. Kang, K. Lee, S.Y. Lee, and S.W. Joo. Aggregation effects of gold nanoparticles for single-base mismatch detection in influenza A (H1N1)

DNA sequences using fluorescence and Raman measurements. *Colloids and Surfaces B: Biointerfaces*, 93:148–153, 2012.

[100] J. Xia, Y. Liu, M. Ran, D. Lu, X. Cao, and Y. Wang. SERS Platform Based on Bimetallic Au-Ag Nanowires-Decorated Filter Paper for Rapid Detection of miR-196a in Lung Cancer Patients Serum. *Journal of Chemistry*, 2020:1–14, 2020.

[101] C.Y. Song, Y.J. Yang, B.Y. Yang, Y.Z. Sun, Y.P. Zhao, and L.H. Wang. Ultrasensitive SERS sensor for simultaneous detection of multiple cancer-related miRNAs. *Nanoscale*, 2016:1–9, 2016.

[102] Z. Wang, S. Zong, Z. Wang, L. Wu, P. Chen, B. Yun, and Y. Cui. Microfluidic chip based micro RNA detection through the combination of fluorescence and surface enhanced Raman scattering techniques. *Nanotechnology*, 28:1–8, 2017.

[103] T. Kang, J. Zhu, X. Luo, W. Jia, P. Wu, and C. Cai. Controlled Self-Assembly of a Close-Packed Gold Octahedra Array for SERS Sensing Exosomal MicroRNAs. *Analytical Chemistry*, 93:2519–2526, 2021.

[104] L. Liu, C. Shangguan, J. Guo, K. Ma, S. Jiao, Y. Yao, and J. Wang. Ultrasensitive SERS Detection of Cancer-Related miRNA-182 by MXene/MoS2@AuNPs with Controllable Morphology and Optimized Self-Internal Standards. *Advanced optical materials*, 8:2001214–2001224, 2020.

[105] S. Meng, R. Chen, J. Xie, J. Li, J. Cheng, Y. Xu, H. Cao, X. Wu, Q. Zhang, and H. Wang. Surface-enhanced Raman scattering holography chip for rapid, sensitive and multiplexed detection of human breast cancer-associated MicroRNAs in clinical samples. *Biosensors and Bioelectronics*, 190:113470–113480, 2021.

[106] J. Chen, Y. Wu, C. Fu, H. Cao, X. Tan, W. Shi, and Z. Wu. Ratiometric SERS biosensor for sensitive and reproducible detection of microRNA based

on mismatched catalytic hairpin assembly. *Biosensors and Bioelectronics*, 144:11619–11627, 2019.

[107] J.S. Wi, C.H. Chung, H.K. Na, and T.S. Oh. Easy-to-make-and-use gold nanotrench arrays for surface-enhanced Raman scattering. *Optical materials express*, 11:3363–3369, 2021.

[108] X. Cao, Y. Sun, Y. Mao, M. Ran, Y. Liu, D. Lu, and C. Bi. Rapid and sensitive detection of dual lung cancer-associated miRNA biomarkers by a novel SERS-LFA strip coupling with catalytic hairpin assembly signal amplification. *Journal of Materials Chemistry C*, 9:3661–3671, 2021.

[109] Y. Mao, Y. Sun, J. Xue, W. Lu, and X. Cao. Ultra-sensitive and high efficiency detection of multiple non-small cell lung cancer-related miRNAs on a single test line in catalytic hairpin assembly-based SERS-LFA strip. *Analytica Chimica Acta*, 1178:338800–338814, 2021.

[110] H. Zhang, C. Fu, S. Wu, Y. Shen, C. Zhou, J. Neng, Y. Yi, Y. Jin, and Y. Zhu. Magnetic-capture-based SERS detection of multiple serum microRNA biomarkers for cancer diagnosis. *Analytical Methods*, 11:783–793, 2019.

[111] M.B. Wabuyele, F. Yan, and T. Vo-Dinh. Plasmonics nanoprobes: detection of single-nucleotide polymorphisms in the breast cancer BRCA1 gene. *Analytical and Bioanalytical Chemistry*, 398:729–736, 2010.

[112] L. Wu, A. Garrido-Maestu, J.R.L. Guerreiro, S. Carvalho, S. Abalde-Cela, M. Prado, and L. Diéguez. Amplification-free SERS Analysis of DNA Mutation in Cancer Cells with Single-base Sensitivity. *Nanoscale*, 11:7781–7789, 2019.

[113] S.M. Restaino and I.M. White. Inkjet-printed paper surface enhanced Raman spectroscopy (SERS) sensors. *IEEE proceeding*, pages 1–3, 2016.

[114] S.M. Restaino and I.M. White. Surface Enhanced Raman Spectroscopy (SERS) methods for endpoint and real-time quantification of miRNA as-

says. *Optics and Biophotonics in Low-Resource Settings III*, 10055:1005502–1005511, 2017.

[115] T. Lee, S. Kwon, H.J. Choi, H. Lim, and J. Lee. Highly Sensitive and Reliable microRNA Detection with a Recyclable Microfluidic Device and an Easily Assembled SERS Substrate. *ACS Omega*, 6:19656–19664, 2021.

[116] T. Lee, J.S. Wi, A. Oh, H.K. Na, J.J. Lee, K. Lee, T.G. Lee, and S. Haam. Highly Robust, Uniform and Ultra-sensitive Surface-enhanced Raman Scattering Substrates for microRNA Detection Fabricated by Using Silver Nanostructures Grown in Gold Nanobowls. *Nanoscale*, 2013:1–9, 2017.

[117] J. Kim, J. Park, J. Ki, H.W. Rho, Y.M. Huh, E. Kim, H.Y. Son, and S. Haam. Simultaneous dual-targeted monitoring of breast cancer circulating miRNA via surface-enhanced Raman spectroscopy. *Biosensors and Bioelectronics*, 207:114143–114152, 2022.

[118] H. Zhou, J. Zhang, B. Li, J. Liu, J.J. Xu, and H.Y. Chen. Dual-Mode SERS and Electrochemical Detection of miRNA Based on Popcorn-like Gold Nanofilms and Toehold-Mediated Strand Displacement Amplification Reaction. *Analytical Chemistry*, 93:6120–6127, 2021.

[119] T. Lee, M. Mohammadniaei, H. Zhang, J. Yoon, H.K. Choi, S. Guo, P. Guo, and J.W. Choi. Single Functionalized pRNA/Gold Nanoparticle for Ultrasensitive MicroRNA Detection Using Electrochemical Surface-Enhanced Raman Spectroscopy. *Advanced Science*, 7:1902477–1902488, 2020.

[120] S. Kim, S.N. Jeong, S. Bae, H. Chung, and S.Y. Yoo. Sensitive Surface Enhanced Raman Scattering-Based Detection of a BIGH3 Point Mutation Associated with Avellino Corneal Dystrophy. *Analytical chemistry*, 88:11288–11292, 2016.

[121] T. Kang, H. Kim, J.M. Lee, H. Lee, Y.S. Choi, G. Kang, M.K. Seo, B.H. Chung, Y. Jung, and B. Kim. Ultra-Specifi c Zeptomole MicroRNA Detection

by Plasmonic Nanowire Interstice Sensor with Bi-Temperature Hybridization. *Small biomarkers*, 10:4200–4206, 2014.

[122] C. Novara, A. Chiado, N. Paccotti, S. Catuogno, C.L. Esposito, G. Condorelli, V.D. Franciscis, F. Geobaldo, P. Rivolo, and F. Giorgis. SERS-active metal-dielectric nanostructures integrated in microfluidic devices for label-free quantitative detection of miRNA. *The Royal Society of Chemistry*, 205:271–289, 2017.

[123] S. Mabbott, S.C. Fernandes, M. Schechinger, G.L. Cote, K. Faulds, C.R. Mace, and D. Graham. Detection of cardiovascular disease associated miR-29a using paper-based microfluidics and surface enhanced Raman scattering. *Analyst*, 145:983–991, 2020.

[124] L.P. Ye, J. Hu, L. Liang, and C. Zhang. Surface-enhanced Raman spectroscopy for simultaneous sensitive detection of multiple microRNAs in lung cancer cells. *Chemical Communications journal*, 50:11883–11886, 2014.

[125] Y. Song, T. Xu, L.P. Xu, and X. Zhang. Superwettable nanodendritic gold substrates for direct miRNA SERS detection. *Nanoscale*, 10:20990–20994, 2018.

[126] B.M. Crawford, H.N. Wang, A.M. Fales, M.L. Bowie, V.L. Seewaldt, and T. Vo-Dinh. SERS-Based Inverse Molecular Sentinel (iMS) Nanoprobes for Multiplexed Detection of MicroRNA Cancer Biomarkers in Biological Samples. *Plasmonics in Biology and Medicine XIV*, 1008:1008008–1008020, 2018.

[127] B.M. Crawford, H.N. Wang, C. Stolarchuk, R.J. Furstenberg, P. Strobbia, D. Zhang, X. Qin, K. Owzar, K.S. Garman, and T. Vo-Dinh. Plasmonic nanobiosensors for detection of microRNA cancer biomarkers in clinical samples. *Analyst*, 145:4587–4594, 2020.

[128] H.N. Wang, B.M. Crawford, A.M. Fales, M.L. Bowie, V.L. Seewaldt, and T. Vo-Dinh. Multiplexed Detection of MicroRNA Biomarkers Using SERS-

Based Inverse Molecular Sentinel (iMS) Nanoprobes. *The journal of physical chemistry*, 120:21047–21055, 2016.

[129] L. Ma, S. Ye, X. Wang, and J. Zhang. SERS-Microfluidic Approach for the Quantitative Detection of miRNA Using DNAzyme-Mediated Reciprocal Signal Amplification. *ACS sensors*, 6:1392–1399, 2021.

[130] W. Luo, C. Wu, S. Huang, X. Luo, R. Yuan, and X. Yang. Liquid Phase Interfacial Surface-Enhanced Raman Scattering Platform for Ratiometric Detection of MicroRNA 155. *Analytical chemistry*, 92:15573–15578, 2020.

[131] Y. He, X. Yang, R. Yuan, and Y. Chai. "Off" to "On" Surface-Enhanced Raman Spectroscopy Platform with Padlock Probe-Based Exponential Rolling Circle Amplification for Ultrasensitive Detection of MicroRNA 155. *Analytical Chemistry*, 89:2866–2872, 2017.

[132] Y. Wu, Y. He, X. Yang, R. Yuan, and Y. Chai. A novel recyclable surface-enhanced Raman spectroscopy platform with duplex-specific nuclease signal amplification for ultrasensitive analysis of microRNA 155. *Sensors and Actuators B: Chemical*, 275:260–266, 2018.

[133] B. Guven, F.C. Dudak, I.H. Boyaci, U. Tamerc, and M. Ozsoz. SERS-based direct and sandwich assay methods for mir-21 detection. *Analyst*, 139:1141–1147, 2014.

[134] J. Su, D. Wang, L. Norbel, J. Shen, Z. Zhao, Y. Dou, T. Peng, J. Shi, S. Mathur, C. Fan, and S. Song. Multicolor Gold-Silver Nano-Mushrooms as Ready-to-Use SERS Probes for Ultrasensitive and Multiplex DNA/miRNA Detection. *Analytical chemistry*, 89:2531–2538, 2017.

[135] L. Peng, J. Zhou, Z. Liang, Y. Zhang, L. Petti, T. Jiang, C. Gu, D. Yang, and P. Mormile. SERS-based sandwich bioassay protocol of miRNA-21 using Au@Ag core–shell nanoparticles and a Ag/TiO2 nanowires substrate. *Analytical methods*, 11:2960–2968, 2019.

[136] L. Qi, M. Xiao, X. Wang, C. Wang, L. Wang, S. Song, X. Qu, L. Li, J. Shi, and H. Pei. DNA-Encoded Raman-Active Anisotropic Nanoparticles for microRNA Detection. *Analytical chemistry*, 89:9850–9856, 2017.

[137] W. Zhou, Y.F. Tian, B.C. Yin, and B.C. Ye. Simultaneous Surface-Enhanced Raman Spectroscopy Detection of Multiplexed MicroRNA Biomarkers. *Analytical chemistry*, 89:6120–6128, 2017.

[138] W.H. Kim, J.U.Lee, S. Song, S. Kim, Y.J. Choi, and S.J. Sim. A label-free, ultra-highly sensitive and multiplexed SERS nanoplasmonic biosensor for miRNA detection using a head-flocked gold nanopillar. *Analyst*, 144:1768–1776, 2019.

[139] W.H. Kim, J.U. Lee, M.J. Jeon, K.H. Park, and S.J. Sim. Three-dimensional hierarchical plasmonic nano-architecture based label-free surface-enhanced Raman spectroscopy detection of urinary exosomal miRNA for clinical diagnosis of prostate cancer. *Biosensors and Bioelectronics*, 205:114116–114125, 2022.

[140] Z. Liang, J. Zhou, L. Petti, L. Shao, T. Jiang, Y. Qing, S. Xie, G. Wua, and P. Mormile. SERS-based cascade amplification bioassay protocol of miRNA-21 by using sandwich structure with biotin–streptavidin system. *Analyst*, 144:1741–1750, 2019.

[141] J.U. Lee, W.H. Kim, H.S. Lee, K.H. Park, and S.J. Sim. Quantitative and Specific Detection of Exosomal miRNAs for Accurate Diagnosis of Breast Cancer Using a Surface-Enhanced Raman Scattering Sensor Based on Plasmonic Head-Flocked Gold Nanopillars. *Small*, 15:1804968–1804978, 2019.

[142] Y. Zhao, X. Fang, M. Bai, J. Zhang, H. Yu, F. Chen, and Y. Zhao. A microfluidic surface-enhanced Raman scattering (SERS) sensor for microRNA in extracellular vesicles with nucleic acid-tyramine cascade amplification. *Chinese Chemical Letters*, 33:2101–2104, 2022.

[143] B. Moody and G. McCarty. Statistically Significant Raman Detection of Mid-

sequence Single Nucleotide Polymorphisms. *Analytical chemistry*, 81:2013–2016, 2009.

[144] B. Moody, J. Leotaud, and G. McCarty. Using surface-enhanced Raman spectroscopy to probe for genetic markers on single-stranded DNA. *Journal of Biomedical Optics*, 15:0270141–0270146, 2010.

[145] Y. Wang, E.J.H. Wee, and M. Trau. Highly Sensitive DNA Methylation Analysis at CpG Resolution by Surface-enhanced Raman Scattering via Ligase Chain Reaction. *Chemical communications*, 51:10953—-10956, 2015.

[146] L. Xu, Y. Gao, H. Kuang, L.M. Liz-Marzan, and C. Xu. MicroRNA-Directed Intracellular Self-Assembly of Chiral Nanorod Dimers. *Angewandte Chemie International Edition*, 57:10544–10548, 2018.

[147] M. Schechinger, H. Marks, A. Locke, M. Choudhury, and G. Cote. Development of a miRNA surface-enhanced Raman scattering assay using benchtop and handheld Raman systems. *Journal of Biomedical Optics*, 23:017002–017013, 2018.

[148] M. Schechinger, H. Marks, S. Mabbott, M. Choudhury, and G. Cote. A SERS approach for rapid detection of microRNA-17 in the picomolar range. *Analyst*, 144:4033–4044, 2019.

[149] W.J. Lee, K.J. Kim, M.K. Hossain, H.Y. Cho, and J.W. Choi. DNA–Gold Nanoparticle Conjugates for Intracellular miRNA Detection Using Surface-Enhanced Raman Spectroscopy. *BiChip Journal*, 16:33–40, 2022.

[150] K. Shin, J. Choi, Y. Kim, Y. Lee, J. Kim, S. Lee, and H. Chung. Feasibility study for combination of field-flow fractionation (FFF)-based separation of size-coded particle probes with amplified surface enhanced Raman scattering (SERS) tagging for simultaneous detection of multiple miRNAs. *Journal of Chromatography A*, 1556:97–102, 2018.

[151] M.Q. He, S. Chen, K. Yao, K. Wang, Y.L. Yu, and J.H. Wang. Oriented Assembly of Gold Nanoparticles with Freezing-Driven Surface DNA Manipulation and Its Application in SERS-Based MicroRNA Assay. *Small methods*, 3:1900017–1900024, 2019.

[152] S. Jiang, Q. Li, C. Wang, Y. Pang, Z. Sun, and R. Xiao. In Situ Exosomal MicroRNA Determination by Target-Triggered SERS and Fe3O4@TiO2-Based Exosome Accumulation. *ACS Sensors*, 6:852–862, 2021.

[153] H.N. Wang and T. Vo-Dinh. Plasmonic Coupling Interference (PCI) Nanoprobes for Nucleic Acid Detection. *Small biosensors*, 7:3067–3074, 2011.

[154] H.N. Wang and T. Vo-Dinh. Plasmonic Coupling Interference: A New Approach for Cancer Diagnostics using SERS Detection. *Advanced Biomedical and Clinical Diagnostic Systems X*, 8214:821405–821413, 2012.

[155] H.N. Wang, B.M. Crawford, S.J. Norton, and T. Vo-Dinh. Direct and Label-Free Detection of MicroRNA Cancer Biomarkers using SERS-Based Plasmonic Coupling Interference (PCI) Nanoprobes. *The journal of physical chemistry*, 123:10245–10251, 2019.

[156] M. Hou, D. He, H. Wang, J. Huang, H. Cheng, K. Wan, H.W. Li, Z. Tang, X. He, and K. Wang. Simultaneous and multiplex detection of exosomal microRNAs based on the asymmetric Au@Au@Ag probes with enhanced Raman signal. *Chinese chemical letters*, 21:01046–01055, 2021.

[157] M. Muhammad, C.S. Shao, C. Liu, and Q. Huang. Highly Sensitive Detection of Elevated Exosomal miR-122 Levels in Radiation Injury and Hepatic Inflammation Using an Aptamer-Functionalized SERS-Sandwich Assay. *ACS Applied bio materials*, 4:8386–8395, 2021.

[158] Y. Yang, X. Jiang, J. Chao, C. Song, B. Liu, D. Zhu, Y. Sun, B. Yang, Q. Zhang, Y. Chen, and L. Wang. Synthesis of magnetic core-branched Au shell nanos-

tructures and their application in cancer-related miRNA detection via SERS. *Science China materials*, 260:1129–1144, 2017.

[159] H. Zhang, Y. Yi, C. Zhou, G. Ying, X. Zhou, C. Fu, Y. Zhu, and Y. Shen. SERS detection of microRNA biomarkers for cancer diagnosis using gold-coated paramagnetic nanoparticles to capture SERS-active gold nanoparticles. *RCS Andances*, 7:52782–52793, 2017.

[160] H. Zhang, C. Fu, Y. Yi, C. Zhou, G. Ying, Y. Shen, and Y. Zhu. Magnetic-based SERS approach for highly sensitive and reproducible detection of cancer-related serum microRNAs. *Analytical Methods*, 10:624–633, 2018.

[161] J. Wu, X. Zhou, P. Li, X. Lin, J. Wang, Z. Hu, P. Zhang, D. Chen, H. Cai, R. Niessner, C. Haisch, P. Sun, Y. Zheng, Z. Jiang, and H. Zhou. Ultrasensitive and Simultaneous SERS Detection of Multiplex MicroRNA Using Fractal Gold Nanotags for Early Diagnosis and Prognosis of Hepatocellular Carcinoma. *Analytical Chemistry*, 93:8799–8809, 2021.

[162] H.T. Ngo, N. Gandra, A.M. Fales, S.M. Taylor, and T. Vo-Dinh. Sensitive DNA detection and SNP discrimination using ultrabright SERS nanorattles and magnetic beads for malaria diagnostics. *Biosensors and Bioelectronics*, 81:8–14, 2016.

[163] H.T. Ngo, N. Gandra, A.M. Fales, S.M. Taylor, and T. Vo-Dinh. DNA detection and single nucleotide mutation identification using SERS for molecular diagnostics and global health. *Proceedings of SPIE*, 10054:100540C–1–100540C–9, 2017.

[164] N. Lyu, V.K. Rajendran, J. Li, A. Engel, M.P. Molloy, and Y. Wang. Highly specific detection of KRAS single nucleotide polymorphism by asymmetric PCR/SERS assay. *Analyst*, 146:5714–5721, 2021.

[165] Y. Wu, Y. Li, H. Han, C. Zhao, and X. Zhang. Dual cycle amplification and dual signal enhancement assisted sensitive SERS assay of MicroRNA. *Analytical Biochemistry*, 564:16–20, 2019.

[166] S. Ye, M. Wang, Z. Wang, N. Zhang, and X. Luo. A DNA–linker–DNA bifunctional probe for simultaneous SERS detection of miRNAs via symmetric signal amplification. *Chemical Communications journal*, 54:7786–7789, 2018.

[167] X.Y. Du, S.H. Wu, X.B. Huang, and J.J. Sun. Ag Nanocubes Coupled with Heating-Enhanced DSN-Assisted Cycling Amplification for Surface-Enhanced Raman Spectroscopy Detection of MicroRNA-21. *ACS applied nanomaterials*, 4:2565–2574, 2021.

[168] H. Zhang, Y. Liu, J. Gao, and J. Zhen. Sensitive SERS detection of miRNA using a label-free multifunctional probe. *Chemical Communications journal*, 51:16836–16839, 2015.

[169] M. Zhu, Z. Sun, Z. Zhang, and S. Zhang. Ultrasensitive SERS detection of highly homologous miRNAs by generating 3D organic-nanoclusters and a functionalized chip with locked nucleic acid probes. *Chemical Communications journal*, 54:13431–13434, 2018.

[170] N. Lyu, V.K. Rajendran, R.J. Diefenbach, K. Charles, S.J. Clarke, A. Engel, Sydney 1000 Colorectal Cancer Study Investigators, H. Rizos, M.P. Molloy, and Y. Wang. Multiplex detection of ctDNA mutations in plasma of colorectal cancer patients by PCR/SERS assay. *Nanotheranostics*, 4:224–232, 2020.

[171] S. Huang, J. Hu, G. Zhu, and C. Zhang. Sensitive detection of point mutation using exponential strand displacement amplification-based surface enhanced Raman spectroscopy. *Biosensors and Bioelectronics*, 65:191—-197, 2015.

[172] S. Ye, X. Li, M. Wang, and B. Tang. Fluorescence and SERS Imaging for the Simultaneous Absolute Quantification of Multiple miRNAs in Living Cells. *Analytical chemistry*, 89:5124–5130, 2017.

[173] Y. Sun and T. Li. Composition-Tunable Hollow Au/Ag SERS Nanoprobes Coupled with Target-Catalyzed Hairpin Assembly for Triple-Amplification Detection of miRNA. *Analytical chemistry*, 90:11614–11621, 2018.

[174] C. Liu, C. Chen, S. Li, H. Dong, W. Dai, T. Xu, Y. Liu, F. Yang, and X. Zhang. Target-Triggered Catalytic Hairpin Assembly-Induced Core-Satellite Nanostructures for High-Sensitive "Off-to-On" SERS Detection of Intracellular MicroRNA. *Analytical chemistry*, 90:10591–10599, 2018.

[175] Y. Si, L. Xu, T. Deng, J. Zheng, and J. Li. Catalytic Hairpin Self-Assembly-Based SERS Sensor Array for the Simultaneous Measurement of Multiple Cancer-Associated miRNAs. *ACS Sensors*, 5:4009–4016, 2020.

[176] Z. Wang, S. Ye, N. Zhang, X. Liu, and M. Wang. Triggerable Mutually Amplified Signal Probe Based SERS-Microfluidics Platform for the Efficient Enrichment and Quantitative Detection of miRNA. *Analytical chemistry*, 91:5043–5050, 2019.

[177] J. Liu, T. Zheng, and Y. Tian. Functionalized h-BN Nanosheets as a Theranostic Platform for SERS Real-Time Monitoring of MicroRNA and Photodynamic Therapy. *Angewandte Chemie International Edition*, 58:7757–7761, 2019.

[178] Z. Wang, J. Xue, C. Bi, H. Xin, Y. Wang, and X. Cao. Quantitative and specific detection of cancer-related microRNAs in living cells using surface-enhanced Raman scattering imaging based on hairpin DNA-functionalized gold nanocages. *Analyst*, 144:7250–7262, 2019.

[179] J. Zhang, H. Zhang, S. Ye, X. Wang, and L. Ma. Fluorescent-Raman Binary Star Ratio Probe for MicroRNA Detection and Imaging in Living Cells. *Analytical chemistry*, 93:1466–1471, 2021.

[180] X. Cao, Z. Wang, L. Bi, C. Bi, and Q. Du. Gold nanocage-based surface-enhanced Raman scattering probes for long-term monitoring of intracellular microRNA during bone marrow stem cell differentiation. *Nanoscales*, 12:1513–1527, 2020.

[181] H.Shao, H. Lin, Z. Guo, J. Lu, Y. Jia, M. Ye, F. Sud, L. Niu, W. Kang, S. Wang, Y. Hu, and Y. Huang. A multiple signal amplification sandwich-type SERS

biosensor for femtomolar detection of miRNA. *Biosensors and Bioelectronics*, 143:111616–111623, 2019.

[182] J. Wang, C. Zhang, Z. Liu, S. Li, P. Ma, and F. Gao. Target-Triggered Nanomaterial Self-Assembly Induced Electromagnetic Hot-Spot Generation for SERS-Fluorescence Dual-Mode In Situ Monitoring MiRNA-Guided Phototherapy. *Analytical chemistry*, 93:13755–13764, 2021.

[183] S. Ye, Y. Wu, X. Zhai, and B. Tang. Asymmetric Signal Amplification for Simultaneous SERS Detection of Multiple Cancer Markers with Significantly Different Levels. *Analytical chemistry*, 87:8242–8249, 2015.

[184] X. Li, S. Ye, and X. Luo. Sensitive SERS detection of miRNA via enzyme-free DNA machine signal amplification. *Chemical Communications journal*, 52:10269–10272, 2016.

[185] J. Zheng, D. Ma, M. Shi, J. Bai, Y. Li, J. Yang, and R. Yang. A New Enzyme-Free Quadratic SERS Signal Amplification Approach for Circulating MicroRNA Detection in Human Serum. *Chemical Communications journal*, 51:16271–16274, 2015.

[186] X. Luo, J. Zhu, W. Jia, N. Fang, P. Wu, C. Cai, and J. Zhu. Boosting Long-Range Surface-Enhanced Raman Scattering on Plasmonic Nanohole Arrays for Ultrasensitive Detection of MiRNA. *ACS applied materials and interfaces*, 13:18301–18313, 2021.

[187] Y. Pang, C. Wang, J. Wang, Z. Sun, R. Xiao, and S. Wang. Fe3O4@Ag magnetic nanoparticles for microRNA capture and duplex-specific nuclease signal amplification based SERS detection in cancer cells. *Biosensors and Bioelectronics*, 79:574–580, 2016.

[188] S. Wen, Y. Su, C. Dai, J. Jia, G.C. Fan, L.P. Jiang, R.B. Song, and J.J. Zhu. Plasmon Coupling-Enhanced Raman Sensing Platform Integrated with Exonuclease-Assisted Target Recycling Amplification for Ultrasensitive and

Selective Detection of microRNA-21. *Analytical chemistry*, 91:12298–12306, 2019.

[189] Y. Hu, C. Wu, S. Huang, X. Luo, R. Yuan, and X. Yang. A novel SERS substrate with high reusability for sensitive detection of miRNA 21. *Talanta*, 228:122240–122247, 2021.

[190] Y. Cui, J. Zheng, W. Zhuang, and H. Wang. A target-activated plasmon coupling surface-enhanced Raman scattering platform for the highly sensitive and reproducible detection of miRNA-21. *New Journal of Chemistry*, 45:10907–10913, 2021.

[191] S.M. Yoo, T. Kang, B. Kim, and S.Y. Lee. Detection of Single Nucleotide Polymorphisms by a Gold Nanowire-on-Film SERS Sensor Coupled with S1 Nuclease Treatment. *European Journal of Medicinal Chemistry*, 17:8657–8662, 2011.

[192] X. Miao, Q. Fang, X. Xiao, S. Liu, R. Wu, J. Yan, B. Nie, and J. Liu. Integrating Cycled Enzymatic DNA Amplification and Surface-Enhanced Raman Scattering for Sensitive Detection of Circulating Tumor DNA. *Frontiers in Molecular Biosciences*, 8:676065–676074, 2021.

[193] Y. Pang, Q. Li, C. Wang, S. Zhen, Z. Sun, and R. Xiao. CRISPR-cas12a mediated SERS lateral flow assay for amplification-free detection of double-stranded DNA and single-base mutation. *Chemical Engineering Journal*, 429:132109–132118, 2022.

[194] Y. Yao, H. Zhang, T. Tian, Y. Liu, R. Zhu, J. Ji, and B. Liu. Iodide-modified Ag nanoparticles coupled with DSN-Assisted cycling amplification for label-free and ultrasensitive SERS detection of MicroRNA-21. *Talanta*, 235:122728–122735, 2021.

[195] M. Li, J. Li, X. Zhang, M. Yao, P. Li, and W. Xu. Simultaneous detection of tumor-related mRNA and miRNA in cancer cells with magnetic SERS nanotags. *Talanta*, 232:122432–122441, 2021.

[196] W. Xu, A. Zhao, F. Zuo, R. Khan, H.M.J. Hussain, and J. Chang. Au@Ag core-shell nanoparticles for microRNA-21 determination based on duplex-specific nuclease signal amplification and surface-enhanced Raman scattering. *Microchimica Acta*, 187:384–393, 2020.

[197] D. Ma, C. Huang, J. Zheng, J. Tang, J. Li, J. Yang, and R. Yang. Quantitative detection of exosomal microRNA extracted from human blood based on surface-enhanced Raman scattering. *Biosensors and Bioelectronics*, 101:167––173, 2018.

[198] Y. He, X. Yang, R. Yuan, and Y. Chai. Switchable Target-Responsive 3D DNA Hydrogels As a Signal Amplification Strategy Combining with SERS Technique for Ultrasensitive Detection of miRNA 155. *Analytical chemistry*, 89:8538–8544, 2017.

[199] Y. He, X. Yang, R. Yuan, and Y. Chai. A novel ratiometric SERS biosensor with one Raman probe for ultrasensitive microRNA detection based on DNA hydrogel amplification. *Journal of Materials Chemistry B*, 7:2643–2647, 2019.

[200] Y. Si, L. Xu, N. Wang, J. Zheng, R. Yang, and J. Li. Target MicroRNA-Responsive DNA Hydrogel-Based Surface-Enhanced Raman Scattering Sensor Arrays for MicroRNA-Marked Cancer Screening. *Analytical chemistry*, 92:2649–2655, 2020.

[201] X. Yang, S. Wang, Y. Wang, Y. He, Y. Chai, and R. Yuan. Stimuli-Responsive DNA Microcapsules for SERS Sensing of Trace MicroRNA. *ACS applied materials and interfaces*, 10:12491–12496, 2018.

[202] Y.S. Huh, A.J. Lowe, A.J. Chung, B. Cordovez, A.D. Strickland, C.A. Batt, and D. Erickson. Optofluidic surface enhanced Raman scattering based detection of single nucleotide polymorphism. *Conference on Miniaturized Systems for Chemistry and Life Sciences*, 13:281—-283, 2009.

[203] Y.S. Huh, A.J. Lowe, A.D. Strickland, C.A. Batt, and D. Erickson. Surface-Enhanced Raman Scattering Based Ligase Detection Reaction. *Journal of the American Chemical Society*, 131:2208—-2213, 2009.

[204] A.J. Lowe, Y.S. Huh, A.D. Strickland, D. Erickson, and C.A. Batt. Multiplex Single Nucleotide Polymorphism Genotyping Utilizing Ligase Detection Reaction Coupled Surface Enhanced Raman Spectroscopy. *Analytical chemistry*, 82:5810—-5814, 2010.

[205] M. Shi, J. Zheng, Y. Tan, G. Tan, J. Li, Y. Li, X. Li, Z. Zhou, and R. Yang. Ultrasensitive Detection of Single Nucleotide Polymorphism in Human Mitochondrial DNA Utilizing Ion-Mediated Cascade Surface-Enhanced Raman Spectroscopy Amplification. *Analytical chemistry*, 87:2734—-2740, 2015.

[206] J.S. Barea and D.K. Kang. Integration of Surface-enhanced Raman Spectroscopy with PCR for Monitoring Single Copy of KRAS G12D Mutation. *Bulletin of the Korean Chemical Society*, 42:945–951, 2021.

[207] L. Ouyang, Y. Hu, L. Zhu, G.J. Cheng, and J. Irudayaraj. A reusable laser wrapped graphene-Ag array based SERS sensor for trace detection of genomic DNA methylation. *Biosensors and Bioelectronics*, 92:755—762, 2017.

[208] A.H. Nguyen, J.U. Lee, and S.J. Sim. Plasmonic coupling-dependent SERS of gold nanoparticles anchored on methylated DNA and detection of global DNA methylation in SERS-based platforms. *Journal of Optics*, 17:114022—-114034, 2015.

[209] Y. Wang, E.J.H. Wee, and M. Trau. Accurate and Sensitive Total Genomic DNA Methylation Analysis from Sub-nanogram Input with Embedded SERS Nanotags. *Chemical communications*, 52:3560–3563, 2016.

[210] J. Turkevich, P.C. Stevenson, and J. Hillier. A study of the nucleation and growth processes in the synthesis of colloidal gold. *Discussion of the Faraday Society*, 11:55–75, 1951.

[211] J. Dong, P.L. Carpinone, G. Pyrgiotakis, P. Demokritou, and B.M. Moudgil. Synthesis of precision gold nanoparticles using Turkevich method. *Kona*, 37:224–232, 2020.

[212] M.A. Ali, T.A.S. Eldin, G.M. Ei Moghazy, I.M. Tork, and I.I. Omara. Detection of E.coli O157:H7 in feed samples using gold nanoparticles sensor. *International Journal of Current microbiology and applied science*, 3:697–708, 2014.

[213] N. Leopold and B. Lendl. A New Method for Fast Preparation of Highly Surface-Enhanced Raman Scattering (SERS) Active Silver Colloids at Room Temperature by Reduction of Silver Nitrate with Hydroxylamine Hydrochloride. *The Journal of Physical Chemistry B*, 107:5723–5727, 2003.

[214] I. Badillo-Ramirez, J.M. Saniger, J. Popp, and D. Cialla-May. SERS characterization of dopamine and in situ dopamine polymerization on silver nanoparticles. *Physical Chemistry Chemical Physics*, 21, 2021.

[215] I.J. Hidi, M. Jahn, K. Weber, D. Cialla-May, and J. Popp. Droplet based microfluidics: spectroscopic characterization of levofloxacin and its SERS detection. *Physical Chemistry Chemical Physics*, 17:21236–21242, 2015.

[216] P.C. Lee and D. Meisel. Absorption and Surface-Enhanced Raman of dyes on silver and gold sols. *The Journal of Physical Chemistry*, 86:3391–3395, 1982.

[217] E. Chirshev, K.C. Oberg, Y.J. Iofe, and J.J. Unternaehrer. Let-7 as biomarker, prognostic indicator, and therapy for precision medicine in cancer. *Clinical and translation medicine*, 8:1—14, 2019.

[218] S. Roush and F.J. Slack. The let-7 family of microRNAs. *Trends in cell biology*, 18:505–516, 2008.

[219] S. Maryam, S.K.V.Sekar, M.S. Nogueira, K.W. Kho, R. Gautam, H. Lu, R.N. Riordain, L. Feeley, P. Sheahan, R. Burke, and S. Andersson-Engels. Multiconfiguration Raman spectrometer for Early Stage Diagnosis of Oral Cancer. *Proceeding of SPIE*, 11967:1–7, 2022.

[220] S. Maryam, S.K.V. Sekar, M.D. Ghauri, E. Fahy, M.S. Nogueira, H. Lu, F. Beffara, G. Humbert, R.N. Riordain, P. Sheahan, R. Burke, K.W. Kho, R. Gautam, and S. Andersson-Engels. Mobile multi-configuration clinical translational Raman system for oral cancer application. *Analyst*, 148:1514–1523, 2023.

[221] H. Torun, B. Bilgin, M. Ilgu, N. Batur, M. Ozturk, T. Barlas, G. Guney-Esken, C. Yanik, , S. Celik, O. Dogan, O. Ergonul, F. Can, I. Solaroglu, and M.C. Onbasli. Rapid Nanoplasmonic-Enhanced Detection of SARS-CoV-2 and Variants on DNA Aptamer Metasurfaces. *Advanced Devices and Instrumentation*, 4:1–13, 2023.

[222] G.K.L. Wong, A.Y.H. Chen, S.W. Ha, R.J. Kruhlak, S.G. Murdoch, R. Leonhardt, J.D. Harvey, and N.Y. Joly. Characterization of chromatic dispersion in photonic crystal fibers using scalar modulation instability. *Optics Express*, 13:8662–8670, 2005.

[223] F. Beffara, J. Perumal, A.P. Mahyuddin, M. Choolani, S.A. Khan, J.L. Auguste, S. Vedraine, G. Humbert, U.S. Dinish, and M. Olivo. Development of highly reliable SERS-active photonic crystal fiber probe and its application in the detection of ovarian cancer biomarker in cyst fluid. *Journal of Biophotonics*, 13:1–11, 2020.

[224] L. Xiao, M.S. Demokan, W. Jin, Y. Wang, and C.L. Zhao. Fusion Splicing Photonic Crystal Fibers and Conventional Single-Mode Fibers: Microhole Collapse Effect. *Journal of lightwave technology*, 25:3565–3574, 2007.

[225] A.N. Kolyadin, A.F. Kosolapov, A.D. Pryamikov, A.S. Biriukov, V.G. Plotnichenko, and E.M. Dianov. Light transmission in negative curvature hollow-core fiber in extremely high material loss region. *Optics Express*, 21:9514–9519, 2013.

[226] A.M. Pinto and M. Lopez-Amo. Photonic Crystal Fibers for Sensing applications. *Journal of Sensors*, 2012:1–22, 2012.

[227] F. Khozeymeh, F. Melli, S. Capodaglio, R. Corradini, F. Benabid, L. Vincetti, and A. Cucinotta. Hollow-Core Fiber-Based Biosensor: A Platform for Lab-in-Fiber Optical Biosensors for DNA Detection. *MDPI sensors*, 22:1–11, 2022.

[228] B. Debord, A. Amsanpally, M. Chafer, A. Baz, M. Maurel, J.M. Blondy, E. Hugonnot, F. Scol, L. Vincetti, F. Gerome, and F. Benabid. Ultralow transmission loss in inhibited-coupling guiding hollow fibers. *Optica*, 4:209–214, 2017.

[229] J.B. Jensen, L.H. Pedersen, P.E. Hoiby, L.B. Nielsen, T.P. Hansen, J.R. Folkenberg, J. Riishede, D. Noordegraaf, K. Nielsen, A. Carlsen, and A. Bjarklev. Photonic crystal fiber based evanescent-wave sensor for detection of biomolecules in aqueous solutions. *Optics Letters*, 29:1974–1976, 2004.

[230] F. Giovanardi, A. Cucinotta, F. Benabid, L. Rosa, and L. Vincetti. Hollow Core Inhibited Coupling Fibers for Biological Optical Sensing. *Journal of lightwave technology*, 37:2598–2604, 2019.

[231] F. Beffara, G. Humbert, J.L. Auguste, J. Perumal, U.S. Dinish, and M. Olivo. Optimization and performance analysis of SERS-active suspended core photonic crystal fibers. *Optics Express*, 28:23609–23619, 2020.

[232] M. Polyanskiy. Refractive index database [online]. 2008. URL: `https://refractiveindex.info/?shelf=main&book=Ag&page=Rakic-BB` [cited 8-9-2023].

[233] D. Czernia. Sellmeier equation calculator [online]. 2022. URL: `https://www.calctool.org/optics/sellmeier-equation` [cited 08-09-2023].

[234] L. Gao, H. Zhao, T. Li, P. Huo, D. Chen, and B. Liu. Atomic Force Microscopy Based Tip-Enhanced Raman Spectroscopy in Biology. *MDPI International Journal of Molecular Sciences*, 19:1–16, 2018.

[235] A. Fiocco. Development of electrochemical tip-enhanced Raman spectroscopy : towards the characterization of electroactive molecular architectures. *Ph.D. thesis, Chemical Physics [physics.chem-ph]. Sorbonne Université*, pages 1–196, 2022.

[236] N. Kumar, S. Mignuzzi, W. Su, and D. Roy. Tip-enhanced Raman spectroscopy: principles and applications. *EPJ Techniques and Intrumentation*, 2:1–23, 2015.

[237] E. Bailo and V. Deckert. Tip-enhanced Raman scattering. *The Royal Society of Chemistry*, 37:921–930, 2008.

[238] M. Ghislandi, G.G. Hoffmann, E. Tkalya, L. Xue, and G.D. With. Tip-Enhanced Raman Spectroscopy and Mapping of Graphene Sheets. *Applied Spectroscopy Reviews*, 47:371–381, 2012.

[239] K.F. Domke, D. Zhang, and B. Pettinger. Tip-Enhanced Raman Spectra of Picomole Quantities of DNA Nucleobases at Au(111). *Journal of the American Chemical Society*, 129:6708–6709, 2007.

[240] E. Bailo and V. Deckert. Tip-Enhanced Raman Spectroscopy of Single RNA Strands: Towards a Novel Direct-Sequencing Method. *Angewandte Chemie International Edition*, 47:1658–1661, 2008.

[241] O. Lancry, A. Tempez, and M. Chaigneau. Ters characterization of graphene nanoribbons [online]. 2021. URL: `https://static.horiba.com/fileadmin/Horiba/Application/Information_Technology/Semiconductors/Graphene/AFM-21-TERS-Characterization-of-Graphene-Nanoribbons.pdf` [cited 1-19-2024].

Acknowledgements

I would like to express my gratitude to a number of people with whom I had the honor to collaborate during my Ph.D. journey.

First of all, I am sincerely thankful to my supervisor Professor Annamaria Cucinotta, who provided me with precious guidance and help in solving scientific, academic, and organizational issues. It was a pleasure to work under the supervision of such a remarkable Professor.

I would like to express my great appreciation to Professor Daniel Milanese and Dr. Maria Diana Grimaldi, the coordinators of the PHAST-ETN project, for their precious help with organizational issues raised when planning the secondments and trips within the project.

I would like to thank Professor Stefano Selleri for his kind support at the beginning of my Ph.D., Dr. Corrado Sciancalepore for his chemical expertise, Professor Matteo Masino for the provision of the Raman equipment, and Dr. Carlo Fornaini for supplying teeth samples for Raman trial experiments.

I would like to acknowledge Professor Federica Maria Angel Rizzi, Dr. Aide Negri, and Dr. Marina Marozzi for conducting the training about RNA and miRNA extraction and providing their biological expertise.

I would like to thank Professor Davide Janner and Dr. Matteo Giardino for sharing their expertise in the development and testing of the SERS sensors and supervising me during my secondment at Politecnico di Torino, Turin, Italy.

I would like to express my great appreciation to Professor Michael Schmitt, Dr. Dana Cialla-May, Dr. Edoardo Farnesi, and Dr. Chen Liu, who have guided me in

the fabrication of NPs colloidal solutions and Raman measurement of miRNA and its bases during my secondment at Leibniz-IPHT, Jena, Germany.

I would like to deeply thank Professor Stefan Andersson-Engels, Dr. Kiang Wei Kho, Dr. Siddra Maryam, and Dr. Muhammad Daniyal Ghauri for their precious guidance in the SERS measurement inside PCFs conducted during my secondment at Tyndall National Institute, Cork, Ireland.

I am grateful to Professor Roberto Corradini, Professor Luca Vincetti, Dr. Federico Melli, Dr. Foroogh Khozeymeh Sarbishe, and Nicola Monelli for our productive collaboration on the work related to transmission spectra shift-based measurement of DNA inside PCFs.

Finally, I would like to acknowledge Dr. Sebastien Legendre, Dr. Alice Fiocco, and Dr. Pooja Girish for their warm welcome and for sharing their expertise in the TERS measurement of miRNAs performed during my secondment in Horiba SAS, Lille, France.

The project is a part of the PHAST-ETN project that received funding from the European Union's Horizon 2020 research and innovation program under the Marie Sklodowska-Curie grant.